Title	Synthesis and Properties of Fluorinated Sumanenes
Author(s)	李, 明洪
Citation	大阪大学, 2024, 博士論文
Version Type	VoR
URL	https://doi.org/10.18910/98757
rights	
Note	

Doctoral Dissertation

Synthesis and Properties of Fluorinated Sumanenes

（フッ素化スマネンの合成と性質）

LI MINGHONG

June 2024

Department of Applied Chemistry

Graduate School of Engineering

Osaka University

Table of contents

Chapter 1 **Introduction**

Chapter 2 **Dielectric response of 1,1-difluorosumanene caused by an in-plane motion**

Chapter 3 **Tuning the dielectric response by co-crystallisation of sumanene and its fluorinated derivative**

Chapter 4 **Biased Bowl-Direction of Monofluorosumanene in the Solid State**

Chapter 1. Introduction

Section 1. Fluorinated compounds

The development of fluorine chemistry has started since Henry Moissan[1] first isolated fluorine in 1886. In the 1930s, a series of critical fluorinated compounds-chlorofluorocarbons (Freons) were used widely as refrigerants, [2] and a milestone in fluorine chemistry was the advance of the Manhattan Project.[3] Many fluorides have been found to prepare highly resistant materials, lubricants, and extremely anti-corrosive materials.[4] The fluorine chemistry has been very important in numerous diversified technical disciplines throughout the past 90 years, including fluorinated polymers, drugs, and material science.[5]

To understand why fluorides possess diverse, unique properties, elemental fluorine must be realized. The atomic radius of a fluorine atom is 42 pm, which is very close to the hydrogen atom whose radius is 25 pm, the property allows the fluorides possessing a similar molecular radius with their hydrogen derivatives, which benefits the fluorinated derivatives to form cocrystals with itself. Furthermore, the fluorine atom is located in the upper right corner of the periodic table. It possesses the highest electronegativity of any element, which makes relatively weak (38 kcal/mol) F–F bond, resulting in fluorine gas being the most reactive chemical reagent. Due to the unique properties of fluorine, the existence of fluorine in organic compounds increases the bond energy between other nearby atoms in the same molecule (i.e., C–C bond energies of CH_3CH_3 and CH_3CF_3 = 88.8 and 101.2kcal/mol, respectively).

In the early stages of organic fluoride synthesis, researchers relied extensively on direct fluorination reactions. Organic molecules were subjected to reactions with elemental fluorine gas (F_2) or other fluorine sources such as hydrogen fluoride (HF) or metal fluorides.[7-10] However, due to elemental fluorine's reactivity, these techniques usually needed more selectivity, strong reaction conditions, and safety issues. Electrophilic fluorination was a significant step forward in organic fluoride synthesis. This process necessitates the employment of strong fluorinating agents, such as a source of electrophilic fluorine, Selectfluor®, or *N*-fluorobenzenesulfonimide (NFSI). Electrophilic fluorination allows fluorine atoms to be incorporated into a wide range of functional groups, including aromatic rings,[11-13] alkenes,[14-15] and carbonyl compounds.[16-17] Nucleophilic substitution techniques were often employed to manufacture alkyl and aryl fluorides. The alkali metal fluorides (e.g., potassium fluoride, KF)[18-19] or tetraalkylammonium fluorides act as a nucleophilic reagent in the organic substrate in these reactions.[20-22] Because of their excellent chemical selectivity and moderate reaction conditions, nucleophilic fluorination methods are helpful for the synthesis of a broad spectrum of organic fluorides. Furthermore, transition metal-catalyzed fluorination has attracted more and more attention in recent years. In this field, transition metal complexes are utilized as catalysts to aid in integrating fluorine atoms into organic molecules, for example, palladium-catalyzed cross-coupling, copper-mediated fluorination,[23] and nickel-catalyzed C–F bond synthesis.[24]

The development of fluorine chemical synthesis methods has promoted its application in many fields. In biomedicine, fluorine could act as a bioisostere of the hydrogen atom. About 20% of pharmaceuticals, including top-class therapies, contain fluorine.[25] At the same time, it plays a unique role in the medical field: for example, volatile anesthetics are fluorinated ethers,[26] and blood substitutes are made from perfluorinated alkanes because of their high oxygen solubility.[27] On the other hand, because surface energies and surface tensions of fluorosurfactants are exceedingly low,[28] hydrofluorocarbons are also employed as new refrigerants since they do not contribute to ozone depletion.[29] Strongly fluorinated substituents offer unique solubility behavior to molecules, enabling organic chemistry product purification.[30] These fluorous phases can undertake many harsh agents due to the relatively strong C–F bond.[31] Furthermore, in both organic solvents and water, hydrophobic fluorinated ionic liquids can develop insoluble phases, resulting in multiphasic liquids.[32]

Section 2. A series of important fluorinated materials: dielectric materials

Fluorine chemistry also plays a significant role in the field of materials. The fluorination of the molecular skeleton, in particular, not only results in electron acceptance but also causes a large dipole moment. Some fluorinated compounds can display a dielectric response with suitable molecular arrangement to benefit molecule rotation along the dipole moment direction, so that they can be employed as dielectric materials, which are insulators but can store the energy from electric fields. Weakly bound electrons and free electrons in dielectric substances do not float across them. Dielectric materials allow for dielectric polarization, allowing them to function as dielectrics rather than conductors. When a dielectric is charged with an external electric field, the positive charges are located in the same direction as the electric field. In contrast, the negative charges are forced to gather in the contrary direction. A high internal field was formed by this polarization, lowering the total electric field inside the material. (Scheme 1)

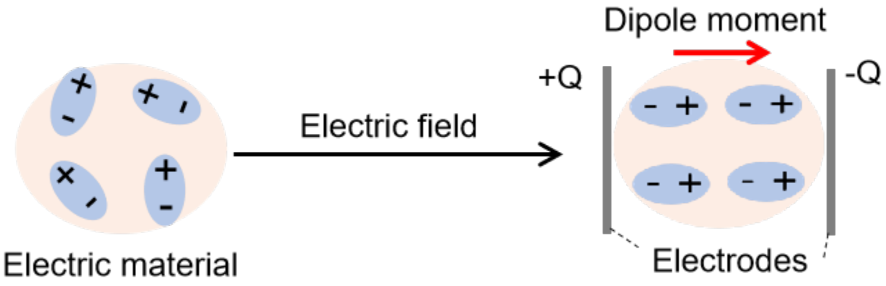

Scheme 1. Dielectric response of dielectric material under electric field.

The ability of dielectric materials to maintain electrostatic fields while dissipating minimum energy to form heat is an important aspect. Dielectric loss is the dissipation of heat or energy. An excellent dielectric material should possess a slight dielectric loss and a large dielectric constant (denoted as ε^*), which denotes the ability to store the energy. In general, the vacuum and dry gases possess low dielectric constants.[33] Meanwhile, ceramics and glass are materials with modest dielectric constants. Metal oxides have high dielectric constants in general.[34]

The following are the most significant dielectric properties: 1) Electrical sensitivity.

This measures how quickly a dielectric substance may be polarized under an electric field. This is the dielectric constant of the material (ε^*). 2) Polarization via dielectric. When an electric field is facilitated with voltage, it stores a certain quantity of electrical energy. It can cancel out the entire electric field because it causes (+) and (–) charges to move in opposing directions. 3) The moment of an electric dipole. The dipole moment is the degree to which (–) and (+) charges are divided inside the material. A dipole moment is created when an electric charge is applied. 4) The amplitude of an electronic signal that occurs when the dielectric molecules that create the dipole moment are composed of neutral particles. 5) Relaxation period. Once some delay, the atoms in the dielectric substance revert to their beginning condition once an applied electric field is removed. The relaxing period is the time that follows the delay.

Dielectric materials are employed in a wide range of applications. They are typically employed as capacitors due to their capacity to hold charges.[35] Dielectric materials with high dielectric constant are frequently utilized to improve the performance of semiconductors.[36] For example, mineral oils can be used as insulators in transformers, earth reactors, etc.[37] In addition, the liquid-crystal screen,[38] and resonating oscillators[39], etc., all these devices require dielectrics.[40] Specially prepared dielectrics function as the electrostatic equivalent of magnets in various applications.[41,42] A large number of organic fluorides are valuable dielectric materials. Organic fluoride dielectric materials provide a wide range of remarkable qualities, including excellent electrical insulation, good stability, resistance to erosion, and low surface energy. These characteristics make them useful in various sectors, including electronics, aerospace, chemical processing, and consumer items.

Section 3. Previous works of fluorinated dielectrics

Many fluoropolymers have advanced dielectric properties. Polytetrafluoroethylene (PTFE), for example, is a commonly used organic fluoride recognized for its exceptional electrical insulating qualities.[43] It is frequently used as a coating in wires and cables to reduce electrical leakage and improve safety. Perfluoroalkoxy alkane (PFA) is an organic fluoride that is extensively utilized as a dielectric material in high-temperature electronic components such as capacitors and insulators.[44] These materials offer good insulation between conductive layers and aid in reducing signal losses and cross-talk. They are biocompatible, electrically insulating, and chemically resistant, making them suitable for usage in lots of medical applications. Furthermore, perfluorocyclobutane (PFCB) is employed as a dielectric material in optical films.[45] By providing insulation and lowering reflection, these coatings improve the performance of displays such as LCDs and OLEDs. The unique qualities of these materials are useful in various of fields and for technological breakthroughs. Importantly, polyvinylidene fluoride (PVDF) is a preferred fluorinated polymer because of its outstanding piezoelectric capabilities, a unique property known as the piezoelectric effect,[46] which is the phenomenon that describes the capacity of some materials to develop an electric charge by mechanical strain and to deform under electric field. Piezoelectric materials are used in sensors,[47] actuators,[48] ultrasonic devices,[49] and even in generating power by vibrations.[50] Polyvinylidene fluoride (PVDF) is an excellent pyroelectric material, meaning it can develop an electric charge in reaction to temperature changes. When the temperature of a pyroelectric material varies, its crystal structure shifts slightly, resulting in an electric dipole moment and the creation of electric charges. Infrared sensors, thermal imaging devices, and energy harvesting applications all make use of pyroelectric materials.[51]

Apart from the fluorinated polymers, some other organic fluorides are also used as dielectric materials or used to make dielectric materials. For example, the crystal of 2-fluoronathylene exhibits a significant dielectric response maximized by the free molecular rotation in the single crystal state under an external electric field.[52] *m*-fluoroanilinium exhibited a 180° flip-flop motion induced by the electric field in a cocrystal system. This cocrystal can be used as a ferroelectric material,[53] which is a subset of dielectric material that exhibits a spontaneous electric polarization even without an external electric field. It has a unique property known as hysteresis, meaning its polarization state remains even after the electric field is removed; these properties making it to retain its polarization memory and exhibit properties like non-linear capacitance and electro-optic effect and it can be used in memory devices,[54] capacitors,[55] sensors,[56] and various other applications.[57]

Section 4. Sumanene chemistry

Sumanene (**Sum**) is a curve molecule, a fragment of C_{60} (Fig. 1a)[58], and its unusual bowl-shaped structure confers several unique properties.[59] Especially, **Sum** showed π-packing columns in the crystal at the same direction (Fig. 1b) that exhibits anisotropic electron mobility[60] and a large Seebeck coefficient.[61] In addition, the **sum** skeleton functions as a liquid crystalline mesogen.[62] All this evidence supports the claim that sumanene possesses great potential to generate multiple materials with various functions. Importantly, **Sum** can exhibit a bowl inversion in the solutions (Fig. 1c). This unique bowl inversion behavior may serve as a switching trigger for additional structural and electrical perturbations.

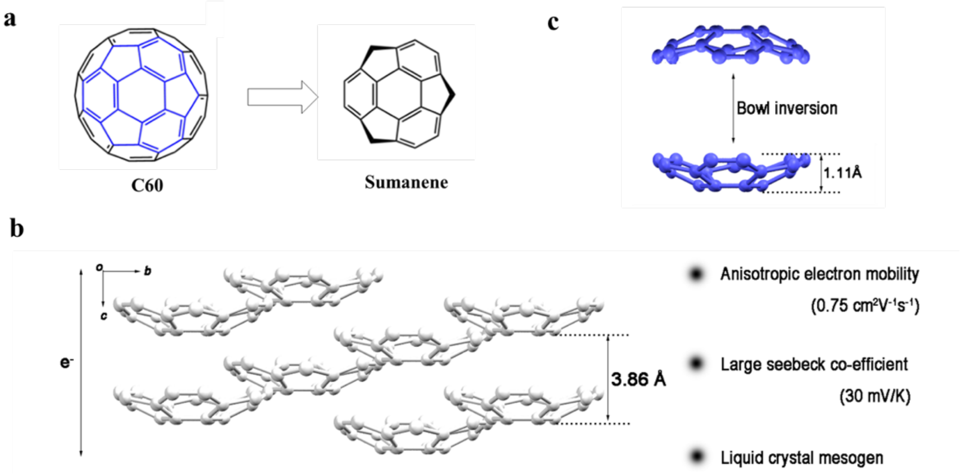

Fig. 1. Properties of Sumanene.

Section 5. This work: Synthesis and properties of fluorosumanenes

The motivation for introducing fluorine atoms into the sumanene skeleton could be categorized in three aspects: 1) As mentioned above, the fluorine atom possesses the largest electronegativity in the periodic table of elements, therefore, introducing it into the sumanene skeleton will change its original dipole moment. Meanwhile, if an external electric field is applied, the direction of the dipole moment of the fluorosumanene would move following the movement of the external electric field, and therefore, the fluorosumanene may exhibit a dielectric response; 2) The atomic radius of the fluorine atom is relatively small as a hydrogen atom, introducing it into the sumanene skeleton may result in similar packing structure in the crystal state. By using these properties, it may be possible to form a co-crystal between the fluorosumanene and pristine sumanene. And by controlling the ratio of them in the resulting co-crystal, it is possible to tune the physical properties of pristine sumanene; 3) The pristine sumanene exhibits bowl inversion in solution. The bowl inversion of the sumanene skeleton of fluorosumanene will produce two diastereoisomers, and these two diastereoisomers may differ in physical properties. Controlling the crystallization conditions to obtain specified diastereomers may resulting different functional materials with different physical properties. Based on the above motivation, the author has attempted to use the sumanene skeleton as a stimulus-responsive component by introducing fluorine atoms to achieve a dielectric response caused by in-plane motions(Scheme 2).

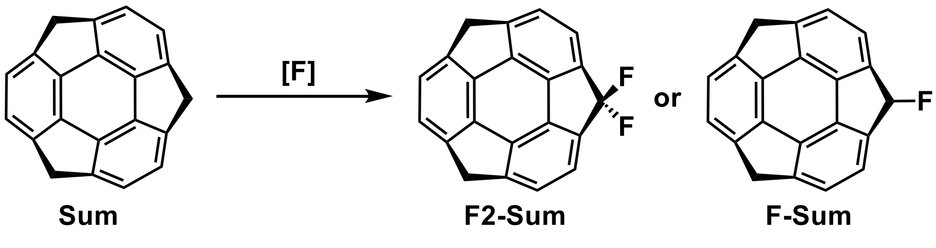

Scheme 2. Fluorination of sumanene.

In Chapter 2, 1,1-difluorosumanene was developed, which possesses two fluorines at one benzyl position on the skeleton of sumanene. This produces a strong dipole moment in the planar direction. Thermal experiments at various temperatures, X-ray diffraction, and infrared investigations demonstrated planar motion in the packing columns of 1,1-difluorosumanene was achieved at high temperatures, with no phase transitions in the crystalline form. The dielectric experiment of 1,1-difluorosumanene in powder and single-crystal state indicated the real (ε_1) and imaginary (ε_2) parts of the dielectric constant increased above 360 K at 1 MHz due to Debye-type dielectric relaxation, suggesting an in-plane motion caused by an electric field.

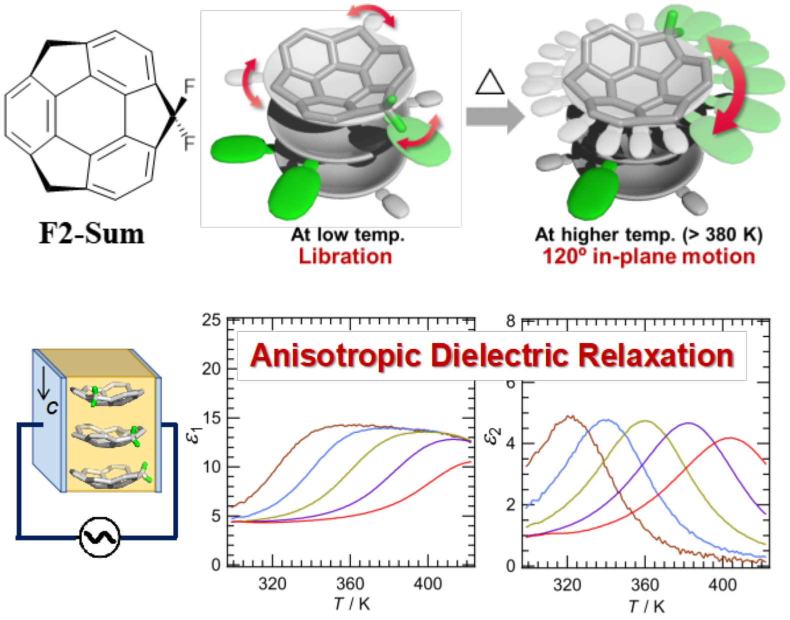

In Chapter 3, the author created several co-crystals consisting of **F2-Sum** and sumanene. Co-crystallization was successful in altering structural and physical properties, notably the dielectric response, without the need for chemical modifications. X-ray analysis and theoretical investigations demonstrate that 1,1-difluorosumanene lowers intermolecular interaction energy and benefit in increasing the dielectric response of the cocrystals.

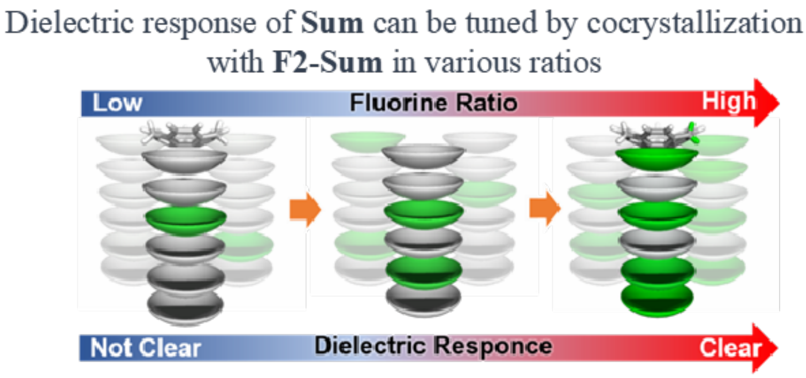

In Chapter 4, 1-fluorosumanene (**F-Sum**) was designed and synthesized, with one fluorine at the benzyl position of sumanene. Interestingly, 1-fluorosumanene displays bowl inversion in the solvated state, leading in the formation of two diastereomeric isomers: **F-Sum**$_{\text{endo}}$ and **F-Sum**$_{\text{exo}}$, each with a different dipole moment. The study discovered an energy relationship between **F-Sum**$_{\text{exo}}$, **F-Sum**$_{\text{endo}}$, and the solvent, allowing for the manipulation of the *exo*:*endo* ratio in single crystals by choosing the proper crystallization solvent. The molecular dynamics (MD) simulations demonstrate that **F-Sum**$_{\text{exo}}$ enhances packing structure elongation. The solvation-induced stability differential between **F-Sum**$_{\text{endo}}$ and **F-Sum**$_{\text{exo}}$ influences the final *exo* to *endo* ratio. The variable *exo*-*endo* proportion of **F-Sum** enables the development of novel materials with unique dielectric properties.

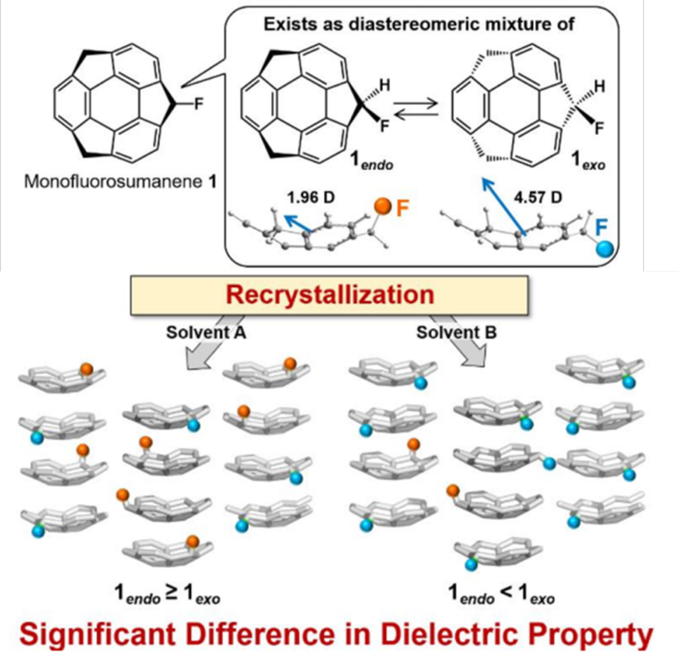

References

1. a) H. Moissan, *C. R. Acad. Sci.,* **1886**, *102*, 1534; b) H. Moissan, *C. R. Acad. Sci.,* **1886**, *103*, 202.

2. A. J. Elliott, Chlorofluorocarbons in: Organofluorine Chemistry: Principles and Commercial Applications, R. E. Banks, B. E. Smart, J. C. Tatlow, eds., Plenum Press, New York, **1994**, 145–157.

3. R. E. Banks, D. W. A. Sharp, J. C. Tatlow (Eds.), Fluorine: The First Hundred Years (1886–1986), Elsevier, Lausanne, **1986**.

4. V. Gouverneur, K. Seppelt, *Chem. Rev.,* **2015**, *115*, 563–565.

5. R. E. Banks, B. E. Smart, J. C. Tatlow, eds., Organofluorine Chemistry: Principles and Commercial Applications, Plenum Press, New York, **1994**.

6. W. R. Dolbier Jr. *J. Fluor. Chem.,* **2005**, *126*, 157–163.

7. H. Hayashi, H. Sonoda, K. Fukumura, T. Nagata, *Chem. Commun.,* **2002**, 1618-1619.

8. D. A. Watson, M. Su, G. Teverovskiy, Y. Zhang, J. García-Fortanet, T. Kinzel, S. L. Buchwald, *Science*, **2009**, *325*, 1661-1664.

9. G. A. Olah, J. T. Welch, Y. D. Vankar, M. Nojima, I. Kerekes, J. A. Olah, *J. Org. Chem.*, **1979**, *44*, 3872-3881.

10. F. Wang, S. Kim, D. Seo, K. Kang, L. Wang, D. Su, J. J. Vajo, J. Wang, J. Graetz, *Nat. Commun.,* **2015**, *6*, 6668.

11. M. A. Subramanian, L .E. Manzer, *Science*, **2002**, *297*, 1665–1665.

12. P. S. Fier, J. F. Hartwig, *J Am Chem Soc.,* **2012**, *134*, 10795–10798.

13. S. D. Taylor, C. C. Kotoris, G. Hum, *Tetrahedron*, **1999**, *55*, 12431-12477.

14. S. Qiu, T. Xu, J. Zhou, Y. Guo, G. Liu, *J. Am. Chem. Soc.,* **2010**, *132*, 2856-2857.

15. D.-F. Lu, C.-L. Zhu, J. D. Sears, H. Xu, *J. Am. Chem. Soc.,* **2016**, *138*, 11360-11367.

16. F. Li, Z. Wu, J. Wang, *Angew. Chem. Int. Ed.,* **2015**, *54*, 656-659.

17. X. Dong, W. Yang, W. Hu, J. Sun, *Angew. Chem. Int. Ed,.* **2015**, *54*, 660-663.

18. M. Khandelwal, G. Pemawat, R. K. Khangarot, *Asian J. Org. Chem.,* **2022**, *11*, 1-17.

19. H. Dang, M. Mailig, G. Lalic, *Angew. Chem. Int. Ed.,* **2014**, *53*, 6473-6476.

20. H. Sun, S. G. DiMagno, *J. Am. Chem. Soc,.* **2005**, *127*, 2050-2051.

21. H. Sun, S. G. DiMagno, *Angew. Chem. Int. Ed.,* **2006**, *45*, 2720-2725.

22. S. D. Schimler, M. A. Cismesia, P. S. Hanley, R. D. Froese, M. J. Jansma, D. C. Bland, M. S. Sanford, *J. Am. Chem. Soc.,* **2017**, *139*, 1452-1455.

23. P. S. Fier, J. F. Hartwig, *J. Am. Chem. Soc.,* **2012**, *134*, 10795–10798.

24. M. G. Campbell, T. Ritter, *Chem. Rev.,* **2015**, *115*, 612–633.

25. Sinz, M. W. *Top. Med. Chem.,* **2015**, *9*, 159−190.

26. Y. Wang, X. Ming, C. Zhang , *Curr. Med. Chem.,* **2020**, *27*, 5599-5652.

27. H Meinert, A Knoblich, *Biomater Artif Cell Immobil Biotechnol* **1993**, *21*, 583-95.

28. Y. Chiu, H. Chan, K. K. L. Phua, Y. Zhang, S. Juul, B. R. Knudsen, Y. Ho, K. W. Leong, *ACS Nano,* **2014**, *8*, 3913–3920.

29. R. Filippo, O. S. Bursi, R. Maggio, *Energy Build.,* **2022**, *273*, 112385.

30. R. Narayan, R. Dominko, *Nat. Rev. Chem.,* **2022**, *6*, 449–450.

31. A. Crombie, S. Kim, S. Hadida, Dennis P. Curran. *Org. Synth.* vol. 10, p. 712.

32. M. L. Ferreira, N. S.M. Vieira, P. J. Castro, L. F. Vega, J. M.M. Araújo, A. B. Pereiro, *J. Mol. Liq.* **2022**, *359*, 119285.

33. R. H. Orcutt; R. H. Cole, *J. Chem. Phys*. **1967**, *46*, 697–702.

34. J. Azadmanjiri, C. C Berndt, J. Wang, A. Kapoor, V. K Srivastava, C. Wen, *J. Mater. Chem. A.,* **2014**.*2*, 3695-3708.

35. A. Zahedi, F. A. Boroumand, H. Aliakbrian, *IET Microw. Antenna. P.* **2020**, *14*, 1926 –1932.

36. Koughia C. Springer handbook of electronic and photonic materials[M]. Springer Science & Business Media, **2007**.

37. J. Rouabeh, L. M. Barki, A. Hammami, I. Jallouli, A. Driss, *Heliyon,* **2019**, *5*, 1159.

38. V. V. Belyaev, D. N. Chausov, A. D. Kurilov, D. O. Rybakov, A. S. Solomatin, A. A. Murauski, A. A. Muravsky, V. G. Chigrinov, *J. SID*, **2015**, *23*, 403.

39. G. Kaizhou, L. A. Trinogga, Y. Rongsheng, *Chin. J. Electron.,* **1994**, *11*, 180.

40. A. Ahmed, I. A. Goldthorpe; A. K. Khandani, *Appl. Phys. Rev., 2*, **2015**, 11302.

41. I. Bica, M. Balaoiu, P. Sirloaga, *Results Phys.,* **2022**, *35*, 105332.

42. P. Chen, S. Harmand, S. Ouenzerf, *Appl. Therm. Eng.,* **2020**, *180*, 115862.

43. L. M. Rasheed, R. Mansoor, *IOP Conf. Ser.: Mater. Sci. Eng.1090 012104*, **2021**.

44. Q. Lei, C. E. J. Dancer, C. R. M. Grovenor, P. S. Grant, *Compos. Sci. Technol.,* **2016**, *129*, 198-204.

45. J. Ghim, D. Lee, B. G. Shin, D. Vak, D. K. Yi, M. Kim, H.-S. Shim, J. Kim, D. Kim, *Macromolecules,* **2004**, *37*, 5724-5731.

46. P. K. Szewczyk, A. Gradys, S. K. Narayan, P. Sajkiewicz, U. Stachewicz, *ACS Appl. Mater. Interfaces,* **2020**, *12*, 13575−13583.

47. P. Regtien, E. Dertien, In Sensors for Mechatronics (Second Edition), Elsevier, The Netherlands, **2018**.

48. X. Gao, J. Yang, J. Wu, X. Xin, Z. Li, X. Yuan, X. Shen, S. Dong, *Adv. Mater. Technol.,* **2020**, *5*, 1900716.

49. J. Pan, C. Bai, Q. Zheng, H. Xie, *Micromachines,* **2023**, *14*, 374.

50. R. C. Garimella, V. R. Sastry, M. S. Mohiuddin, *Procedia Earth Planet. Sci.,* **2015**, *11*, 445-456.

51. R. Yang, J. Li, Y. Wang, Y. Liu, X. Du, W. Li, *Infrared Phys. Techn.,* **2021**, *113*, 103624.

52. A. Aihara, *Chem. Lett.,* **1987**, 1201-1204.

53. T. Akutagawa, H. Koshinaka, D. Sato, S. Takeda, S. Noro, H. Takahashi, R. Kumai, Y. Tokura, T. Nakamura, *Nature Mater.,* **2009**, *8*, 342.

54. I. Kim, J. Lee, *Adv. Mater.,* **2023**, *35*, 2206864.

55. J. Íñiguez, P. Zubko, I. Luk'yanchuk & A. Cano, *Nature Rev. Mater.,* **2019**, *4*, 243–256.

56. W. Li, C. Li, G. Zhang, Z. Wang, Q. Tong, W. Dong, S. Jiang, S. Zhang, Q. Wang, *Adv. Mater.,* **2021**, *33*, 2104107.

57. T. Y. Kim, S. K. Kim, S.-W. Kim, *Nano Converg.* **2018**, *5*, 30.

58. H. Sakurai, T. Daiko, T. Hirao, *Science,* **2003**, *301*, 1878.

59. M. Saito, H. Shinokubo, H. Sakurai, *Mater. Chem. Front.,* **2018**, *2*, 635.

60. T. Amaya, S. Seki, T. Moriuchi, K. Nakamoto, T. Nakata, H. Sakane, A. Saeki, T. Hirao, *J. Am. Chem. Soc.,* **2009**, *131*, 408.

61. H. Kojima, M. Nakagawa, R. Abe, F. Fujiwara, Y. Yakiyama, H. Sakurai, M. Nakamura, *Chem. Lett.,* **2018**, *47*, 524.

62. Y. Shoji, T. Kajitani, F. Ishiwari, Q. Ding, H. Sato, H. Anetai, T. Akutagawa, H. Sakurai, T. Fukushima, *Chem. Sci.,* **2017**, *8*, 8405.

Chapter 2: Dielectric Response of 1,1-Difluorosumanene Caused by an In-Plane Motion

Section 1. Introduction

Chemists are exploring crystalline dielectric functional materials based on organic molecules to develop new types of electronics.[1] To achieve a high dielectric constant, materials must undergo molecular motions caused by an external dielectric field. The types of molecular motions that have been widely studied can be found in rotor-type structures,[2-5] π-stacked columns[6-8], etc.[9,10] (Fig. 2a)

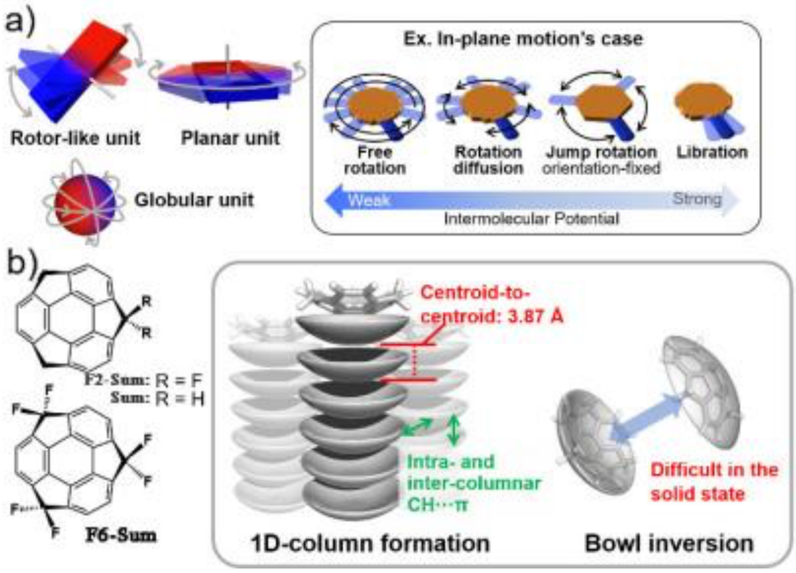

Fig. 2. a) Classical molecular motions of crystal dielectric materials. b) **Sum** and F-modified **Sum** materials designed in this work and characterization of **F2-Sum**.

Molecular motions are usually included in free rotation, leap rotation, libration, and rotational diffusion in the solid state.[11] For example, perdeuterated benzene exhibits in-plane rotation (nearly a $2\pi/6$ jump model) and restricted molecular plane vibration at 96-293K when it was trapped by tri-*ortho*-thymotide.[12] The molecular movement properties depend on their molecular structure and the intermolecular interactions. The complexes of curved aromatics with C_{60} moieties are frequently smooth. The classical example is C_{60} in the solid state, showing the rotated isotropically characteristics.[13] The smooth motion of C_{60} in the single-crystalline form can still kept even at low temperatures in a system when C_{60} is trapped in the finite single-wall carbon nanotubes.[14,15] These examples mentioned above demonstrate that in the solid state, curve-to-curve interactions allow the components to proceed a smooth molecular movements.

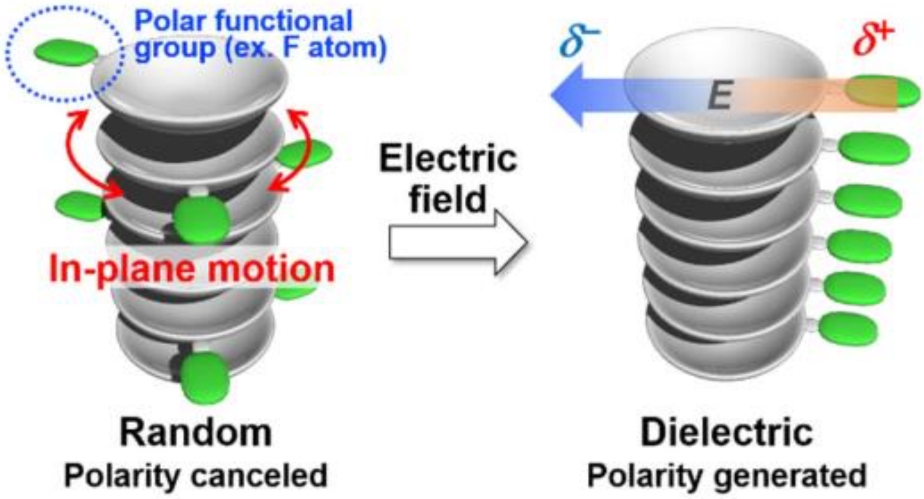

Fig. 3. The behavior of dielectric response movement in the plane of the bowl.

As mentioned in Chapter 1, **Sum** exhibits bowl inversion characteristics along the dipole in the solution state (Fig. 2b). This inversion-capable bowl is attractive for developing switchers. However, due to the generation of densely packed one-dimensional columns, the bowl inversion energy of **Sum** is very high in the solid state. Therefore, applying the bowl inversion of sumanene in the solid state is not straightforward; it is only used for 1,4,7-trithiasumanene derivatives, in which the simple bowl inversion is possible because of a much shallower bowl depth.[16]

In this chapter, the author explores **Sum**'s in-plane motion in a solid state and tries to exploit **Sum**'s motion to reveal its unique physical functional properties. In the packing structure of **Sum**, the benzylic sp^2 carbons and the bowl show two kinds of weak $CH\cdots\pi$ interactions; compared with intra-columnar $\pi\cdots\pi$ interactions, inter- and intra-columnar $CH\cdots\pi$ interactions are predominant. (bowl to bowl distance of **Sum**: 3.87 Å).[17] Compared with traditional planar π-conjugated compounds, the existence of the weaker π···π interactions of the curved π-conjugated compounds is beneficial in increasing flexibility for planar motion. In the meantime, the existence of the CH···π interaction helps to increase the crystal stability, as seen in a C_{60} complex,[18] which is hindering the planar motion. Understanding such conflicting effects in **Sum**'s crystal packing is important for future applications of sumanene derivatives, particularly the derivatives that make use of their planar motions.

Next, the author concentrated on installing a polar substituted functional group to generate the in-plane motion (Fig. 3) and resulting dielectricity simultaneously. The previously reported 1,1,4,4,7,7-hexafluorosumanene (**F6-Sum**), which installed six fluorine atoms on every benzyl position, served as a reference for this purpose.[19] X-ray single crystals analysis demonstrated **F6-Sum** possesses an isostructural packing structure with **Sum** in single crystal, showing that the insertion of fluorine atoms onto the sumanene moieties has no noticeable influence on their stacking structure because element fluorine and hydrogen have similar diameters. Taking advantage of this phenomenon, 1,1-difluorosumanene (**F2-Sum**) was developed, a compound with two fluorines on one benzyl position of **Sum**, resulting in a high dipole moment at the planar direction. As predicted, a single crystal of **F2-Sum** exhibited an isostructural packing structure with sumanene in the single crystal state. In addition, **F2-Sum** demonstrated a dielectric response behavior dependent on temperature due to its planar mobility in the crystal.

Section 2. Synthesis of F2-Sum

A modified version of a previously published synthesis route (Scheme 3) was used to synthesize 1,1-difluorosumanene (**F2-Sum**).[19] Sumanen-1-one[20] was protected to produce **4** in 92% yield. Following the previous procedure, the fluorination was first carried out at –30 ℃ to 25 ℃ with an excess amount of N-Iodosuccinimide(NIS) (20 equiv.) and Pyridine hydrofluoride(Py•HF)(100 equiv.) However, no desired **1** was observed and **4** was entirely consumed, assuming that the iodination of the aromatic part of **4** occurred at 25°C, resulting in multiple products that are difficult to analyze. Then, the equivalent of NIS was reduced to 2.48 equiv., and the reaction was conducted at –30 °C with 24.4 equiv. Py•HF generates **F2-Sum** in 77% yield successfully.

To study the influence of putting two fluorines on the benzyl of sumanene, **F2-Sum**'s structural and electrical characteristics were first characterized by DFT calculations (Fig. 4, Table 1).[21] The most stable structure of **F2-Sum** calculated by DFT revealed that the bowl depth of F2-Sum differs from the pristine sumanene and hexafluorosumanene. This was confirmed by that **F2-Sum** having a greater orbital axis vector (POAV) angle (8.9°) than **Sum** (8.7°); which helps evaluate the curvature of buckybowl and fullerene.[22]

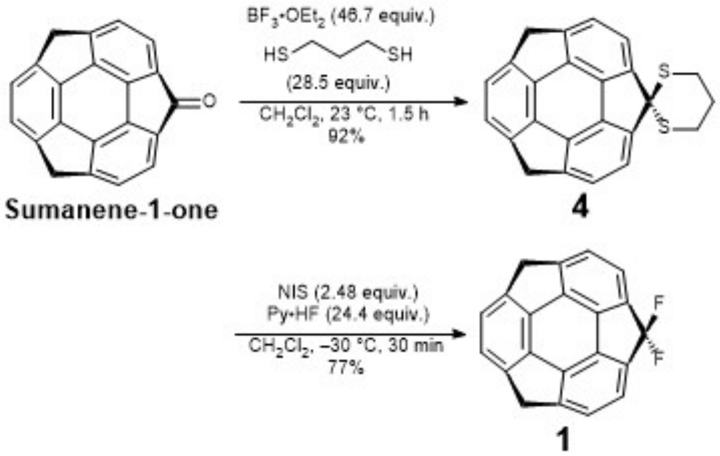

Scheme 3. Synthetic route of 1,1-difluorosumanene (**F2-Sum**).

Section 3. UV−Vis Absorption, cyclic voltammetry, x-ray

In the electronic structure of **F2-Sum**, it's obvious how the fluorine atom attracts the electrons from the whole molecule. (Fig. 4a). Consequently, **F2-Sum** has the biggest dipole moment compared with **Sum** and **F6-Sum**, and the value of the dipole moment is 3.62 Debye, whereas the in-plane dipoles in **Sum** and **F6-Sum** tend to cancel each other out due to their high symmetrical structures (Fig. 4b).

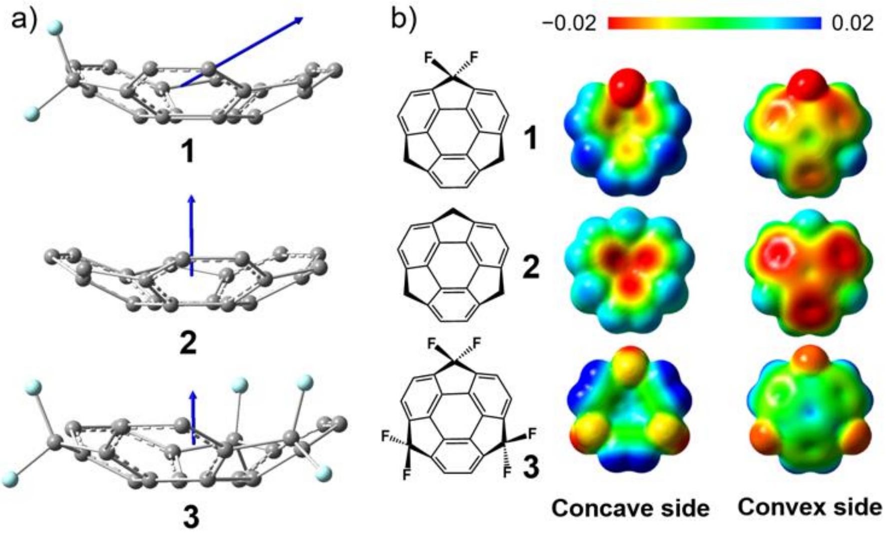

Fig. 4. DFT calculated electronic structures of **F2-Sum**, **Sum**, and **F6-Sum** (B3LYP/6-31G(d,p) level of theory). a) Directions of the dipole moment of **F2-Sum**, **Sum**, and **F6-Sum**. C is gray, F is pale-blue, H have been omitted for clarity. b) Maps of the electrostatic potential of **F2-Sum**, **Sum**, and **F6-Sum**.

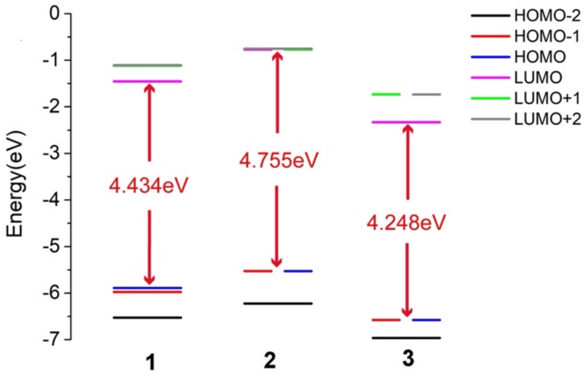

Fig. 5. DFT calculated the **energy graph of F2-Sum, Sum,** and **F6-Sum**.

As predicted, the energy level of HOMO and LUMO was reduced compared with **Sum** by the introduction of fluorine atoms but increased when compared to

F6-Sum (Fig. 5). UV-vis spectra and CV (cyclic voltammetry) reflected the electronic disturbance caused by fluorine atoms. The UV-vis spectra of **F2-Sum** revealed a maximum absorption peak at 273 nm, as well as a broad absorption peak caused by the electrical transitions of HOMO and LUMO, which locates at 350 nm (Fig. 6); the locations of these two absorption are in the middle of the case of **Sum** and **F6-Sum**.[19]

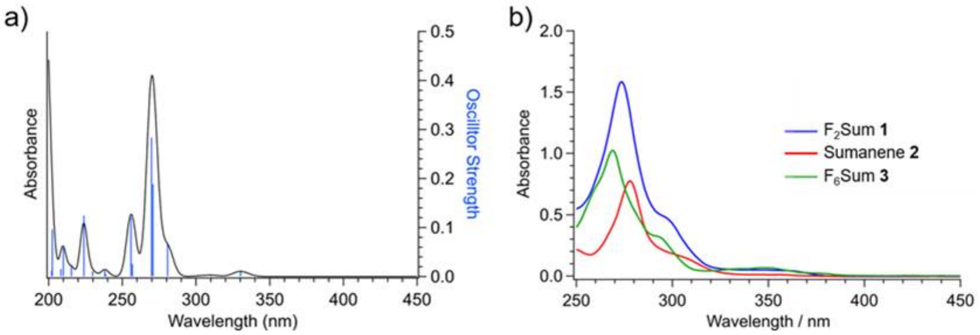

Fig. 6. F2-Sum UV-vis spectrum. a) DFT calculated figure (TD-B3LYP/6-31G++(d,p)). b) The experiment UV-vis data of **F2-Sum**, **Sum**, and **F6-Sum**. The concentration of **F2-Sum**, **Sum,** and **F6-Sum** is 1.0 × 10^{-5} M in DCM.

Table 1. Detailed construction parameters of **F2-sum**, **Sum**, and **F6-sum**. The values in parentheses are calculated by DFT(B3LYP/6-31G(d,p)).[21]

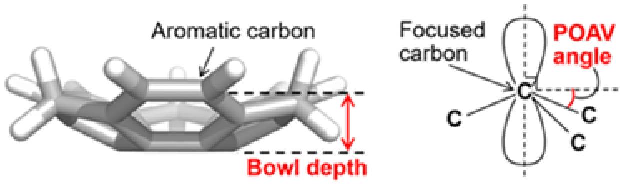

Compound	F2-Sum	Sum[17]	F6-Sum[19]
Bowl depth (Å)	1.16 (1.15)	1.11 (1.12)	1.24 (1.23)
POAV angle (°)	8.9 (9.0)	8.9 (8.7)	9.4 (9.3)
Dipole moment (D)	(3.62)	(1.94)	(1.22)

In comparison with **Sum**, CV data of **F2-Sum** in THF revealed a positive change in the peak of the reduction process. Irreversible reduction waves were seen at 2.64 V(E_p^{red1}), 2.89 V(E_p^{red2}) separately, under the Fc^0/Fc^+ pair condition (Fig. 7).

This result suggested that **F2-Sum** possesses higher electron-accepting ability than **Sum** (3.21 V), but lower than **F6-Sum** (1.79 V).[19]

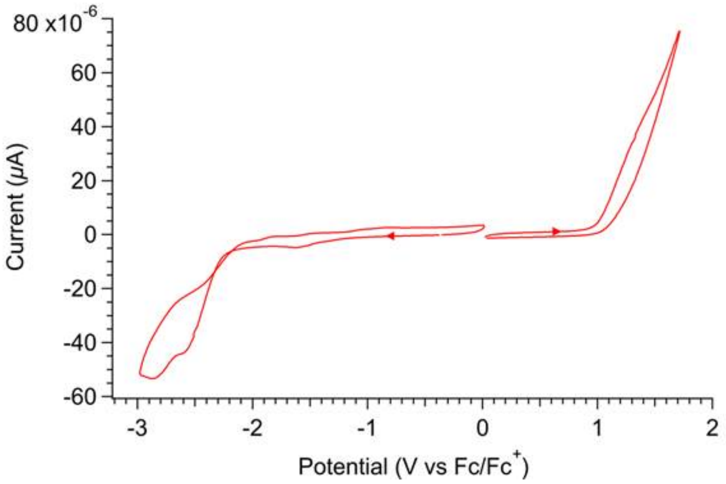

Fig. 7. Cyclic volt-ampere diagram of **F2-Sum**. The measurement conditions: concentration is 2.0 × 10^{-3} M in tetrahydrofuran, $[n\text{-}Bu_4N]^+[ClO_4]^-$ (0.1 M) was used as supporting electrolyte, the reference is Fc^0/Fc^+, the scan rate is 0.1 $V\cdot s^{-1}$ and the temperature is 294 K.

The single crystal structure confirmed the structural details of **F2-Sum**. Slow evaporation of a chloroform solution of **F2-Sum** yielded suitable single crystals of it. Despite having lesser molecular symmetry than C3-symmetric **Sum**, the packing structure of **F2-Sum** in the crystal is the isostructure with sumanene because of the tiny diameter of the fluorine element. The disorder of the fluorine atom with an occupancy factor of 0.33 (Fig. 8a) shows dipole cancellation in the crystalline state. The spatial structure of **F2-Sum** moieties has a distance of 1.16 Å from the top to the bottom of the bowl (bowl depth), which is greater than the distance of **Sum** without the fluorine substitution (1.11 Å). The structure data for the characterization of the single crystals are in agreement with the data calculated by the DFT, as shown in Table 1. The relative distance between the two **F2-Sum** units depends mainly on the relative distance between the two central hexagonal rings (bowl to bowl distance), which was 3.95 Å (Fig. 8b). This value was larger than in the case of **Sum** (3.86 Å). The inter-columnar distance was 9.662 Å, which is longer compared to the case of

Sum(9.570Å). This was probably explained by the partial presence of F···F interactions with the distance of 2.63 Å. (Fig. 8c)

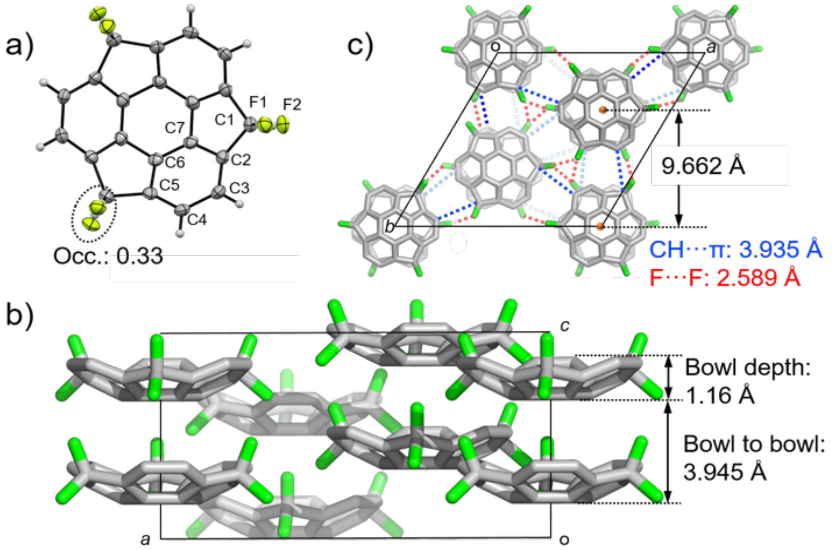

Fig. 8. Crystallization data of **F2-Sum** a) 50% probability of thermal displacement ellipsoid plot is **F2-Sum** crystal. Occupancy factors of F1 and F2 are 0.33 separately. b) The *a*-axis view of **Sum**. c) the *c*-axis view of **Sum**. CH···π interactions are blue dotted lines; F···F interactions are red dotted lines. C is gray, F is light green. H atoms are omitted for clarity.

Section 4. Specific heat measurement, VT-PXRD, VT-x-ray, VT-IR

Because the predicted packing structure was attained, thermal investigations were carried out to evaluate if **F2-Sum** is stable at high temperatures and to discover if phase transitions exist (Fig. 9). But the result indicated that there is no phase transition of **F2-Sum**. Then the specific heat experiment was conducted and there was an obvious absorption at 77 °C (Fig. 10), this result suggested that some molecular motion existed but did not influence the whole packing structure of **F2-Sum**.

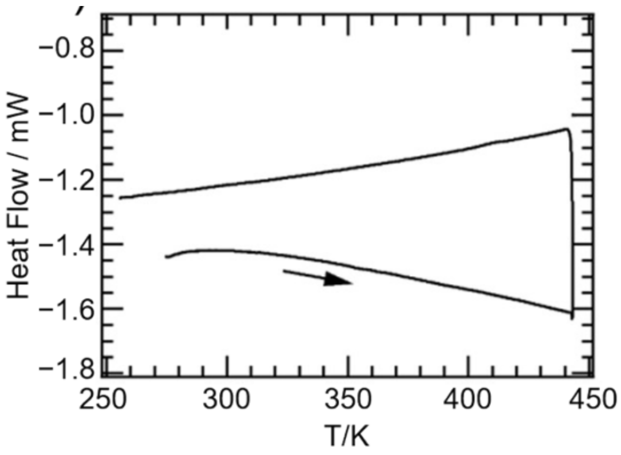

Fig. 9. DSC result of **F2-Sum**.

To evaluate the influence of the temperature on the structure, VT-PXRD was also employed (Fig. 11). There was an abrupt rise peak at roughly 2θ= 25°, namely 202 reflection, at 380 K (Fig. 11a, c), which is identical to the apparent peak seen during the heat-capacity test. It's clear that this 202 reflection slices the column in the simulated structure from the x-ray structure of **F2-Sum** (Fig. 11b).

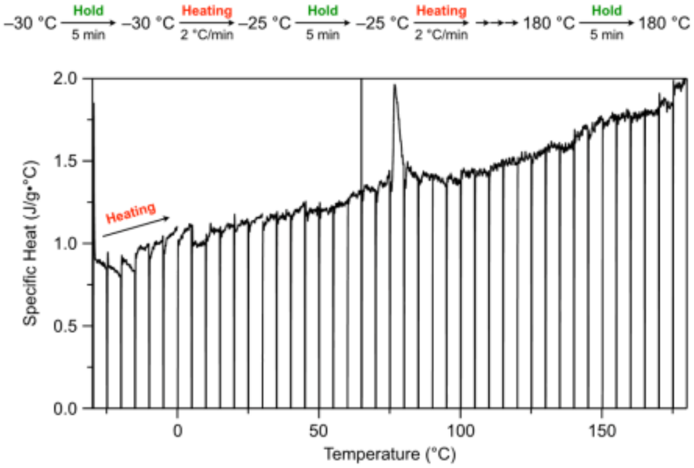

Fig. 10. The measurement of the specific heat for **F2-sum**.

As a result, the sharpening of the peak on heating suggests the decrease of the energy of the intermolecular bonds, and peak equalization happens due to significantly quick molecular motion. Characterization of the crystal structure of **F2-Sum** (Fig. 12) indicated that the cell size is increasing at 413 K compared with the case at the temperature of 100 K, but the length of the bonds and the bowl depth were similar (Fig. 13).

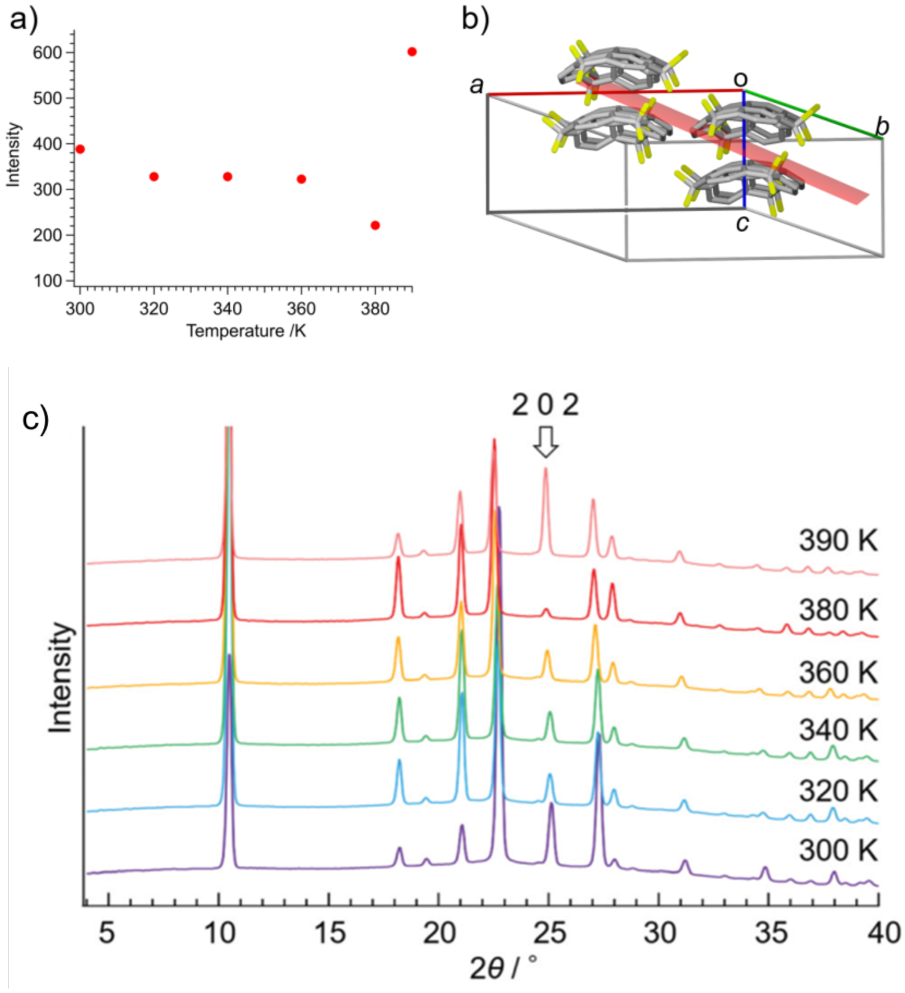

Fig. 11. a) Temperature dependent VT-PXRD characterization (around 2θ = 25°). b) The relationship between the the crystal structure and the crystal plane (one of (101) plane, red). c) TD-PXRD profile of powdered crystalline **F2 Sum**. The small arrows indicate the peak of the change in intensity at 380 K.

On the other hand, increasing temperature magnified each atom's displacement parameters as well, and the shape of the thermal ellipsoids correlated to planar motion (Fig. 13). These findings strongly support that a 120° planar fluctuation happens when the temperature increases (Fig. 14). Furthermore, an energy analysis by *CrystalExplorer* software revealed the existence of intercolumnar interaction in the system at 413 K, as well as a substantially greater intracolumnar interaction(Fig. 15).[23] This structural characteristic of **F2-Sum** lends weight to the hypothesis that these intercolumnar and intracolumnar interactions are the main factors to impede the molecular motion.

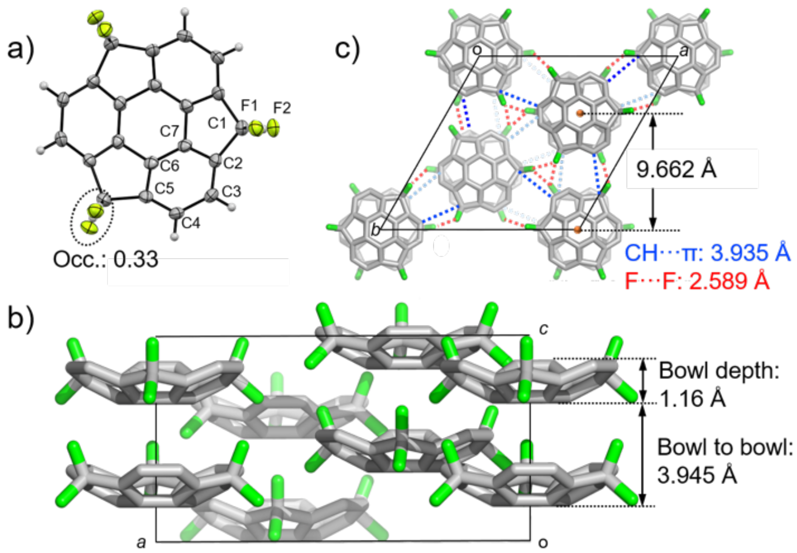

Fig. 12. Crystallisation data of **F2-Sum** at 413 K. a) Thermal displacement ellipsoid of **F2-Sum** in a crystal structure at 50% probability. Occupancy factors of F1 and F2 are 0.33 separately. b) View from the *a*-axis. c) C-axis view of the structure. The shortest C (aromatic)–C(benzylic) and F–F distances are indicated by blue and red dotted lines, respectively. C is gray, F is light green, H is omitted for clarity.

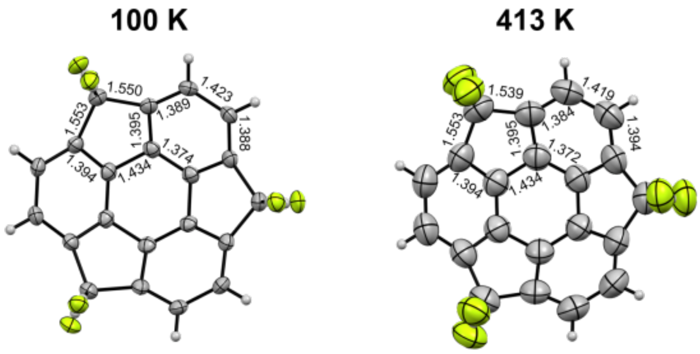

Fig. 13. Differences in the length of the bond and the size of the displacement ellipsoid at 100 K and 413 K.

More evidence was derived from VT-IR approach (Fig. 16). When a KBr pellet of **F2-Sum** was heated, the absorption measurements revealed a modest peak widening. Furthermore, at temperatures above 100 °C, a broad peak at around 1030 to 1200 cm^{-1}, which denotes the stretching of the C–F bond, shifted to a longer wavelength zone. Noticed, another absorption at roughly 780–810 cm^{-1} moved to a longer wavelength zone due to the benzylic C–H bending motion. These findings suggested that molecule movements altered about 100 °C, despite the fact that total inter-molecular interactions were intact at higher temperatures. The thermal analysis and TD-PXRD data support this assumption.

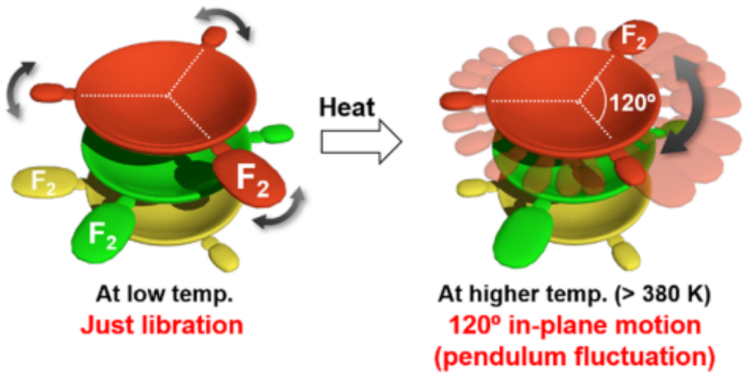

Fig. 14. Schematic diagram of temperature-dependent molecular motion in an **F2-Sum** stacked column. The white dotted line is used to describe the orientation of the molecules maintained in the crystal (the position of the three benzylic carbons).

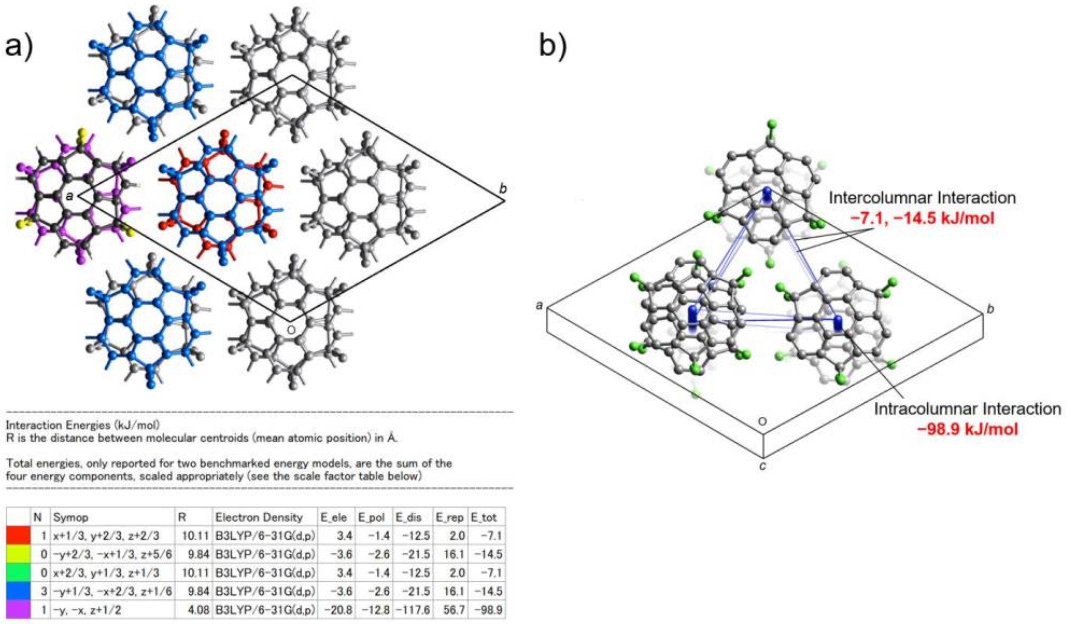

Interaction Energies (kJ/mol)
R is the distance between molecular centroids (mean atomic position) in Å.

Total energies, only reported for two benchmarked energy models, are the sum of the four energy components, scaled appropriately (see the scale factor table below)

	N	Symop	R	Electron Density	E_ele	E_pol	E_dis	E_rep	E_tot
🟥	1	x+1/3, y+2/3, z+2/3	10.11	B3LYP/6-31G(d,p)	3.4	−1.4	−12.5	2.0	−7.1
🟨	0	−y+2/3, −x+1/3, z+5/6	9.84	B3LYP/6-31G(d,p)	−3.6	−2.6	−21.5	16.1	−14.5
🟩	0	x+2/3, y+1/3, z+1/3	10.11	B3LYP/6-31G(d,p)	3.4	−1.4	−12.5	2.0	−7.1
🟦	3	−y+1/3, −x+2/3, z+1/6	9.84	B3LYP/6-31G(d,p)	−3.6	−2.6	−21.5	16.1	−14.5
🟪	1	−y, −x, z+1/2	4.08	B3LYP/6-31G(d,p)	−20.8	−12.8	−117.6	56.7	−98.9

Fig. 15. a) An energy framework shows the total interaction energy in the **F2-Sum** crystal structure at 413 K. b) The output file of the energy frame calculation and the interacting energy of **F2-Sum** at 413 K are color coded.

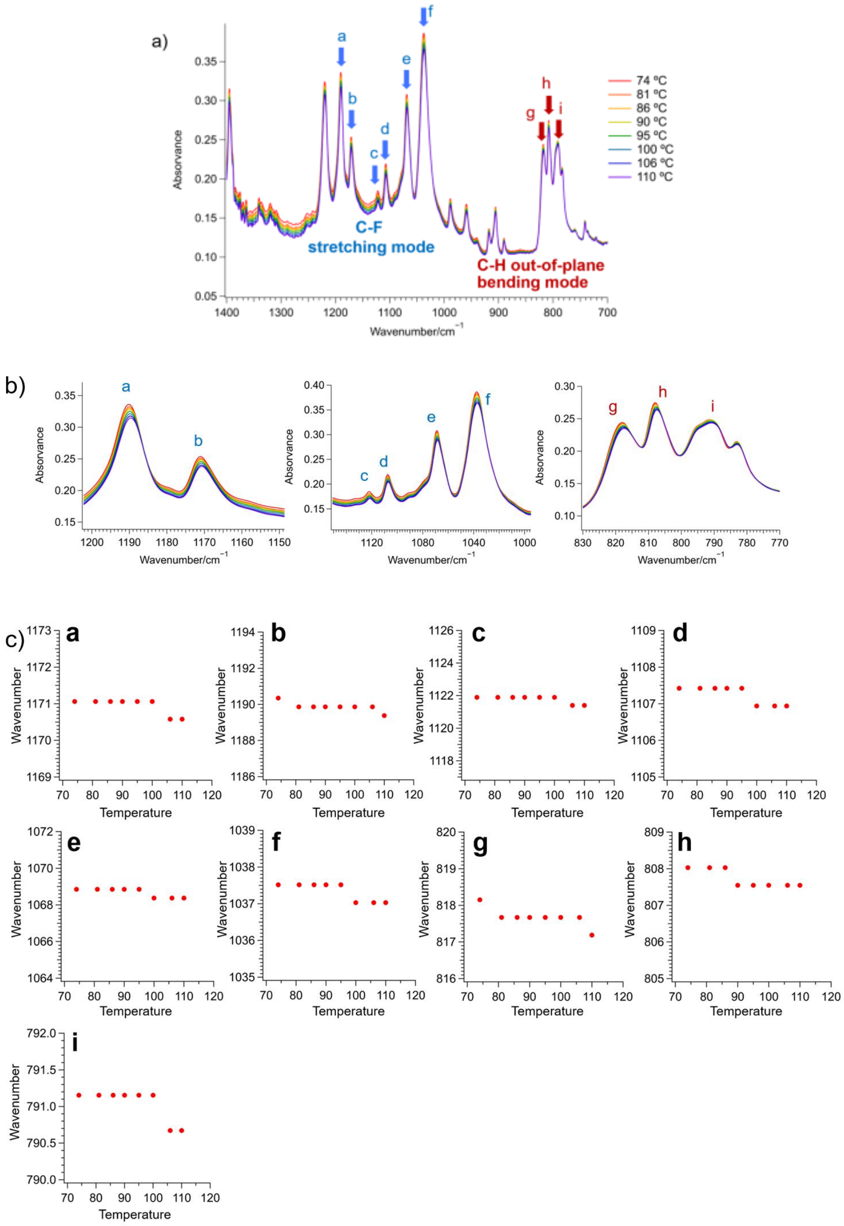

Fig. 16. VT-IR spectrum of **F2-Sum** at the temperature range of 74 °C~110 °C. All the data was obtained using ϕ = 7 mm KBr pellet of **F2-Sum** on a Cu plate with a heater. A thermocouple attached directly to the pellet was used to obtain the sample temperature. a) IR spectrum: blue represents C–F stretching, red represents bending modes C–H out of the plane. All peaks marked with arrows show a reduced wavenumber shift when heated. b) Enlarged image of each of the regions. c) Temperature-dependent change in the wave number at the top of the peak in every absorption band.

Section 5. Dielectric experiments

After confirming that **F2-Sum** exhibits 120° planar movement under high-temperature conditions in the solid state, dielectric experiments of **F2-Sum** and **F6-Sum** were conducted at multiple frequencies. **F2-Sum** exhibited a Debye-type relaxation. Over 360 K at 1 MHz, the dielectric constant is increasing (Fig. 17).

The phenomenon of the change happening at this range of temperature was consistent with the result mentioned before. The Arrhenius plot of **F2-Sum** revealed a linear connection (Fig. 18), and the activation energy E_a = 65 kJ/mol to trigger the molecular motion of **F2-Sum**. However, due to dipole cancellation in the in-plane direction, no apparent dielectric response was detected in the case of **F6-Sum** due to its high symmetry (Fig. 19).

In order to establish a more precise connection between the movements of molecules and the dielectrical performance of **F2-Sum**, the dielectric experiment of a sizable single crystal of **F2-Sum** was conducted by attaching two electrodes to it directly (Fig. 20). From the crystal packing direction of **F2-Sum** view from the *c*-axis (Fig. 21), there is no noticeable dielectricity (Figs. 21b and 21c). Conversely, from the viewing angle perpendicular to the π accumulation axis (Fig. 21), an obvious dielectric response was observed (Fig. 21d and 21e). The activation energy was 62 kJ/mol, which is consistent with the case of crystalline powdered **F2-Sum** (Fig. 17).

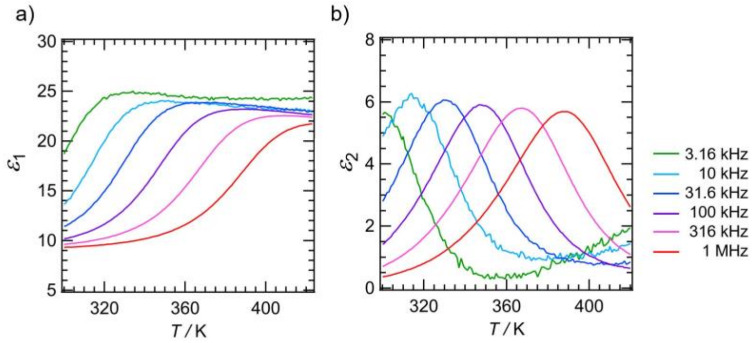

Fig. 17. Crystalline powder dielectric response of **F2-Sum**. a) The real and b) the imaginary of the dielectric constant of **F2-Sum** obtained by the heating process.

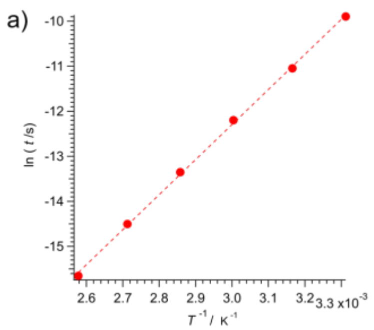

Fig. 18. The relaxation time τ of **F2-Sum** is an Arrhenius diagram in relation to the anti-temperature in a) Powder crystal particles and b) For a single crystal sample, the τ is the reciprocal of $\tau = 1/(2\pi f)$ measured f-value. The least squares fit of the data is shown by the dotted line.

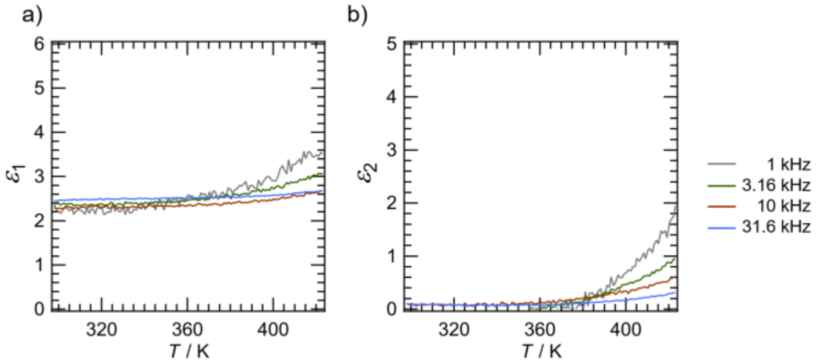

Fig. 19. Crystalline powder dielectric response of **F6-Sum**. a) The real and b) the imaginary parts of the dielectric constant of **F6-Sum** obtained by the heating process.

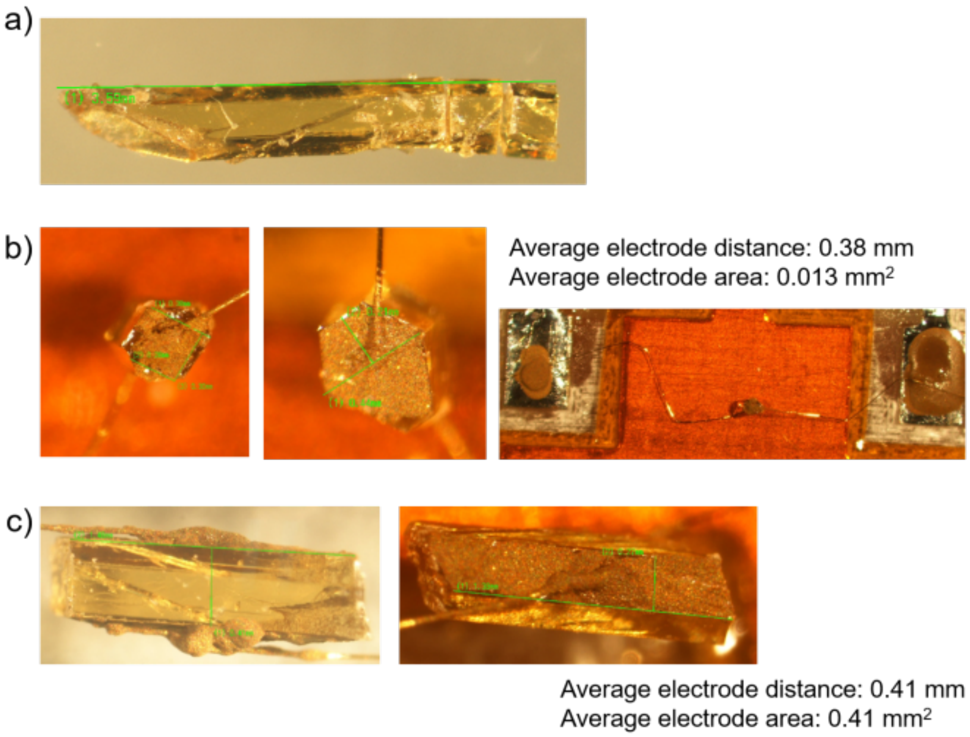

Average electrode distance: 0.38 mm
Average electrode area: 0.013 mm^2

Average electrode distance: 0.41 mm
Average electrode area: 0.41 mm^2

Fig. 20. Single-crystal sample for dielectric measurement. a) **F2-Sum** sample. b) Test set-up for the measurement of the dielectric response in the direction of the long axis. c) Test set-up for the measurement of the dielectric response in the direction of the short axis.

The anisotropic dielectric response of **F2-Sum** was confirmed by this experiment, and the activation energy is similar to some other organic dielectrics that experience phase transition under heating. These experiments demonstrate that reducing intracolumnar contacts, particularly CH···π interactions, is a crucial factor in developing novel switches from sumanene by utilizing its planar mobility.

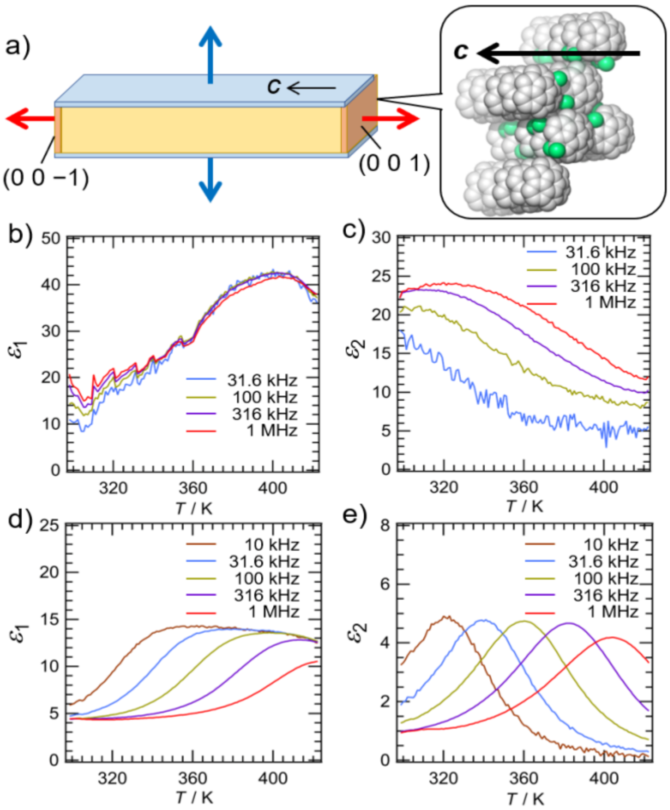

Fig. 21. a) Simplified model of the relationship between the shape of the **F2-sum** singular crystal and the external electric field. b) to e) Temperature dependence of b), d) the real part (ε1) and c), e) the imaginary part (ε_2) of the dielectric constant of **F2-Sum** in a single-crystalline form measured at various frequencies. The direction of the electric field applied for b) and c): parallel to the *c*-axis; for d) and e): orthogonal to the *c*-axis.

Section 6. Summary

In this chapter, a unique buckybowl, **F2-Sum** has been developed and synthesized. Compared with **Sum** and **F6-Sum, F2-Sum** possesses the largest dipole moment in the horizontal direction based on the DFT simulations result. During the heating process, **F2-Sum** happened a planar 120° pendulum swinging. Due to the special thermal properties of **F2-Sum**, its crystalline structure exhibited an anisotropic dielectric response, indicating that **F2-Sum** has in-plane motion in stacked columns. These, which focus on in-plane molecule motion in a buckybowl's π-stacking column, will contribute to accelerating the development of the dielectrics based on curved systems including buckybowls and fullerenes.

Experimental section

All chemicals were reagent grade and used as received if not mentioned. ^{1}H and ^{13}C NMR spectra were recorded on a JEOL JNM-ECS400 NMR spectrometer (^{1}H: 400 MHz and ^{13}C: 100 MHz). Chemical shift (δ) are expressed relative to the resonances of the residual non-deuterated solvent for ^{1}H ($CDCl_3$: ^{1}H(δ) = 7.26 ppm, $(CD_3)_2CO$: ^{1}H(δ) = 2.50 ppm) and for ^{13}C ($CDCl_3$: ^{13}C(δ) = 77.0 ppm, $(CD_3)_2CO$: ^{13}C(δ) = 39.52 ppm). High resolution mass spectra (HRMS) were measured using electron impact mode (EI) methods on JEOL JMS-777V spectrometer. Infrared spectra and UV-vis absorption spectra were recorded on a JASCO FTIR-4100 spectrometer and a JASCO V-670 spectrometer, respectively. VT-IR measurement was performed on a JASCO FTIR-4200 spectrometer with JASCO IRT-5000 FTIR microscope system. Electrochemical measurements were performed on a BAS ALS660A Electrochemical Measurement System for cyclic voltammetry. A standard three-electrode cell incorporating a glassy carbon (GC) as a working electrode, a Pt counter electrode and an $Ag/AgNO_3$ reference electrode was employed for electrochemical measurements. Specific heat measurement was carried out on a Perkin Elmer DSC 8500 differential scanning calorimeter, where temperature and enthalpy were calibrated with In (156.6 °C, 28.450 J/g) standard sample in a sealed Al pan. Specific heat profile was analyzed using the Perkin Elmer Pyris software. TG-DTA was carried out using a Rigaku Thermo Plus TG8120 thermal analysis station with Al_2O_3 reference under N_2. Differential scanning calorimetry (DSC) analysis was performed on a Mettler thermal analysis DSC1-TS station using an Al_2O_3 reference under N_2. Temperature-dependent powder X-ray diffraction patterns were collected on a Rigaku Rint-Ultima III diffractometer using Cu Kα radiation at λ = 0.154187 nm. Temperature-dependent dielectric constants were measured using the two-probe AC impedance method betIen 1000 and 1000 × 10^3 Hz (HP 4194A impedance/gain-phase analyzer, Hewlett-Packard). Electrical contacts were prepared using gold paste (Tokuriki 8560) to attach the 10 μm ϕ gold wires to the single crystal and the 25 μm ϕ gold wires to the 3 mm ϕ compressed pellet. Temperature control between 298 and 423 K was carried out using a Linkam LTS350 hot stage. Melting points were determined on a Standford Research Systems Optimelt MPA100 and were uncorrected. The preparative TLC (PTLC) purification was conducted using Wakogel B-5F PTLC plates. Elemental analyses were measured on a J-Science Micro corder JM10 at the Analysis Center in Osaka University.

1. Characterization

4,7-dihydrospiro[tricyclopenta[*def,jkl,pqr*]triphenylene-1,2'-[1,3]dithiane] (4)

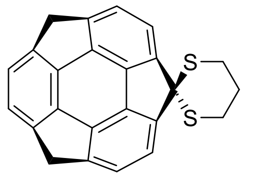

To a solution of sumanene-1-one[S1] (80.0 mg, 0.287 mmol, 100 mol%) in dry CH_2Cl_2 (132 mL) was added 1,3-Dithiopropane (0.820 mL, 8.18 mmol, 2850 mol %) and Boron trifluoride etherate (1.66 mL, 13.4 mmol, 4660 mol %). The reaction mixture was stirred at 23 °C for 1.5 h. After quenched with 10% NaOH aqueous solution, the organic layer was washed with sat. $NaHCO_3$ aq., dried over anhydrous Na_2SO_4, filtered and concentrated under reduced pressure. The residue was purified by silica gel chromatography by a eluent of Hexane:DCM = 2:1 to give the target product **4** as a white solid (97.0 mg, 92%).

mp: 59 °C; ^{1}H NMR ($CDCl_3$): δ (ppm) 7.37 (d, J = 8.0 Hz, 2H), 7.14 (s, 2H), 7.12 (d, J = 8.0 Hz, 2H), 4.71 (d, J = 20.0 Hz, 2H), 3.46 (d, J = 20.0 Hz, 2H), 3.32 (m, 4H), 2.34 (m, 2H); ^{13}C NMR (100 MHz, $CDCl_3$): δ (ppm) 154.94, 150.79, 149.00, 148.91, 148.85, 144.73, 124.15, 123.67, 121.76, 60.73, 41.91, 29.52, 28.82, 24.80; IR (KBr): 3047(s), 2949(s), 2938(s), 2893(vs), 1556(w), 1416(s), 1389(vs), 1268(vs), 1235(s), 1076(s), 914(s), 796(vs), 776(vs), 747(vs), 675(w), 630(s), 611(s), 566(s), 516(w); HRMS (EI) *m/z*: Calcd. for $C_{24}H_{16}S_2$ $[M]^+$ 368.0693, found: 368.0688.

1,1-difluoro-4,7-dihydro-1*H*-tricyclopenta[*def,jkl,pqr*]triphenylene (1,1-Difluorosumanene) (F2-Sum)

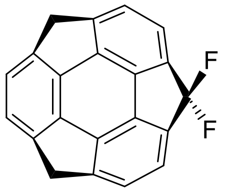

A carefully dried PP-tube was charged with *N*-iodosuccinimide (29.0 mg, 0.13 mmol, 250 mol %) and purged with N_2. CH_2Cl_2 (10.0 mL) was added by syringe and the mixture was cooled to -30 °C. Pyridine hydrofluoride (0.033 mL, 1.27 mmol, 2442 mol %) was added in one portion, then folloId by the dropwise addition of **4** (19.0 mg, 0.052 mmol, 100 mol %) in 4.00 mL dichloromethane. The mixture was stirred at -30 °C for 30 min. Then water and dichloromethane (30 mL) were added and the organic phase was washed with sat. $NaHCO_3$ aq., dried over anhydrous Na_2SO_4, filtered and concentrated under reduced pressure. The residue was purified by PTLC (Hexane/DCM = 2:1) to give the compound **1** as a white solid (12.0 mg, 77 %). Single crystal of **1** was obtained by the slow evaporation method using chloroform solution of **1.**

mp: 226 °C (dec.); ^{1}H NMR ($CDCl_3$, 400 MHz): δ (ppm) 7.20 (d, J = 8.0 Hz, 2H), 7.16 (s, 2H), 7.13 (d, J = 8.0 Hz, 2H), 4.72 (d, J = 20.0 Hz, 2H), 3.49 (d, J = 20.0 Hz, 2H); ^{13}C NMR ($CDCl_3$, 100 MHz): δ (ppm) 154.10, 149.24, 149.00, 148.79, 145.93 (dd, $^{3}J_{C\text{-}F}$ = 8.0, 3.0 Hz), 142.94 (t, $^{2}J_{C\text{-}F}$ = 27.0 Hz), 126.48 (t, $^{1}J_{C\text{-}F}$ = 258 Hz), 124.61, 124.03, 122.35, 42.01; ^{19}F-NMR ($(CD_3)_2CO$, 376 MHz): δ (ppm) −91.55 (d, J = 263 Hz), −117.05 (d, J = 244 Hz); IR (KBr): 3048(s), 2931(s), 2886(vs), 1570(w), 1446(w), 1393(vs), 1219(vs), 1189(vs), 1171(s), 1068(vs), 1035(vs), 906(s), 816(s), 804(vs), 288(vs), 739(s), 672(w), 607(s), 566(s), 543(w), 475(w); HRMS (EI) *m/z*: Calcd. for $C_{21}H_{10}F_2$ $[M]^+$ 300.0751, found: 300.0750. Elemental Analysis: Calcd. for $C_{21}H_{10}F_2(H_2O)_{0.2}$ C, 83.00; H, 3.45; Found: C, 83.12; H, 3.68.

2. Single crystal x-ray crystallography

The diffraction data for **F2-Sum** (at 100 K) was recorded on a DICTRIS PILATUS3 X CdTM 1M Detector System (λ = 0.43158 Å) at 100 K at SPring-8 BL02B1. The diffraction images were processed by using RIGAKU RAPID AUTO.

The diffraction data for **F2-Sum** (at 413 K) was recorded on an ADSC Q210 CCD area detector with a synchrotron radiation (λ =0.70000 Å) at 2D beamline in Pohang Accelerator Laboratory (PAL). The diffraction images were processed by using HKL3000.

All the structures were solved by direct methods (SHELXT-2015, 2018/2) and refined by full-matrix least squares calculations on F^2 (SHELXL-2018/3) using the Olex2 program package.

CCDC 2119515 (**F2-Sum** at 100 K) and 2119514 (**F2-Sum** at 413 K) contain the crystallographic data for this paper. These data can be obtained free of charge from The Cambridge Crystallographic Data Centre (https://www.ccdc.cam.ac.uk/).

F2-Sum (at 100 K): $C_{21}H_{10}F_2$, trigonal, space group $R3c$ (No. 161), $a = b$ = 16.735(2) Å, c = 7.889(2) Å, V = 1913.5(7) Å^3, ρ_{calcd} = 1.564 g/cm^3, Z = 6, 874 unique reflections out of 972 with $I > 2(I)$, 82 parameters, 3.43° < θ < 38.00°, R_1 = 0.0372, wR_2= 0.0964, GOF = 1.037.

F2-Sum (at 413 K): $C_{21}H_{10}F_2$, trigonal, space group $R3c$ (No. 161), $a = b$ = 16.872(2) Å, c = 8.169(2) Å, V = 2013.9(7) Å^3, ρ_{calcd} = 1.486 g/cm^3, Z = 6, 1156 unique reflections out of 1504 with $I > 2(I)$, 82 parameters, 4.387° < θ < 33.115°, R_1 = 0.0580, wR_2 = 0.1652, GOF = 1.070.

3. DFT calculation

All theoretical calculations were conducted by Gaussian09.[S7] The ground state structure optimization were performed at the B3LYP/6-31G(d,p) level of theory. Simulation of UV-vis spectrum were performed by TD-DFT (time-dependent density functional theory) at the B3LYP/6-31G++(d,p) level of theory using the optimized coordinates.

a)Optimized cartesian coordinates of **F2-Sum**

C	-0.72807	0.428827	1.408445
C	-0.76868	-0.77111	0.719841
C	-0.17103	-1.92834	1.221208
C	0.056953	-2.86406	0
C	-0.17103	-1.92834	-1.22121
C	0.379507	-1.85974	-2.50067
C	0.411167	-0.62104	-3.21784
H	0.903171	-2.71028	-2.92724
H	0.9536	-0.59868	-4.15942
C	-0.70008	1.671284	-0.69379
C	-0.70008	1.671284	0.693793
C	-0.04885	2.658975	1.439937
C	0.198928	2.068334	2.855508
C	-0.08488	0.55525	2.648005
C	0.411167	-0.62104	3.21784
C	0.379507	-1.85974	2.500672
H	1.224745	2.244169	3.194816
H	-0.46523	2.509762	3.610947
H	0.9536	-0.59868	4.159419
H	0.903171	-2.71028	2.927244
C	-0.76868	-0.77111	-0.71984
C	-0.72807	0.428827	-1.40845
C	-0.08488	0.55525	-2.64801
C	0.198928	2.068334	-2.85551
C	-0.04885	2.658975	-1.43994
C	0.4875	3.729063	-0.71512
C	0.4875	3.729063	0.715116
H	1.224745	2.244169	-3.19482
H	-0.46523	2.509762	-3.61095
H	1.032977	4.524418	-1.21683
H	1.032977	4.524418	1.216827
F	-0.80176	-3.93402	0
F	1.318809	-3.39181	0

b)Optimized cartesian coordinates of **Sum**

C	0.013492	-0.6845	1.409983
C	1.214202	-0.68451	0.716476
C	2.3657	-0.06667	1.214665
C	3.303022	0.186263	0
C	2.3657	-0.06667	-1.21467
C	2.279584	0.438276	-2.51725
C	1.040134	0.438454	-3.23296
H	3.120097	0.958107	-2.97065
H	1.012607	0.958554	-4.18741
C	-1.22737	-0.68449	-0.69331
C	-1.22737	-0.68449	0.693313
C	-2.23476	-0.06671	1.441288
C	-1.6517	0.186006	2.860477
C	-0.13098	-0.06665	2.656325
C	1.040134	0.438454	3.232955
C	2.279584	0.438276	2.517245
H	1.012607	0.958554	4.187409
H	3.120097	0.958107	2.970651
C	1.214202	-0.68451	-0.71648
C	0.013492	-0.6845	-1.40998
C	-0.13098	-0.06665	-2.65633
C	-1.6517	0.186006	-2.86048
C	-2.23476	-0.06671	-1.44129
C	-3.31974	0.43843	-0.71558
C	-3.31974	0.43843	0.71558
H	-4.13245	0.958537	-1.21683
H	-4.13245	0.958537	1.21683
H	4.171147	-0.48695	0
H	3.696913	1.207898	0
H	-1.84903	1.207442	3.201984
H	-2.08569	-0.48771	3.611889
H	-1.84903	1.207442	-3.20198
H	-2.08569	-0.48771	-3.61189

c)Optimized cartesian coordinates of **F6-Sum**

C	0.836277	0.017142	1.412196
C	0.836266	1.214478	0.720636
C	0.18084	2.346079	1.218828
C	-0.06975	3.278476	0
C	0.18084	2.346079	-1.21883
C	-0.39288	2.261021	-2.48438
C	-0.39279	1.020951	-3.20056
H	-0.96424	3.089247	-2.89217
H	-0.96406	0.960101	-4.12177
C	0.83618	-1.23089	-0.69136
C	0.83618	-1.23089	0.691356
C	0.181289	-2.22847	1.422151
C	-0.07007	-1.63926	2.839003
C	0.181185	-0.11748	2.641409
C	-0.39279	1.020951	3.200559
C	-0.39288	2.261021	2.484383
H	-0.96406	0.960101	4.121771
H	-0.96424	3.089247	2.892172
C	0.836266	1.214478	-0.72064
C	0.836277	0.017142	-1.4122
C	0.181185	-0.11748	-2.64141
C	-0.07007	-1.63926	-2.839
C	0.181289	-2.22847	-1.42215
C	-0.39139	-3.2827	-0.71598
C	-0.39139	-3.2827	0.71598
H	-0.96166	-4.05071	-1.22941
H	-0.96166	-4.05071	1.229414
F	-1.34038	3.775405	0
F	0.76996	4.359268	0
F	0.767675	-2.18102	3.775889
F	-1.34139	-1.88624	3.267849
F	-1.34139	-1.88624	-3.26785
F	0.767675	-2.18102	-3.77589

References

1. J. Brebels, J. V. Manca, L. Lutsen, D. Vanderzande, W. Maes, *J. Mater. Chem. A* **2017**, *5*, 24037.
2. R. D. Horansky, L. I. Clarke, J. C. Price, T.-A. V. Khuong, P. D. Jarowski, M. A. Garcia-Garibay, *Phys. Rev. B: Condens. Matter Mater. Phys*. **2005**, *72*, 014302.
3. T. Akutagawa, H. Koshinaka, D. Sato, S. Takeda, S.-I. Noro, H. Takahashi, R. Kumai, Y. Tokura, T. Nakamura, *Nat. Mater*. **2009**, *8*, 342.
4. W. Li, C.-T. He, Y. Zeng, C.-M. Ji, Z.-Y. Du, W.-X. Zhang, X.-M. Chen, *J. Am. Chem. Soc.* **2017**, *139*, 8086.
5. M. Tsurunaga, Y. Inagaki, H. Momma, E. Kwon, K. Yamaguchi, K.Yoza, W. Setaka, *Org. Lett.* **2018**, *20*, 6934.
6. J.-i. Ichikawa, N. Hoshino, T. Takeda, T. Akutagawa, *J. Am. Chem. Soc.* **2015**, *137*, 13155.
7. R. Bhowal, A. A. Balaraman, M. Ghosh, S. Dutta, K. K. Dey, D. Chopra, *J. Am. Chem. Soc*. **2021**, *143*, 1024.
8. J. Harada, M. Ohtani, Y. Takahashi,T. Inabe, *J. Am. Chem. Soc*. **2015**, *137*, 4477.
9. C. Shi, X. Zhang, Y. Cai, Y.-F. Yao, W. Zhang, *Angew. Chem., Int. Ed*. **2015**, *54*, 6206.
10. J. Harada, T. Shimojo, H. Oyamaguchi, H. Hasegawa, Y. Takahashi, K. Satomi, Y. Suzuki, J. Kawamata, T. Inabe, *Nat. Chem.* **2016**, *8*, 946.
11. J. N. Sherwood, The Plastically Crystalline State: Orientationally Disordered Crystals, Wiley, Chichester, **1979**.
12. A. E. Aliev, K. D. M. Harris, A. Mahdyarfar, *J. Chem. Soc. Faraday Trans.* **1995**, *91*, 2017.
13. P. A. Heiney, J. E. Fischer, A. R. McGhie, W. J. Romanow, A. M. Denenstein, J. P. McCauley, Jr., A. B. Smith, III, D. E. Cox, *Phys. Rev. Lett*. **1991**, *66*, 2911.
14. a) S. Sato, T. Yamasaki, H. Isobe, *Proc. Natl. Acad. Sci. U. S. A.* **2014**, *111*, 8374. b) T. Matsuno, Y. Nakai, S. Sato, Y. Maniwa, H. Isobe, *Nat. Commun*. **2018**, *9*, 1907.

15. S. Furukawa, J. Wu, M. Koyama, K. Hayashi, N. Hoshino, T. Takeda, Y. Suzuki, J. Kawamata, M. Saito and T. Akutagawa, *Nat. Commun.*, **2021**, *12*, 768.

16. S. Furukawa, J. Wu, M. Koyama, K. Hayashi, N. Hoshino, T. Takeda, Y. Suzuki, J. Kawamata, M. Saito, T. Akutagawa, *Nat. Commun.* **2021**, *12*, 768.

17. S. Mebs, M. Weber, P. Luger, B. M. Schmidt, H.Sakurai, S. Higashibayashi, S. Onogi, D. Lentz, *Org. Biomol. Chem.* **2012**, *10*, 2218.

18. Y. Yamamoto, E. Tsurumaki, K. Wakamatsu, S. Toyota, *Angew. Chem. Int. Ed.* **2018**, *57*, 8199.

19. B. M. Schmidt, B. Topolinski, S. Higashibayashi, T. Kojima, M. Kawano, D. Lentz, H. Sakurai, *Chem. Eur. J.* **2013**, *19*, 3282.

20. T. Amaya, M. Hifumi, M. Okada, Y. Shimizu, T. Moriuchi, K. Segawa, Y. Ando, T. Hirao, *J. Org. Chem*. **2011**, *76*, 8049.

21. M. J. Frisch, G. W. Trucks, H. B. Schlegel, G. E. Scuseria, M. A. Robb, J. R. Cheeseman, G. Scalmani, V. Barone, G. A. Petersson, H. Nakatsuji, X. Li, M. Caricato, A. Marenich, J. Bloino, B. G. Janesko, R. Gomperts, B. Mennucci, H. P. Hratchian, J. V. Ortiz, A. F. Izmaylov, J. L. Sonnenberg, D. Williams-Young, F. Ding, F. Lipparini, F. Egidi, J. Goings, B. Peng, A. Petrone, T. Henderson, D. Ranasinghe, V. G. Zakrzewski, J. Gao, N. Rega, G. Zheng, W. Liang, M. Hada, M. Ehara, K. Toyota, R. Fukuda, J. Hasegawa, M. Ishida, T. Nakajima, Y. Honda, O. Kitao, H. Nakai, T. Vreven, K. Throssell, J. A. Montgomery, Jr., J. E. Peralta, F. Ogliaro, M. Bearpark, J. J. Heyd, E. Brothers, K. N. Kudin, V. N. Staroverov, T. Keith, R. Kobayashi, J. Normand, K. Raghavachari, A. Rendell, J. C. Burant, S. S. Iyengar, J. Tomasi, M. Cossi, J. M. Millam, M. Klene, C. Adamo, R. Cammi, J. W. Ochterski, R. L. Martin, K. Morokuma, O. Farkas, J. B. Foresman and D. J. Fox, Gaussian 09, Revision D.01, Gaussian, Inc., Wallingford CT, 2013.

22. R. C. Haddon, *J. Am. Chem. Soc.* **1987**, *109*, 1676.

23. M. J. Turner, S. Grabowsky, D. Jayatilaka, M. A. Spackman, *J. Phys. Chem. Lett.* **2014**, *5*, 4249.

Chapter 3: Tuning the dielectric response by co-crystallisation of sumanene and its fluorinated derivative

Section 1. Introduction

After successfully witnessing **F2-Sum**'s dielectric properties generated by in-plane motion, the author set a goal to modify the dielectric property without using any chemicals. And the method is co-crystallization, which is a useful technique for bringing the disturbance of chemical structure and electric properties into complex molecules.[1-3] It is frequently employed in the drug manufacturing industry to increase solubility, hygroscopic properties, and compactness property[4,5] and manufacture other materials.[6-10] The parameters of two crystals can be reduced by preserving the identical packing structure of them. This approach, however, has certain conditions, such as the components having comparable structures, equivalent energies, and crystal growth dynamics behaviors.[11] Introducing a fluorine on the structure and cocrystallize it with the original molecule is an efficient strategy for producing cocrystals for the reason that the fluorine atom and hydrogen atom almost match in diameter,[12,13] this method is very useful for enhancing the ability to accept electrons or form large dipole moments.[14]

In Chapter 1, difluorosumanene (**F2-Sum**) was discovered to have a pendulum-type in-plane motion at temperatures over 380 K in the solid state.[15] Because of the existence of a large dipole moment caused by the fluoride installation, this phenomenon demonstrated an anisotropic dielectricity. **Sum** derivatives modified with fluorine atoms such as **F2-Sum** and **F6-Sum** have the same three-dimensional packing structure as **Sum**.[16] This unique property suggests that the preparation of cocrystal with **Sum** and **F2-Sum** or **F6-Sum** is a valuable option for tuning the permittivity characteristics (Fig. 22). A series of cocrystals composed of **F2-Sum** and **Sum** have been prepared in this work and the experimental results show that the dielectric characteristics were strongly influenced by percentage of **F2-Sum** in the cocrystals.

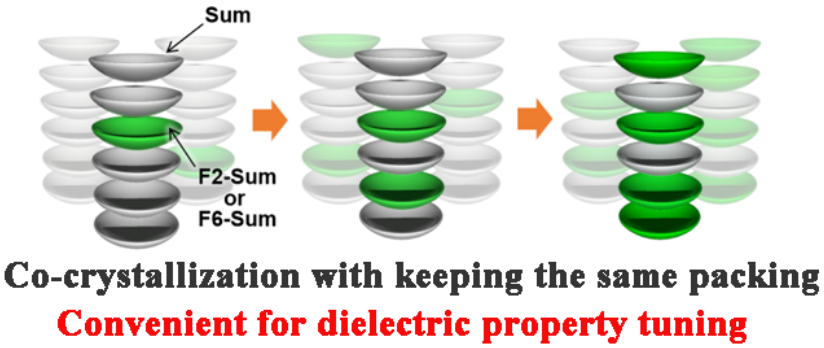

Fig. 22. Model of the strategy using co-crystallization to tune the dielectricity.

Table 2. Cell parameters of **Sum**, **F2-Sum**, and **F6-Sum** from single crystal X-ray data.

Compound	**Cell parameter (Å)** *a* and *b*	*c*	**Cell volume (Å^3)**
Sumanene	16.575	7.580	1803.45
Difluorosumanene	16.735	7.889	1913.49
Hexafluorosumanene	17.064	8.333	2101.33

Table 3. Structural parameters of **Sum**, **F2-Sum**, and **F6-Sum** in single-crystal X-ray analysis data at 100K.

Compound	**Bowl depth(Å)**	**Bowl-to-bowl distance(Å)**	**Intercolumnar Distance(Å)**
Sum[15]	1.11	3.86	9.56
F2-Sum	1.16	3.95	9.67
F6-Sum[15]	1.24	4.16	9.85

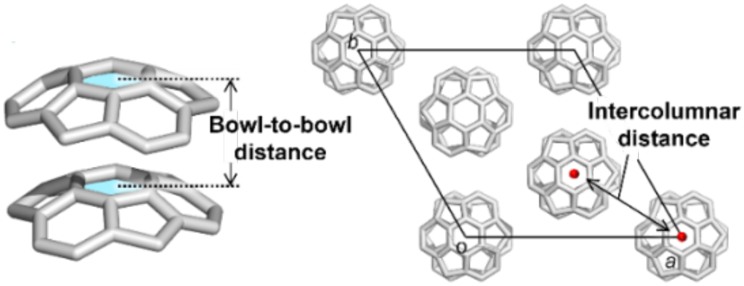

A necessary condition for the preparation of cocrystals is that the components have similar structures. After the fluorine atom was introduced into the benzyl group, the cell parameters of **F2-Sum** and **F6-Sum** are different from **Sum** (Table 2). Compared with **Sum**, **F2-Sum** and **F6-Sum** have a greater bowl to the bowl distance, because the atomic radius of a fluorine atom is greater than the atomic radius of a hydrogen atom. (Table 3).

Section 2. Co-crystallization

Based on these structural characteristics, co-crystals were first attempted by using the mixtures of **Sum** and **F6-Sum**, while **F6-Sum** had the greatest conformational variation with **Sum**. In chloroform, the crystallization process was set in a series of samples with varying proportions of sumanene and **F6-Sum** and then evaporated slowly. (Table 4).

Table 4. Co-crystallization of **F6-Sum** and **Sum**. Both **F6-Sum** (5.0 mg) in chloroform (1 mL) and **Sum** (3.5 mg) in chloroform (1 mL) were prepared (0.0134 mmol/mL each). They were mixed in various loading ratios (v/v) shown below and were left to stand for 24 h. [a] Prepared by slow diffusion method with hexane at 25 °C. [b] Prepared by slow evaporation method at 25 °C.

Loading ratio (F6-Sum:Sum)	Result
75:25[a]	Only **Sum** crystal
80:20[a]	Only **Sum** crystal
83:17[a]	No single crystal
50:50[b]	No single crystal

Unfortunately, **Sum** and **F6-Sum** did not form co-crystals, and there is one kind of single crystal - **Sum** was discovered. This result suggested that **F6-Sum** and **Sum** possess significant differences in structure, and it caused the failure of forming the cocrystal. Then the cocrystallizations of **F2-Sum** and **Sum** were carried out in various ratios (Table 5). As a consequence, cocrystallization of **Sum** and **F2-Sum** is succeeded in every setup. Although the loading ratio differs slightly from the results of ^{1}H NMR spectrum and single crystal diffraction characterization due to the formation of some amorphous structure, the characterization of the ratio of **Sum** and **F2-Sum** by ^{1}H NMR spectrum and XRD of the co-crystals showed a consistent trend(Table 6). In order to get more in-depth research results, a large scale of cocrystals with different proportions were prepared with **F2-Sum**/**Sum** loading ratios of 83:17, 50:50, and 35:65.

Table 5. Structural parameters of the co-crystals composed of **F2-Sum** and **Sum** prepared on a small scale. Both **F2-Sum** (5.0 mg) in chloroform (2 mL) and **Sum** (4.4 mg) in chloroform (2 mL) were prepared (0.0166 mmol/mL each). They were mixed in various loading ratios (v/v) shown below and were left to stand for 24 h at 25 °C to generate the co-crystals by slow evaporation of the solvent. The same procedure was applied for the scale-up preparation using 15 mg of **F2-Sum** in chloroform (6 mL) and 13.2 mg **Sum** in chloroform (6 mL) and mixed them in various loading ratios (v/v) shown below and were left to stand for 48 h at 25 °C to generate the co-crystals by slow evaporation of the solvent. [a] Based on several single crystals prepared in the same batch. The NMR charts are shown on later page. [b] Checked two different single crystals obtained from the same crystallization vial.

Loading ratio (F2-Sum:Sum)	**^{1}H NMR Ratio**[a]	**Cell parameter (Å)**		**X-ray ratio**	**Bowl Depth (Å)**	**Bowl to bowl distance (Å)**	**Crystal No.**
		a and *b*	*c*				
87:13[b]	83:17	16.7155(6)	7.8787(3)	81:19	1.161	3.939	**1**
		16.7139(6)	7.8744(3)	83:17	1.160	3.937	**2**
75:25[b]	75:25	16.7002(5)	7.8414(3)	71:29	1.153	3.921	**3**
		16.7127(9)	7.8468(5)	70:30	1.155	3.923	**4**
50:50	50:50	16.6500(6)	7.7389(3)	40:60	1.138	3.869	**5**
25:75	10:90	16.6137(8)	7.6344(6)	0:100	1.120	3.812	**6**
13:87[b]	4:96	16.5929(7)	7.6175(3)	0:100	1.118	3.809	**7**
		16.5959(7)	7.6226(3)	0:100	1.119	3.811	**8**

Table 6. Structural parameters of the co-crystals composed of difluorosumanene and sumanene prepared on a large scale.

Loading ratio (F2-Sum:Sum)	**Cell parameter (Å)**		**X-ray ratio**[a] **(F2-Sum:Sum)**	**Bowl depth (Å)**	**Bowl-to-bowl Distance (Å)**	**Crystal No.**
	a and *b*	*c*				
100:0	16.735(2)	7.889(2)	100:0	1.160	3.945	Ref. 42
87:13	16.755(1)	7.9305(7)	78:22	1.147	3.966	9
	16.723(1)	7.8675(7)	63:37	1.148	3.934	10
	16.740(2)	7.9040(8)	75:25	1.156	3.952	11
50:50	16.6665(3)	7.7333(2)	38:62	1.136	3.867	12
	16.6836(6)	7.7867(3)	46:54	1.143	3.894	13
	16.6650(5)	7.7508(3)	40:60	1.137	3.876	14
35:65	16.6264(4)	7.6483(2)	11:89	1.117	3.827	15
	16.6293(5)	7.6551(2)	11:89	1.122	3.828	16
	16.6267(4)	7.6522(2)	11:89	1.121	3.825	17
0:100	16.5754(5)	7.5796(5)	0:100	1.114	3.790	Ref. 17

Section 3. DFT calculation

Before presenting the experimentally acquired structures and co-crystal characteristics, the cause for co-crystallization failure was investigated in the system of **Sum** and **F6-Sum**. The interaction of **Sum** with **F6-Sum**, and the interaction of **Sum** with **F2-sum** were calculated by DFT separately (Fig. 23, 24).[17] For the calculation, vacuum conditions are selected and monomer units of the dimer are optimized to create appropriate models because the intra-columnar interaction was counted as the key factor.

From the calculated data, the best rotation angle of these dimers was 60° in all cases, which was consistent with the values of the case of **Sum**. And the bowl-to-bowl distance was set from 3.7Å to 4.0Å. While the bowl-to-bowl distance of **Sum** is 3.86 Å in the crystal structure, which is well match with the result calculated by DFT (3.85 Å). The result indicated that **Sum**/**F6-Sum** samples have different interaction energies at different bowl to bowl distance (Fig. 23, 24).

The interaction energies between different types dimer pairs show different interaction energies, with the interaction energy between **Sum** and **Sum** being comparable to that between **Sum** and **F2-Sum**, but larger than that between **Sum** and **F6-Sum.** Thus **F2-Sum** can successfully form cocrystal with **Sum**. On the contrary, **F6-Sum** cannot form cocrystal with **Sum**. (Table 7).

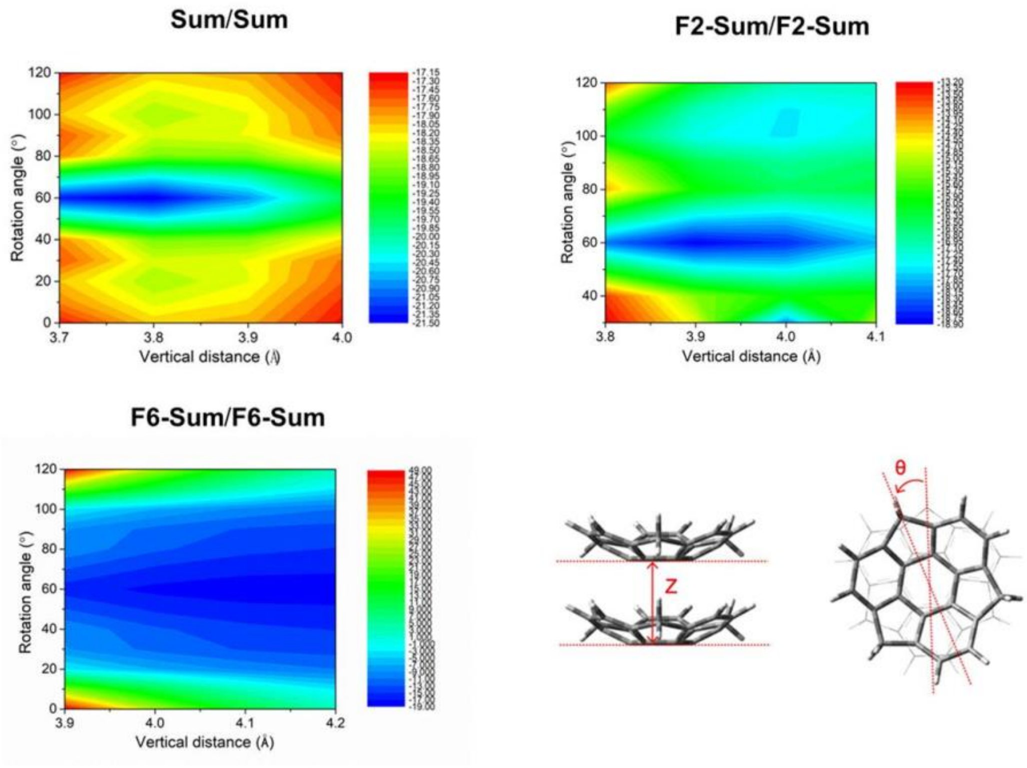

Fig. 23. The interaction energy surface of **Sum/Sum**, **F2-Sum/F2-Sum**, and **F6-Sum/F6-Sum** pairs. All calculations were performed at the ωb97xd/6-311+g(d,p) level of theory.

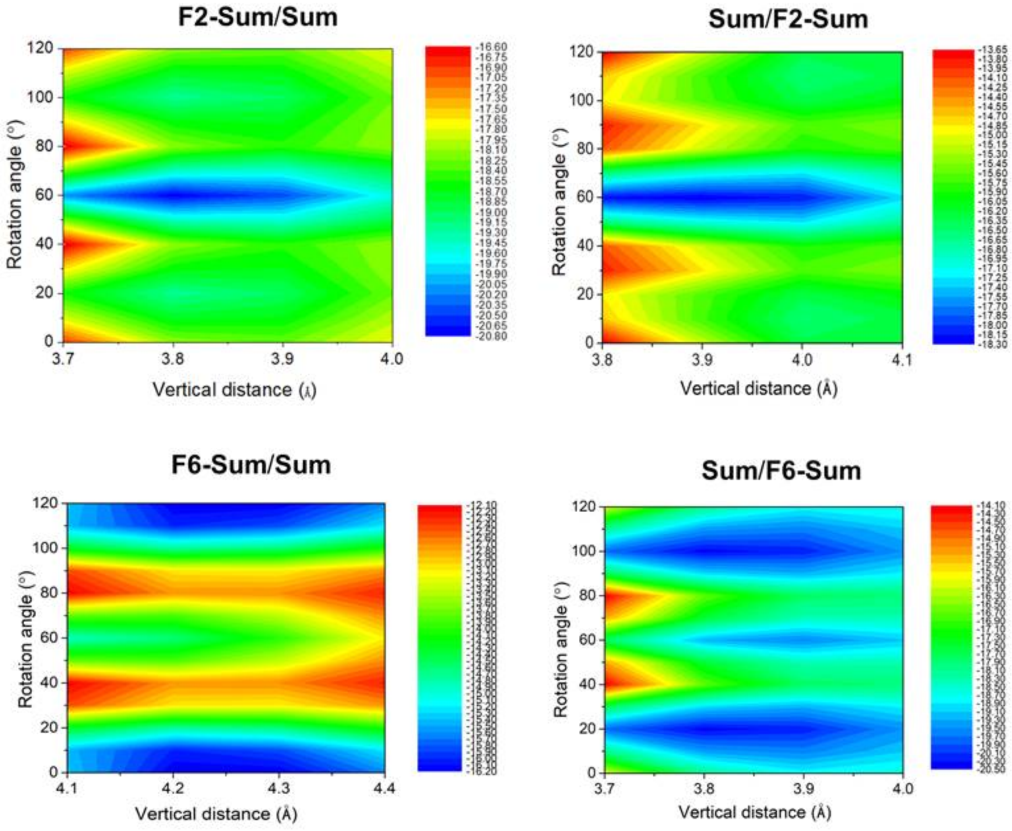

Fig. 24. The interaction energy surface for the **F2-Sum/Sum**, **Sum/F2-Sum**, and **F6-Sum/Sum**, **Sum/F6-Sum** pairs.

Table 7. Summary of interaction energies of the molecular pairs.

Dimer[a]	**Vertical distance Z (Å)**	**Rotation angle θ (°)**	***E* (kcal/mol)**
Sum/Sum	3.8	60	−21.50
F2-Sum/F2-Sum	3.9	60	−18.84
	3.9	180	−18.34
F6-Sum/F6-Sum	4.1	60	−18.01
F2-Sum/Sum	3.9	60	−18.52
Sum/F2-Sum	3.8	60	−20.77
F6-Sum/Sum	4.1	60	−14.90
Sum/F6-Sum	3.9	60	−19.55

Previous research about fluorine atoms disorder properties on the sumanene's methylene units was found in the prior study on **F2-Sum**.[15] The similar phenomenon is found in this work. The occupancy of the fluorine atoms in the co-crystals is influenced by the **F2-Sum** to **Sum** ratios. When **F2-Sum**'s composition increases in the cocrystal, the bowl depth and the bowl-to-bowl distance of the units are also relatively increased. A reasonable explanation for this phenomenon is that the fluorine atom has more atomic space than the hydrogen atom. There is also strong evidence that the *a* and *c* axis in cocrystals with different proportions of fluorine are linearly related to the percentage of **F2-Sum** (Fig. 25, Table 5, 6).

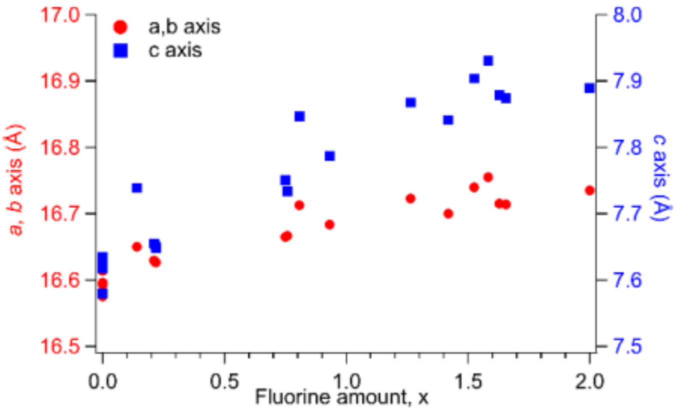

Fig. 25. The relationship between F amount in the formula and cell parameters in each co-crystal. The fluorine quantity is denoted as the value of "x" in the co-crystal formula C21H12-xFx.

Remarkably, compared with other axis data, the *c* axis showed a larger slope, suggesting the addition of fluorine had a great impact on increasing the bowl-to-bowl distance rather that column-to-column distance. Importantly, the physical properties of **Sum** can be tuned by alternating the proportion of **F2-Sum** in the cocrystal.

Section 4. Thermal properties and dielectric experiments

The thermal activities of three kinds of cocrystal samples were first investigated, which **F2-Sum/Sum** = 83:17, 50:50, and 35:65). And the influence of the ratio of **F2-Sum** on thermal activities has been studied (Fig. 26). The TG (thermogravimetry) experiment demonstrated that all three co-crystals were stable at temperatures lower than 177°C. Therefore, these samples have been characterized by the DSC measurement in the temperature range of –73°C to 152°C. During this heating process, there is no molecular movement in the crystals that causes the disorder of rotation, for the spectrum didn't show the trend of phase transition of the first order (Fig. 27).[15]

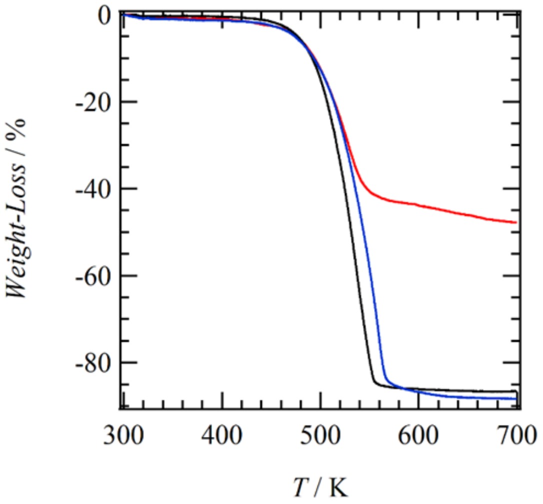

Fig. 26. TG (Thermo-gravimetry) experiments of the cocrystals composed of $(\textbf{F2-Sum})_{0.35}(\textbf{Sum})_{0.65}$ (blue line), $(\textbf{F2-Sum})_{0.5}(\textbf{Sum})_{0.5}$ (red line), $(\textbf{F2-Sum})_{0.87}(\textbf{Sum})_{0.13}$ (black line).

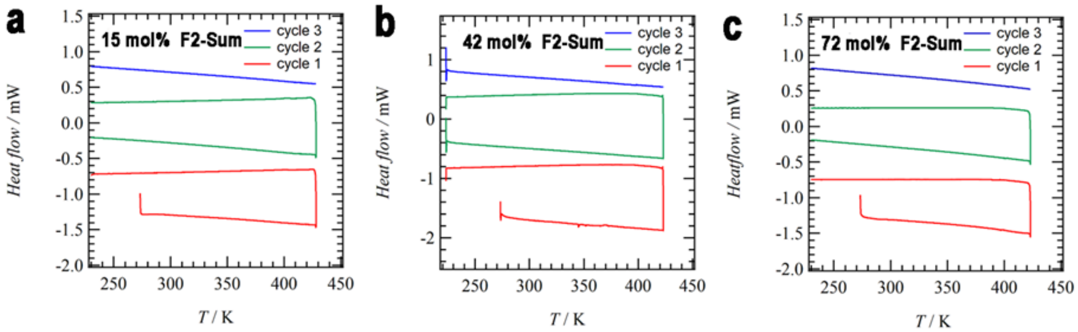

Fig. 27. DSC(Differential scanning calorimetry) experiments of the co-crystals of (a) **(F2-Sum)**$_{0.35}$**(Sum)**$_{0.65}$, (b) **(F2-Sum)**$_{0.5}$**(Sum)**$_{0.5}$, and (c) **(F2-Sum)**$_{0.87}$**(Sum)**$_{0.13}$.

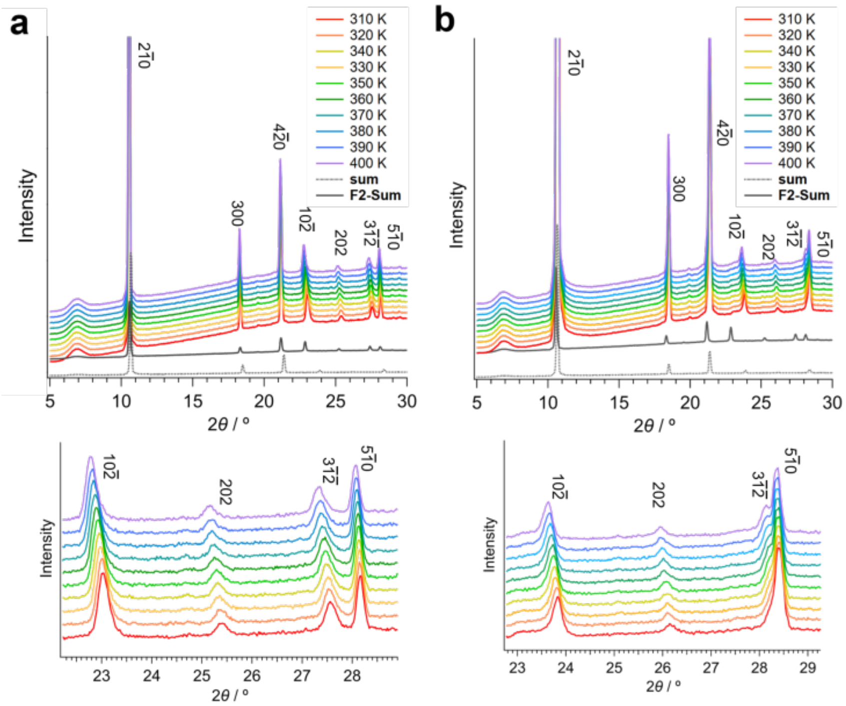

Fig. 28. Variable temperature PXRD data. The patterns of the co-crystalline powder of a) **(F2-Sum)**$_{0.87}$**(Sum)**$_{0.13,}$ b) **(F2-Sum)**$_{0.35}$**(Sum)**$_{0.65}$. The figures below each pattern show the magnified one in the 2*θ* range 23~29°.

VT-PXRD characterization of these samples revealed further information about their thermal behavior (Fig. 28). For the cocrystal **F2-Sum**/**Sum** = 83:17, noticeable peaks shift to low angles were detected at 2*θ* = 23.0°, 25.4°, and 27.6° at 310 - 390K, that were corresponding to (1 0 -2), (2 0 2), and (3 -1 -2) reflections, respectively. In the meantime, some other peaks corresponding to (2 -1 0), (3 0 0), and (4 -2 0) reflections remained nearly intact, which suggested that some motion of the molecule happens while the whole packing structure was kept under heating. The reflections corresponding to the angle of $2\theta = 23.0°$, $25.4°$, and $27.6°$ cut the packing column of the cocrystals. Whereas the resting reflections were corresponding to the same direction as the packing column stacks (Fig. 29). This result advised that the average distance of the samples is increasing while maintaining the direction of the column (Fig. 30). Given the previous work of **F2-Sum** exhibited planar motion under heating, and it's unable to confirm clear evidence of a first-order phase transition, similar molecular motion with **F2-Sum** in these cocrystals should happened in this case.

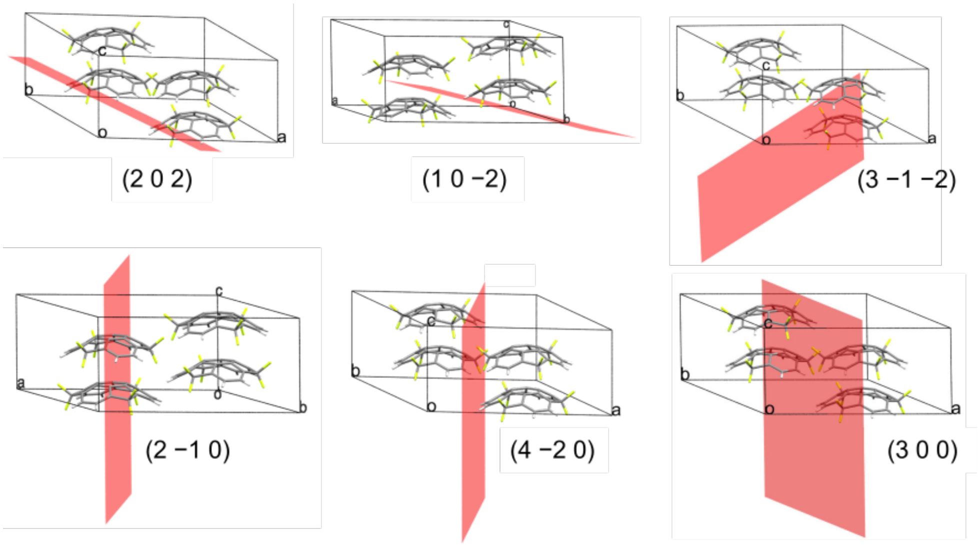

Fig. 29. Lattice plane and the structure relationships.

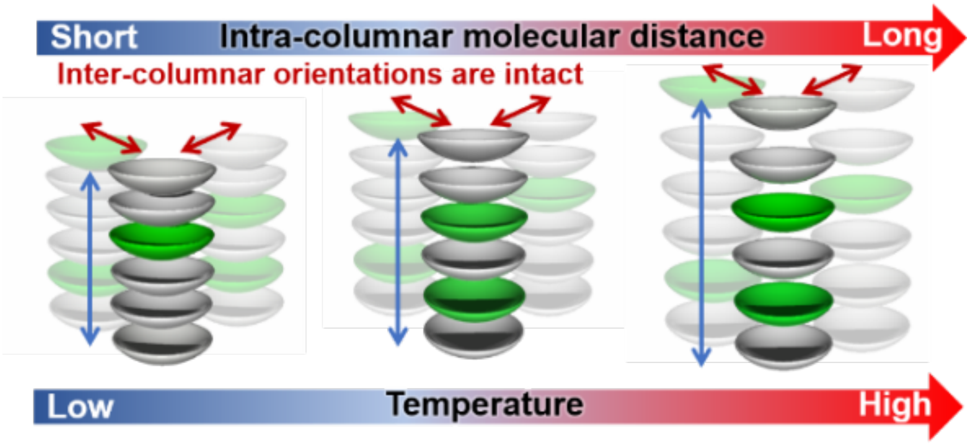

Fig. 30. The plausible model of the molecular motion in the co-crystals.

Dielectric spectroscopy was used to analyze the three cocrystals in crystalline powders state with the anticipation that they would display various dielectric behavior based on the different proportions of the two components of **F2-Sum** and **Sum** (Fig. 31). When **F2-Sum** was 87%, the sample displayed the strongest dielectric behavior, with the dielectric constant real part ε_1 and imaginary part ε_2 improved at 1000 kHz at 380 K (Fig.31e, f). As expected, when **F2-Sum** content was 50%, the sample showed a less obvious dielectric response (Figs. 31c and 31d). At 1000 kHz, both dielectric constants began to increase beyond 400 K, which means that more power is absorbed to get the same level of polarization as when **F2-Sum** is 87%. Finally, when **F2-Sum** was 35%, the sample showed the lowest dielectricity (Figs. 31a and 31b).

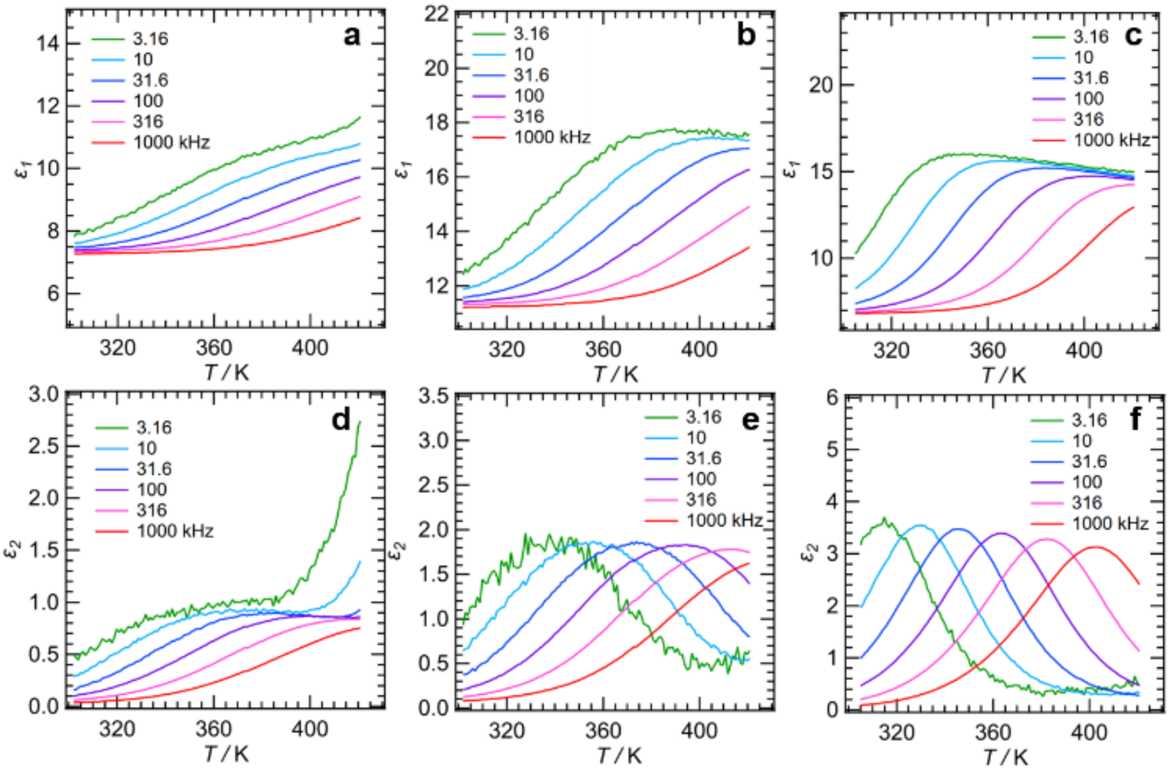

Fig. 31. Temperature dependence of the a), b) and c) real (ε1) and d), e) and f) imaginary (ε2) parts of the dielectric constants of **(F2-Sum)**$_{0.35}$**(Sum)**$_{0.65}$, **(F2-Sum)**$_{0.50}$**(Sum)**$_{0.50}$, and **(F2-Sum)**$_{0.87}$**(Sum)**$_{0.13}$, respectively.

The Arrhenius plot of each cocrystal revealed a linear connection (Fig. 32), and the activation energy E_a = 93 kJ/mol for **F2-Sum/Sum** = 0.35:0.65, 74 kJ/mol for **F2-Sum/Sum** = 0.5:0.5, 69 kJ/mol for **F2-Sum/Sum** = 0.87:0.13, respectively. Because the activation energy of the 100 mol% **F2-Sum** system is lower (65 kJ/mol), the E_a was higher in the cocrystal for the reason that the intra- and inter-interaction energy is increased along with the proportion of **F2-Sum**.

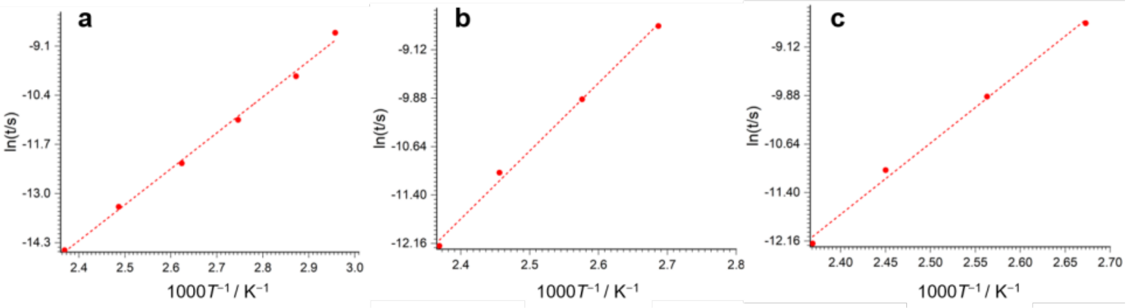

Fig. 32. Arrhenius plot. The relaxation time τ as a function of inverse temperature for a) (**F2-Sum**)$_{0.35}$(**Sum**)$_{0.65}$, b) (**F2-Sum**)$_{0.5}$(**Sum**)$_{0.5}$, and c) (**F2-Sum**)$_{0.87}$(**Sum**)$_{0.13}$ powder co-crystalline pellet, $\tau = 1/(2\pi f)$.

Section 5. Theoretical study

Furthermore, the inter- and intra-columnar interactions highly influence the dielectricity of the cocrystal, which differs for the studied molecule pairs, and they are composed of **Sum**/**Sum**, **F2-Sum**/**F2-Sum**, and **Sum**/**F2-Sum**. The EDA-FF decomposition analysis of interaction energy showed the interaction energies of these pairs based on the force field.[18,19]

To simplify the process of building the pair model, all the coordinates of the models were taken from the cif file of the cocrystals (see experimental section). Meanwhile, all the potential structures of pairings in the co-crystals were evaluated (Figs. 33-35 and Table 9-11).

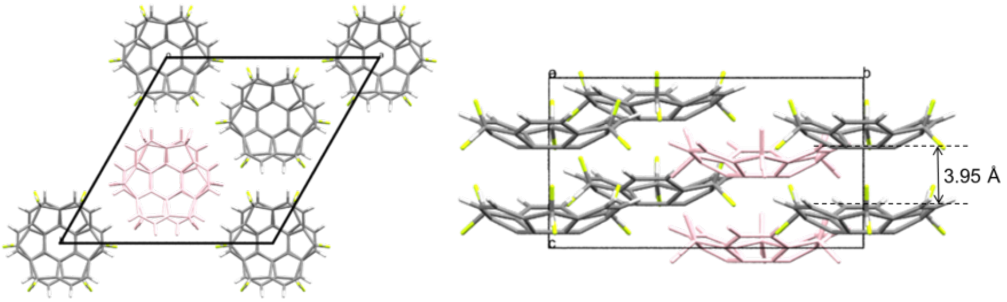

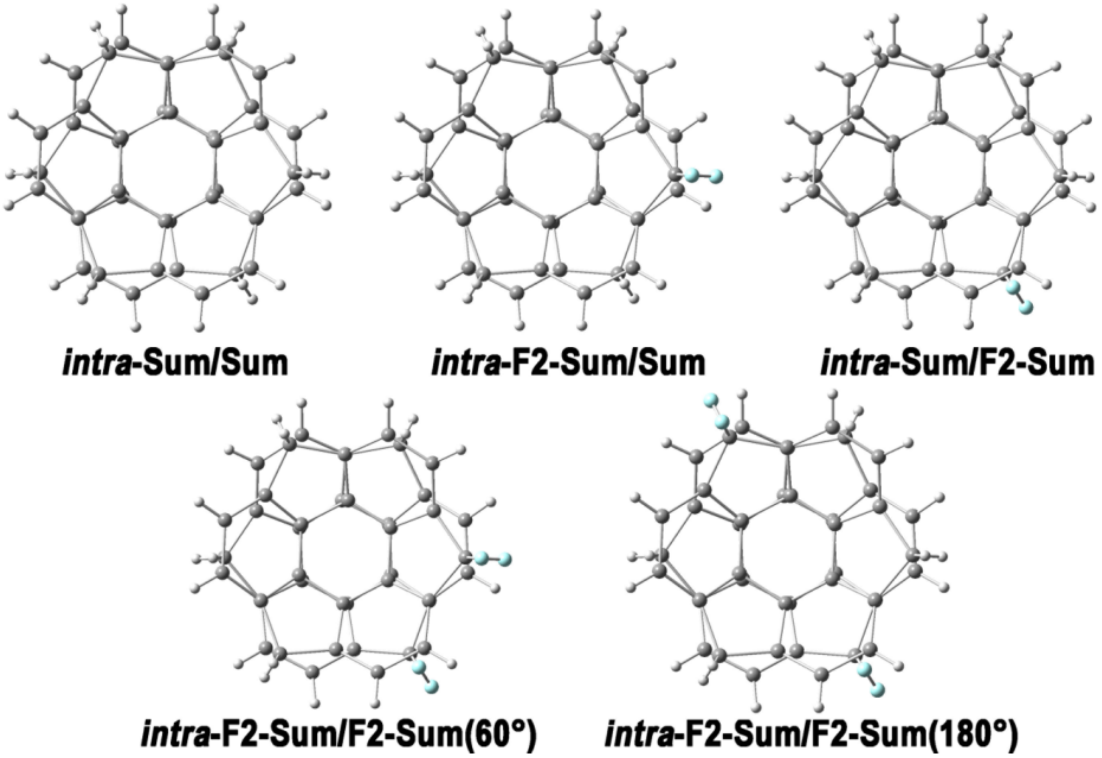

***intra*-Sum/Sum** ***intra*-F2-Sum/Sum** ***intra*-Sum/F2-Sum**

***intra*-F2-Sum/F2-Sum(60°)** ***intra*-F2-Sum/F2-Sum(180°)**

Fig. 33 Top view of molecular pairs used to calculate intra-columnar interactions. In **F2-Sum**/**F2-Sum** pairings, rotation angles of 60° and 180° correspond to the fluorine-attached two benzylic carbons. Carbon is gray; hydrogen is white; and fluorine is pastel blue.

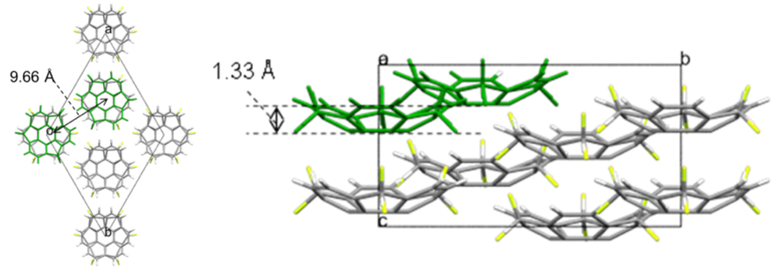

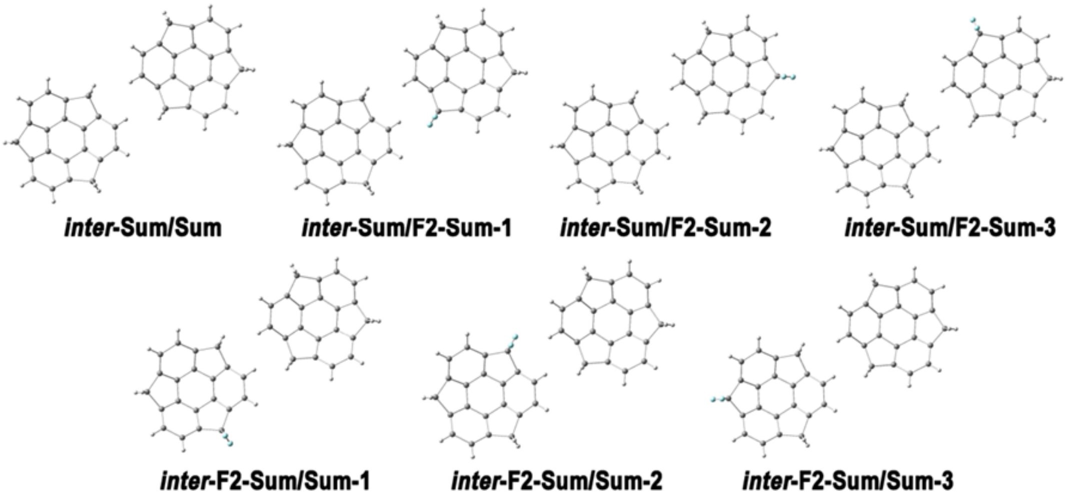

Figure 34. Top view of the molecular pairings (**Sum**/**Sum** and **Sum**/**F2-sum**) used to calculate intra-columnar interactions. Carbon is gray; hydrogen is white; and fluorine is pastel blue.

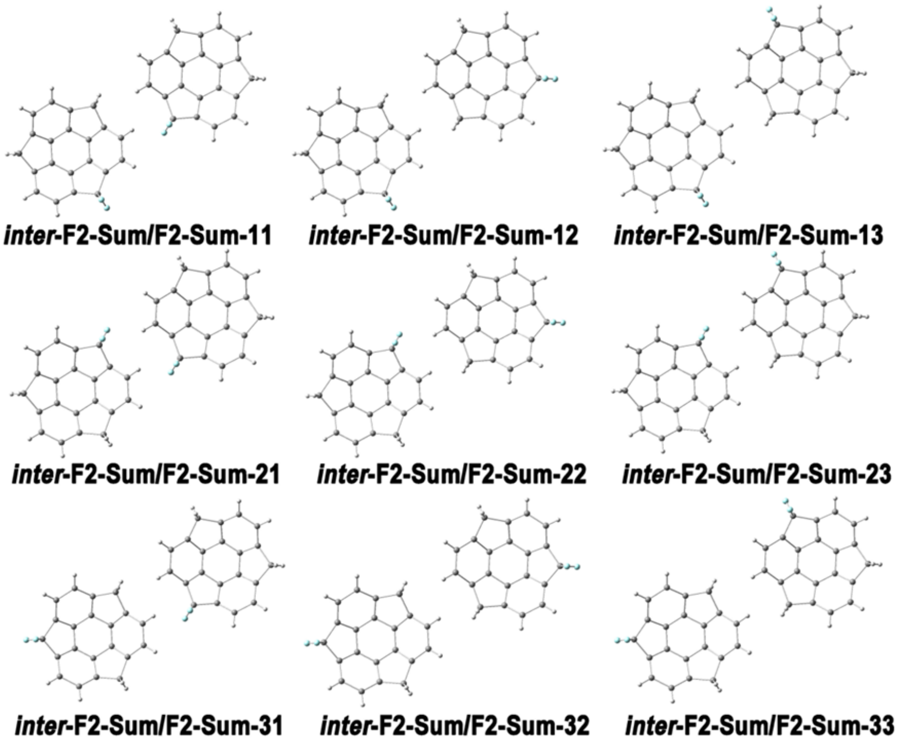

Figure 35. Top view of the molecular pairings (**F2-Sum**/**F2-Sum**) used to calculate intra-columnar interactions. Carbon is gray; hydrogen is white; and fluorine is pastel blue.

The computation revealed the dispersion force governs the interaction energy in every pair. The interaction energy of the *intra*-**Sum**/**Sum** pairs (72.4 kJ/mol, Table 9) is significantly higher than **F2-Sum**/**F2-Sum** pairs (67.9 kJ/mol(60° rotation), 68.0 kJ/mol (180° rotation)). In the instance of the combination of **Sum** and **F2-Sum**, the interaction energy is higher when **Sum** located at the upper position. Even while just the *intra*-**Sum**/**F2-Sum** had a little higher value than the *intra*-**Sum**/**Sum** pair, these findings revealed that the inclusion of **F2-Sum** in the pairs decreases overall intracolumnar interaction energy.

Table 9. Intra-columnar interaction energies of molecular dimers (**Sum**/**Sum**, **Sum**/**F2-Sum**, and **F2-Sum**/**F2-Sum**). D/R represents the ratio of dispersion energy to repulsion energy.

Molecular pair	Electrostatic (kJ/mol)	Repulsion (kJ/mol)	Dispersion (kJ/mol)	Total energy (kJ/mol)	D/R
***intra*-Sum/Sum**	−0.04	44.38	−116.75	−72.40	−2.63069
***intra*-F2-Sum/Sum**	2.4	56.99	−126.07	−66.67	−2.21214
***intra*-Sum/F2-Sum**	−1.34	49.34	−121.03	−73.03	−2.45298
***intra*-F2-Sum/F2-Sum (60°)**	0.45	61.97	−130.48	−68.05	−2.10553
***intra*-F2-Sum/F2-Sum (180°)**	0.44	61.95	−130.36	−67.97	−2.10428

Table 10. Inter-columnar interaction energies of molecule pairs (**Sum**/**Sum** and **Sum**/**F2-Sum**). D/R represents the ratio of dispersion energy to repulsion energy.

Molecular pair	Electrostatic (kJ/mol)	Repulsion (kJ/mol)	Dispersion (kJ/mol)	Total energy (kJ/mol)	D/R
***inter*-Sum/Sum**	0.16	4.23	−13.62	−9.22	−3.21986
***inter*-Sum/F2-Sum-1**	1.24	8.25	−17.75	−8.26	−2.15152
***inter*-Sum/F2-Sum-2**	0.17	4.23	−13.63	−9.22	−3.22222
***inter*-Sum/F2-Sum-3**	0.13	4.23	−13.67	−9.31	−3.23168
***inter*-F2-Sum/Sum-1**	0.48	4.23	−13.68	−8.97	−3.23404
***inter*-F2-Sum/Sum-2**	0.43	12.92	−18.16	−4.81	−1.40557

Table 11. Inter-columnar interaction energies of the molecular dimers (**F2-Sum**/**F2-Sum**).

Molecular pair	Electrostatic (kJ/mol)	Repulsion (kJ/mol)	Dispersion (kJ/mol)	Total energy (kJ/mol)	D/R
***inter*-F2-Sum/F2-Sum-11**	0.98	8.25	−17.84	−8.62	−2.16242
***inter*-F2-Sum/F2-Sum-12**	0.86	4.23	−13.69	−8.61	−3.23641
***inter*-F2-Sum/F2-Sum-13**	0.56	4.23	−13.74	−8.95	−3.24823

***inter*-F2-Sum/F2-Sum-21**	-2.05	16.95	−22.39	−7.49	−1.32094
***inter*-F2-Sum/F2-Sum-22**	-0.36	12.92	−18.17	−5.61	−1.40635
***inter*-F2-Sum/F2-Sum-23**	-0.07	12.92	−18.23	−5.38	−1.41099

In all circumstances, the interaction energies between the molecules in the columnar direction were governed by the dispersion forces, while the interaction energy of *inter*-**Sum**/**Sum** was 9.2 kJ/mol(Table 10). This value is greater than the energy of the **F2-Sum**/**F2-Sum** pairings (from 5.3 to 8.9 kJ/mol). The interaction energies of the five forms of *inter*-**Sum**/**F2-Sum** couples ranged from substantially lower to slightly higher than those of the **Sum**/**Sum** dimers(4.8 to 9.3 kJ/mol). Despite the fact that there are six forms of *inter*-**Sum**/**F2-Sum** pairs possessing higher intercolumnar interaction energies in specified molecular orientations(9.3 kJ/mol, Table 10), the effect of them was likely canceled by the unstable effect from other orientations. Therefore, elevating the ratio of **F2-Sum** in the cocrystal will resulting lower intra and inter-molecular interaction energies. Because the absolute values of inter-columnar energies are 8 times smaller than intra-columnar energies, suggesting that the intra-columnar interaction governs the dielectric constants of the co-crystals. Thus, increasing the ratio of **F2-Sum** will resulting a better dielectric response by enlarging the distance of the molecules in the column.

Section 6. Summary

Finally, the dielectric characteristics of co-crystalline systems were effectively tuned by changing the proportion of **Sum** and **F2-Sum**. The unique phenomenon has been explained by the in-depth examination of molecular orientations through detailed experiment characterization. These findings provide access to reveal how the different ratios of **F2-Sum** change the character of **Sum** and also provide an effective method to prepare the energy materials.

Experimental section

All the procedures follow as mentioned in the Chapter 2 unless otherwise noted. Temperature-dependent powder X-ray diffraction patterns were collected on a Rigaku Rint-Ultima III diffractometer using Cu Kα radiation at $\lambda = 0.154187$ nm.

1. Single crystal x-ray crystallography

The diffraction data for the cocrystals of F2-Sum and Sum from No. 1 to 8 were recorded on a XtaLAB Synergy with a Mo-target ($\lambda = 0.71073$ Å) equipped with a Rigaku HyPix-6000HE as the detector at 123 K in house.

The diffraction data for crystal No. 9 to 17 were recorded on a XtaLAB Synergy with a Cu-target ($\lambda = 1.54184$ Å) equipped with a Rigaku HyPix-6000HE as the detector at 123 K in house.

All the diffraction images were processed by using CrysAlisPro. All the structures were solved by direct methods (SHELXT-2015, 2018/2) and refined by full-matrix least squares calculations on F^2 (SHELXL-2018/3) using the Olex2 program package.

1: $C_{21}H_{10.37}F_{1.63}$, hexagonal, space group = $R3c$ (No. 161), $a = b = 16.7155(6)$ Å, $c = 7.8787(3)$ Å, $\alpha = \beta = 90^\circ$, $\gamma = 120^\circ$ $V = 1906.4(2)$ Å^3, $Z = 6$, $\rho_{\mathrm{calcd}} = 1.534$ g cm^{-1}. 1114 unique reflections out of 1139 with $I > 2\sigma(I)$, 83 parameters, $2.437^\circ < \theta < 31.013^\circ$, $R_1 = 0.0330$, w$R_2 = 0.0920$, GOF = 1.074. CCDC 2172504.

2: $C_7H_{3.45}F_{0.55}$, hexagonal, space group = $R3c$ (No. 161), $a = b = 16.7139(6)$ Å, $c = 7.8744(3)$ Å, $\alpha = \beta = 90^\circ$, $\gamma = 120^\circ$ $V = 1905.0(2)$ Å^3, $Z = 18$, $\rho_{\mathrm{calcd}} = 1.538$ g cm^{-1}. 1118 unique reflections out of 1134 with $I > 2\sigma(I)$, 83 parameters, $2.437^\circ < \theta < 30.744^\circ$, $R_1 = 0.0336$, w$R_2 = 0.0930$, GOF = 1.043. CCDC 2172505.

3: $C_7H_{3.53}F_{0.47}$, hexagonal, space group = $R3c$ (No. 161), $a = b = 16.7002(5)$ Å, $c = 7.8414(3)$ Å, $\alpha = \beta = 90^\circ$, $\gamma = 120^\circ$ $V = 1894.0(1)$ Å^3, $Z = 18$, $\rho_{\text{calcd}} = 1.525$ g cm^{-1}. 1084 unique reflections out of 1113 with $I > 2\sigma(I)$, 83 parameters, $2.439^\circ < \theta < 30.767^\circ$, $R_1 = 0.0342$, w$R_2 = 0.0936$, GOF = 1.035. CCDC 2172509.

4: $C_7H_{3.53}F_{0.47}$, hexagonal, space group = $R3c$ (No. 161), $a = b = 16.7127(9)$ Å, $c = 7.8468(5)$ Å, $\alpha = \beta = 90^\circ$, $\gamma = 120^\circ$ $V = 1898.1(2)$ Å^3, $Z = 18$, $\rho_{\text{calcd}} = 1.520$ g cm^{-1}. 944 unique reflections out of 973 with $I > 2\sigma(I)$, 83 parameters, $2.437^\circ < \theta < 30.793^\circ$, $R_1 = 0.0355$, w$R_2 = 0.0973$, GOF = 1.059. CCDC 2172508.

5: $C_{21}H_{11.19}F_{0.81}$, hexagonal, space group = $R3c$ (No. 161), $a = b = 16.6500(6)$ Å, $c = 7.7389(3)$ Å, $\alpha = \beta = 90^\circ$, $\gamma = 120^\circ$ $V = 1858.0(2)$ Å^3, $Z = 6$, $\rho_{\text{calcd}} = 1.495$ g cm^{-1}. 1073 unique reflections out of 1081 with $I > 2\sigma(I)$, 83 parameters, $2.446^\circ < \theta < 30.744^\circ$, $R_1 = 0.0333$, w$R_2 = 0.0933$, GOF = 1.067. CCDC 2172518.

6: $C_{21}H_{11.86}F_{0.14}$, hexagonal, space group = $R3c$ (No. 161), $a = b = 16.5968(5)$ Å, $c = 7.6249(3)$ Å, $\alpha = \beta = 90^\circ$, $\gamma = 120^\circ$ $V = 1818.9(1)$ Å^3, $Z = 6$, $\rho_{\text{calcd}} = 1.461$ g cm^{-1}. 1070 unique reflections out of 1080 with $I > 2\sigma(I)$, 73 parameters, $2.454^\circ < \theta < 30.692^\circ$, $R_1 = 0.0344$, w$R_2 = 0.0958$, GOF = 1.121. CCDC 2172515.

7: $C_{21}H_{12}$, hexagonal, space group = $R3c$ (No. 161), $a = b = 16.5929(7)$ Å, $c = 7.6175(3)$ Å, $\alpha = \beta = 90^\circ$, $\gamma = 120^\circ$ $V = 1816.3(2)$ Å^3, $Z = 6$, $\rho_{\text{calcd}} = 1.450$ g cm^{-1}. 1073 unique reflections out of 1086 with $I > 2\sigma(I)$, 64 parameters, $2.455^\circ < \theta < 30.873^\circ$, $R_1 = 0.0360$, w$R_2 = 0.1000$, GOF = 1.096. CCDC 2172506.

8: $C_{21}H_{12}$, hexagonal, space group = $R3c$ (No. 161), $a = b = 16.5959(7)$ Å, $c = 7.6226(3)$ Å, $\alpha = \beta = 90^\circ$, $\gamma = 120^\circ$ $V = 1818.2(2)$ Å^3, $Z = 6$, $\rho_{\text{calcd}} = 1.448$ g cm^{-1}. 1083 unique reflections out of 1097 with $I > 2\ \sigma(I)$, 64 parameters, $2.454° < \theta < 30.840°$, $R_1 = 0.0362$, w$R_2 = 0.1021$, GOF = 1.071. CCDC 2172507.

9: $C_{21}H_{10.42}F_{1.58}$, hexagonal, space group = $R3c$ (No. 161), $a = b = 16.755(1)$ Å, $c = 7.9305(7)$ Å, $\alpha = \beta = 90°$, $\gamma = 120°$ $V = 1928.1(3)$ Å^3, $Z = 6$, $\rho_{calcd} = 1.513$ g cm^{-1}. 753 unique reflections out of 802 with $I > 2\sigma(I)$, 83 parameters, $5.280° < \theta < 75.048°$, $R_1 = 0.0762$, w$R_2 = 0.2157$, GOF = 1.142. CCDC 2172516.

10: $C_{21}H_{10.79}F_{1.21}$, hexagonal, space group = $R3c$ (No. 161), $a = b = 16.723(1)$ Å, $c = 7.8675(7)$ Å, $\alpha = \beta = 90°$, $\gamma = 120°$ $V = 1905.4(3)$ Å^3, $Z = 6$, $\rho_{calcd} = 1.469$ g cm^{-1}. 705 unique reflections out of 746 with $I > 2\sigma(I)$, 83 parameters, $5.290° < \theta < 75.814°$, $R_1 = 0.0627$, w$R_2 = 0.1685$, GOF = 1.078. CCDC 2172512.

11: $C_{21}H_{10.47}F_{1.53}$, hexagonal, space group = $R3c$ (No. 161), $a = b = 16.740(2)$ Å, $c = 7.9040(8)$ Å, $\alpha = \beta = 90°$, $\gamma = 120°$ $V = 1918.2(4)$ Å^3, $Z = 6$, $\rho_{calcd} = 1.515$ g cm^{-1}. 754 unique reflections out of 811 with $I > 2\sigma(I)$, 83 parameters, $5.285° < \theta < 75.377°$, $R_1 = 0.0772$, w$R_2 = 0.1976$, GOF = 1.096. CCDC 2172510

12: $C_{21}H_{11.24}F_{0.76}$, hexagonal, space group = $R3c$ (No. 161), $a = b = 16.6665(3)$ Å, $c = 7.7333(2)$ Å, $\alpha = \beta = 90°$, $\gamma = 120°$ $V = 1860.30(8)$ Å^3, $Z = 6$, $\rho_{calcd} = 1.489$ g cm^{-1}. 604 unique reflections out of 609 with $I > 2\sigma(I)$, 83 parameters, $5.308° < \theta < 76.051°$, $R_1 = 0.036$, w$R_2 = 0.0901$, GOF = 1.151. CCDC 2172511.

13: $C_{21}H_{11.07}F_{0.93}$, hexagonal, space group = $R3c$ (No. 161), $a = b = 16.6836(6)$ Å, $c = 7.7867(3)$ Å, $\alpha = \beta = 90°$, $\gamma = 120°$ $V = 1877.0(2)$ Å^3, $Z = 6$, $\rho_{calcd} = 1.492$ g cm^{-1}. 559 unique reflections out of 563 with $I > 2\sigma(I)$, 83 parameters, $5.303° < \theta < 75.236°$, $R_1 = 0.0366$, w$R_2 = 0.0972$, GOF = 1.107. CCDC 2172517.

14: $C_{21}H_{11.19}F_{0.81}$, hexagonal, space group = $R3c$ (No. 161), $a = b = 16.6650(5)$ Å, $c = 7.7508(3)$ Å, $\alpha = \beta = 90^\circ$, $\gamma = 120^\circ$ $V = 1864.18(3)$ Å^3, $Z = 6$, $\rho_{\text{calcd}} = 1.489$ g cm^{-1}. 596 unique reflections out of 596 with $I > 2\sigma(I)$, 83 parameters, $5.309° < \theta < 75.489°$, $R_1 = 0.0327$, wR_2 = 0.0857, GOF = 1.061. CCDC 2172513.

15: $C_{12}H_{11.78}F_{0.22}$, hexagonal, space group = $R3c$ (No. 161), $a = b = 16.6264(4)$ Å, $c = 7.6483(2)$ Å, $\alpha = \beta = 90^\circ$, $\gamma = 120^\circ$ $V = 1831.0(1)$ Å^3, $Z = 6$, $\rho_{\text{calcd}} = 1.460$ g cm^{-1}. 761 unique reflections out of 765 with $I > 2\sigma(I)$, 73 parameters, $5.321° < \theta < 76.056°$, $R_1 = 0.0401$, wR_2 = 0.1131, GOF = 1.153. CCDC 2172514.

16: $C_{12}H_{11.79}F_{0.21}$, hexagonal, space group = $R3c$ (No. 161), $a = b = 16.6293(5)$ Å, $c = 7.6551(2)$ Å, $\alpha = \beta = 90^\circ$, $\gamma = 120^\circ$ $V = 1833.3(1)$ Å^3, $Z = 6$, $\rho_{\text{calcd}} = 1.457$ g cm^{-1}. 632 unique reflections out of 635 with $I > 2\sigma(I)$, 73 parameters, $5.320° < \theta <7\ 5.681°$, $R_1 = 0.0337$, wR_2 = 0.0897, GOF = 1.102. CCDC 2172519.

17: $C_{12}H_{11.79}F_{0.22}$, hexagonal, space group = $R3c$ (No. 161), $a = b = 16.6267(4)$ Å, $c = 7.6522(2)$ Å, $\alpha = \beta = 90^\circ$, $\gamma = 120^\circ$ $V = 1832.0(1)$ Å^3, $Z = 6$, $\rho_{\text{calcd}} = 1.458$ g cm^{-1}. 644 unique reflections out of 645 with $I > 2\sigma(I)$, 73 parameters, $5.321° < \theta < 75.725°$, $R_1 = 0.0366$, wR_2 = 0.1063, GOF = 1.153. CCDC 2172520.

2. Cartesian Coordinates of Optimized Structures

a) Optimized cartesian coordinates of **Sum.**

C	1.40971	0.01336	-0.68398	C	-0.69329	-1.22753	-0.68398
C	0.71643	1.21417	-0.68398	C	0.69329	-1.22753	-0.68398
C	1.21479	2.36589	-0.06664	C	1.44152	-2.23498	-0.06664
C	0	3.30365	0.18499	C	2.86105	-1.65183	0.18499
C	-1.21479	2.36589	-0.06664	C	2.65632	-0.13091	-0.06664
C	-2.51709	2.27967	0.43868	C	3.23279	1.04003	0.43868
C	-3.23279	1.04003	0.43868	C	2.51709	2.27967	0.43868
H	0	3.69921	1.20598	H	3.20361	-1.84961	1.20598
H	0	4.17039	-0.48998	H	3.61167	-2.0852	-0.48998
H	-2.97058	3.12003	0.95865	H	4.18732	1.01258	0.95865
H	-4.18732	1.01258	0.95865				

b) Optimized cartesian coordinates of **F2-Sum.**

C	-0.72807	0.42883	1.40845	H	-0.46523	2.50976	3.61095
C	-0.76868	-0.77111	0.71984	H	0.9536	-0.59868	4.15942
C	-0.17103	-1.92834	1.22121	H	0.90317	-2.71028	2.92724
C	0.05695	-2.86406	0	C	-0.76868	-0.77111	-0.71984
C	-0.17103	-1.92834	-1.22121	C	-0.72807	0.42883	-1.40845
C	0.37951	-1.85974	-2.50067	C	-0.08488	0.55525	-2.64801
C	0.41117	-0.62104	-3.21784	C	0.19893	2.06833	-2.85551
H	0.90317	-2.71028	-2.92724	C	-0.04885	2.65898	-1.43994
H	0.9536	-0.59868	-4.15942	C	0.4875	3.72906	-0.71512
C	-0.70008	1.67128	-0.69379	C	0.4875	3.72906	0.71512
C	-0.70008	1.67128	0.69379	H	1.22475	2.24417	-3.19482
C	-0.04885	2.65898	1.43994	H	-0.46523	2.50976	-3.61095
C	0.19893	2.06833	2.85551	H	1.03298	4.52442	-1.21683
C	-0.08488	0.55525	2.64801	H	1.03298	4.52442	1.21683
C	0.41117	-0.62104	3.21784	F	-0.80176	-3.93402	0
C	0.37951	-1.85974	2.50067	F	1.31881	-3.39181	0
H	1.22475	2.24417	3.19482				

c) Optimized cartesian coordinates of **F6-Sum.**

C	1.4119	0.0169	-0.83506	H	2.89439	3.09049	0.9609
C	0.72058	1.21429	-0.83506	C	-0.72058	1.21429	-0.83506
C	1.21908	2.3464	-0.18111	C	-1.4119	0.0169	-0.83506
C	0	3.27868	0.07002	C	-2.64158	-0.11745	-0.18111
C	-1.21908	2.3464	-0.18111	C	-2.83942	-1.63934	0.07002
C	-2.48545	2.26176	0.39111	C	-1.4225	-2.22895	-0.18111
C	-3.20147	1.02158	0.39111	C	-0.71602	-3.28335	0.39111
H	-2.89439	3.09049	0.9609	C	0.71602	-3.28335	0.39111
H	-4.12364	0.96137	0.9609	H	-1.22925	-4.05186	0.9609
C	-0.69132	-1.23119	-0.83506	H	1.22925	-4.05186	0.9609
C	0.69132	-1.23119	-0.83506	F	0	4.36066	-0.76803
C	1.4225	-2.22895	-0.18111	F	0	3.77388	1.34122
C	2.83942	-1.63934	0.07002	F	-3.26827	-1.88694	1.34122
C	2.64158	-0.11745	-0.18111	F	-3.77644	-2.18033	-0.76803
C	3.20147	1.02158	0.39111	F	3.26827	-1.88694	1.34122
C	2.48545	2.26176	0.39111	F	3.77644	-2.18033	-0.76803
H	4.12364	0.96137	0.9609				

References

1. C. B. Aaker¨y, D. J. Salmon, *CrystEngComm* **2005**, *7*, 439–448.
2. C. B. Aakero¨y, *Acta Crystallogr., Sect. B: Struct. Sci., Cryst. Eng. Mater.* **2015**, *71*, 387–391.
3. S. Aitipamula, P. S. Chow and R. B. H. Tan, *CrystEngComm* **2014**, *16*, 3451–3465.
4. O. Almarsson and M. J. Zaworotko, *Chem. Commun.* **2004**, 1889–1896.
5. J. W. Steed, *Trends Phamacol. Sci.* **2013**, *34*, 185–193.
6. Y.-L. Lei, Y. Jin, D.-Y. Zhou, W. Gu, X.-B. Shi, L.-S. Liao and S.-T. Lee, *Adv. Mater.* **2012**, *24*, 5345–5351.
7. Y. Sun, Y. Lei, H. Dong, Y. Zhen and W. Hu, *J. Am. Chem. Soc.* **2018**, *140*, 6186–6189.
8. J. Zhang, P. Gu, G. Long, R. Ganguly, Y. Li, N. Aratani, H. Yamada and Q. Zhang, *Chem. Sci.* **2016**, *7*, 3851–3856.
9. Y. Qin, J. Zhang, X. Zheng, H. Geng, G. Zhao, W. Xu, W. Hu, Z. Shuai and D. Zhu, *Adv. Mater.* **2014**, *26*, 4093–4099.
10. K. P. Goetz, J. Tsutsumi, S. Pookpanratana, J. Chen, N. S. Corbin, R. K. Behera, V. Coropceanu, C. A. Richter, C. A. Hacker, T. Hasegawa and O. D. Jurchescu, *Adv. Electron. Mater.* **2016**, *2*, 1600203.
11. M. Karimi-Jafari, L. Padrela, G. M. Walker and D. M. Croker, *Cryst. Growth Des.* **2018**, *18*, 6370–6387.
12. A. Friedrich, I. E. Collings, K. F. Dziubek, S. Fanetti, K. Radacki, J. Ruiz-Fuertes, J. Pellicer-Porres, M. Hanfland, D. Sieh, R. Bini, S. J. Clark and T. B. Marder, *J. Am. Chem. Soc*. **2020**, *142*, 18907–18923.
13. C. R. Patrick and G. S. Prosser, *Nature* **1960**, *187*, 1021.
14. K. Reichenba¨cher, H. I. Su¨ss and J. Hulliger, *Chem. Soc. Rev.* **2005**, *34*, 22–30.
15. M. Li, J. Wu, K. Sambe, Y. Yakiyama, T. Akutagawa, T. Kajitani, T. Fukushima, K. Matsuda and H. Sakurai, *Mater. Chem. Front.* **2022**, *6*, 1752.

16. B. M. Schmidt, B. Topolinski, S. Higashibayashi, T. Kojima, M. Kawano, D. Lentz and H. Sakurai, *Chem. Eur. J.* **2013**, *9,* 3282.

17. J. D. Chai and M. Head-Gordon, P*hys. Chem. Chem. Phys*. **2008**, *10*, 6615–6620.

18. T. Lu, Z. Liu and Q. Chen, *Mater. Sci. Eng., B.* **2021**, *273*, 115425.

19. T. Lu and F. Chen, *J. Comput. Chem.* **2012**, *33*, 580−592.

Chapter 4: Biased Bowl-Direction of Monofluorosumanene in the Solid State

Section 1. Introduction

The first stage of crystallization is nucleation, which is heavily influenced by variable aspects, e.g. temperature, solvent, solute concentration, and contamination.[1] These factors have a profound influence on the packing structure of the resulting crystals. The understanding of the characteristics of the structure of crystalline materials is crucial for the reason that these characteristics influence their physical properties. The influence of the solvent in forming the nucleus of a crystal was characterized by proton NMR, IR, DFT calculation, etc. in various aromatic compounds[2-10] and pharmaceuticals[11-14]. However, the general rules governing the processes of nucleation and crystallization[15-17] remain unclear, manipulating the packing structure of the crystal to introduce specific properties remains a challenging problem.[18]

Sumanene (**Sum**), a representative buckybowl, also exhibits dynamic behavior due to the bowl flipping in the solution state (Fig. 36).[19,20] Due to the bowl structure, two geminal protons on the same benzylic carbons of **Sum** are not geometrically equivalent. Sumanene may potentially yield *endo* or *exo* products if mono substitution on one benzyl position is performed, and the *endo* and *exo* products are diastereomers. The ratio of *endo* to *exo* was determined by the stereo-electronic effect, which denotes the steric effect between the substituent and the buckybowl.[21] For instance, hydroxylsumanene only generates the *endo* conformer, but trimethylsilyl sumanene only resulting the *exo* conformer.[21]

The corresponding diastereomers differ in energy, as shown in the preceding example. In the meantime, if the two diastereomers possess close energies, the conversion between them takes place and result in a comparable ratio of *endo* to *exo*. In such a case, the external factors of the environment including temperature, type of solvent, and additives have a chance to affect the conversion of *endo* and *exo*. It is not surprising to monitor a difference *endo* in a single crystal, the effect of the intermolecular interaction overrides the effect of the solvent/molecular interaction.

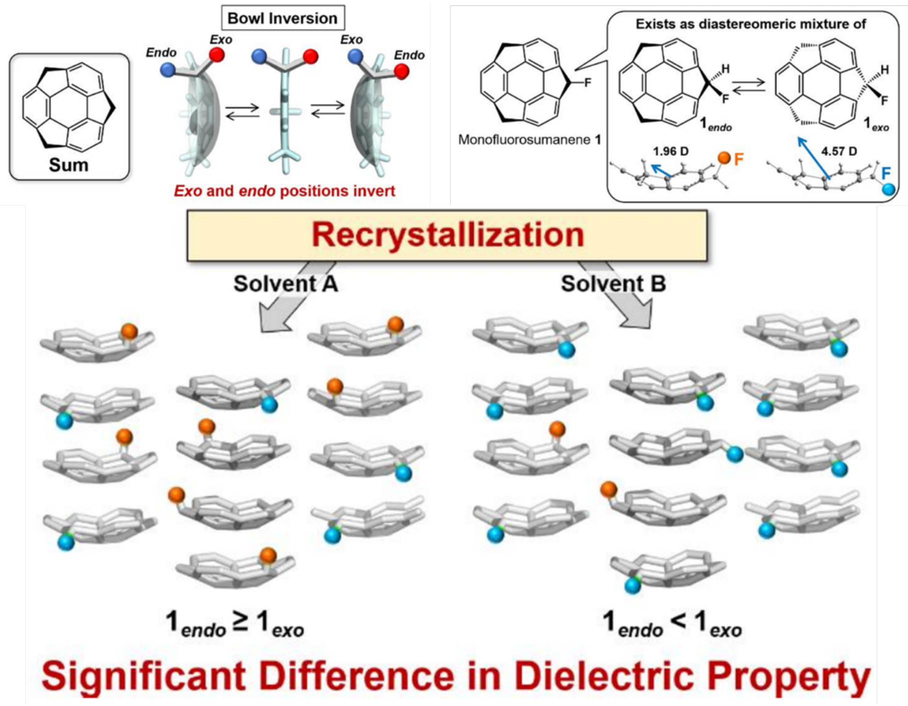

Fig. 36 General concept of this work and bowl-to-bowl inversion of **Sum**.

Table 12 DFT calculation results of **Sum**, $\mathbf{1}_{endo}$, and $\mathbf{1}_{exo}$ under B3LYP/6-31G(d,p) level of theory. The experimental results are in parentheses.

Compound	**Sum**[32]	$\mathbf{1}_{endo}$	$\mathbf{1}_{exo}$
Bowl depth (Å)	1.12(1.11)	1.16	1.14
POAV angle (Å)	8.7(8.9)	8.94	8.81
Dipole moment (D)	(1.94)	1.60	3.68

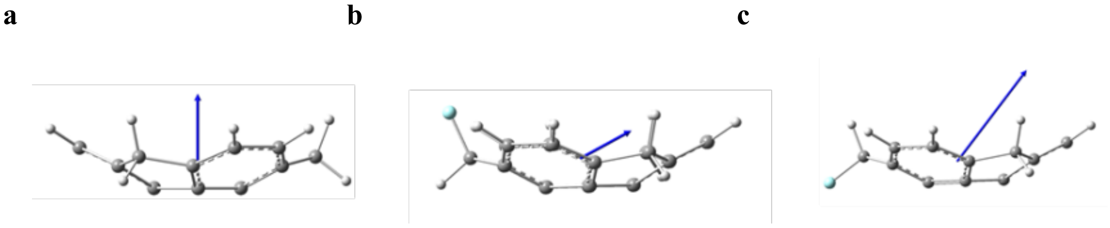

Fig. 37 Calculated dipole moment direction of a) **Sum**, b) ***endo*-F-Sum**, c) ***exo*-F-Sum** under B3LYP, 6-31G(d, p) level of theory. Gray: C, pale-blue: F. White: hydrogen atoms.

The study of fluorosumanenes[22-28] from both structural and application perspectives has been the focus of the author. The fact that these compounds produce the isostructural packing structure in single crystals with pristine sumanene.[29,30] The case of **F2-Sum** is intriguing. The structure of **F2-Sum** actuates a response of anisotropic dielectricity because of its dipole brought by the introduction of a fluorine atom.[23] This property has been used to control dielectric properties by altering the ratio of sumanene to **F2-Sum**[24]. In this unique circumstance, to expand the fluorosumanene chemistry, monofluorosumanene (**F-Sum**) was developed. In this study, **F-Sum** occurs in both solution and solid stages which are composed of two diastereomers: **F-Sum**$_{endo}$ and **F-Sum**$_{exo}$. **F-Sum**$_{endo}$ and **F-Sum**$_{exo}$ had distinct electronic structures and the dipole moments are various (**F-Sum**$_{endo}$: 1.96 D; **F-Sum**$_{exo}$: 4.57 D, Fig. 37, Table 12). It is important to note that **F-Sum** provided the iso-structural packing in a single crystal of **Sum** and its *endo*-to-*exo* ratio significantly varied with crystallization solvent from 60: 40 to 17: 83. These two crystals formed with various *endo*:*exo* ratios which exhibited noteworthy vary in the dielectricity. The mechanism was also investigated by MD and DFT calculation. It was found that the solvation and intermolecular interaction had a significant impact on the final *endo*-to-*exo* proportion in the crystals.

Section 2. Synthesis of 1-fluorosumanene

In the beginning, route 3 was attempted to synthesize **F-sum** in Scheme 4. This route uses the direct fluorination of hydroxylsumanene by diethylaminosulfur trifluoride (DAST) to generate **F-Sum**. However, after the purification by silica gel chromatography, no desired product is obtained. Then the synthesis route was changed to route 1. **1-1** was obtained by nucleophilic addition by thiophenol following a reduction by Triethylsilane. However, in the next step for oxidative fluorination, only an unknown product with large polarity is generated. After surveying the literature, route 2 was figured out, which uses **F2-Sum** as starting material, after partial reductive defluorination, **F-Sum** should be generated. However, this reduction is very difficult to control, only fully reductive defluorinated product- sumanene is obtained. Finally, route 3 was tried again, this time GPC(gel permeation chromatography) was used to separate the product, in a reasonable yield, 1-fluorosumanene (**F-Sum**) was obtained. The reason **F-Sum** was not obtained at the beginning by the purification via silica gel chromatography is that the **F-Sum** can hydrolyze into hydroxylsumanene during the purification procedure, for the fluorine atom was activated by silica gel and the water from the eluent attacked the carbon connecting with fluorine atom to generate hydroxylsumanene.

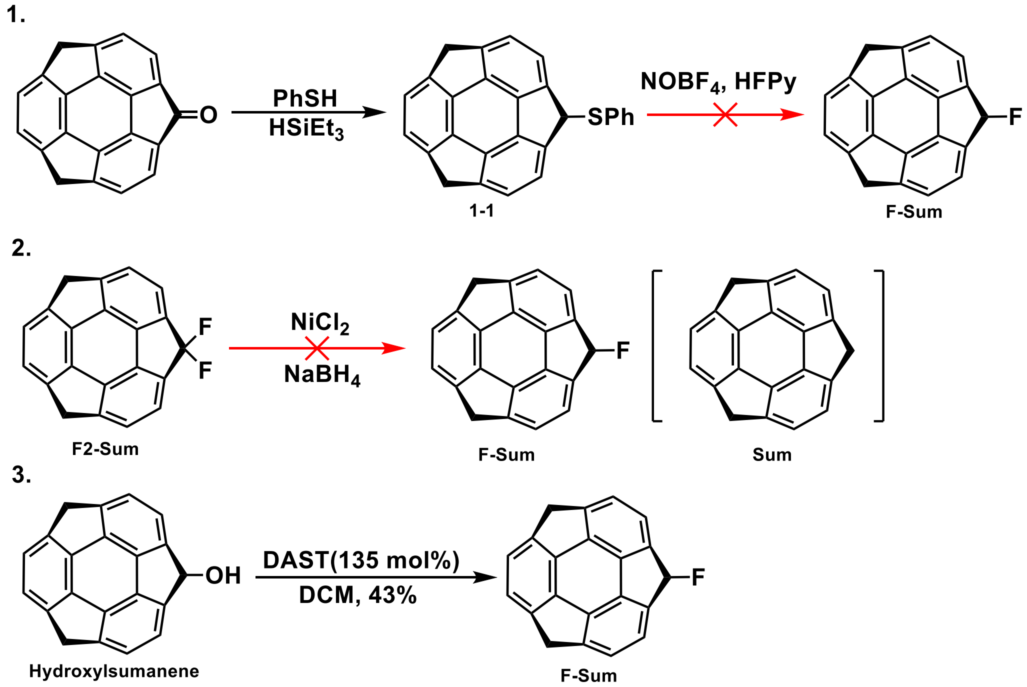

Scheme 4. Synthesis of **F-Sum**.

Section 3. UV-vis absorption spectroscopy, cyclic voltammetry

The effect of the presence of fluorine atom was detected by UV and cyclic voltammetry (CV) experiment. The UV-vis spectra of **F-Sum** displayed an absorption at 276 nm, and a broad peak at 352 nm, which was attributable to the HOMO–LUMO conversion (Fig. 38). Compared with **Sum**, the voltammogram of **F-Sum** displayed a positive shift of the reduction peak, when the acetonitrile was used as the solvent and tetrabutylammonium perchlorate was used as a supporting electrolyte (E_{pred} = −1.81 V (vs Fc^0/Fc^+), Fig. 39). This result indicated that the electron-accepting ability of **F-Sum** is stronger than **Sum** (−2.49 V) due to the presence of an electron negative fluorine atom.[31]

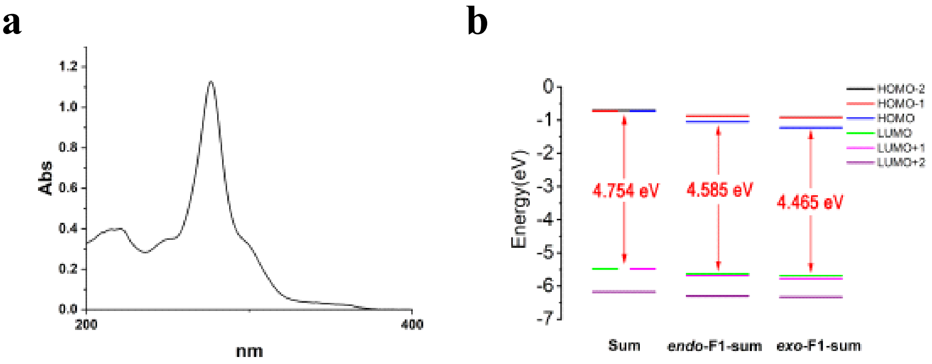

Fig. 38 a) UV-vis spectroscopic of **F-Sum**, 1.0 × 10^{-5} M in DCM. b) DFT calculation result of the energy diagram of **Sum**, **F-Sum**$_{endo}$, and **F-Sum**$_{exo}$ under B3LYP/6-31G(d,p) level of theory.

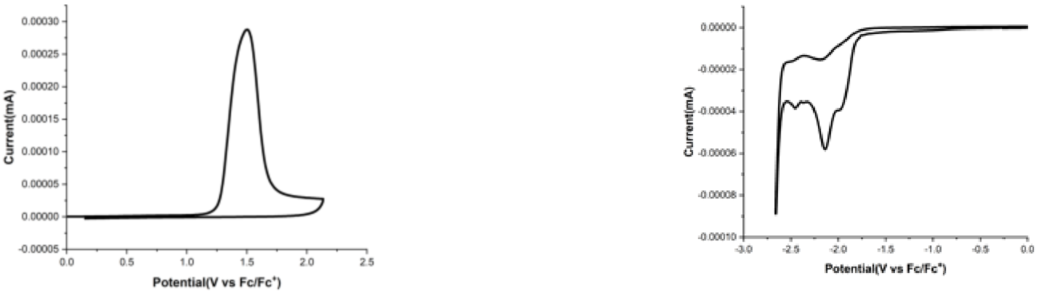

Fig. 39 Cyclic voltammetry diagram of acetonitrile solution of left: oxidation part; right: reduction part of **F-Sum** (2.0 × 10^{-3} M) measured at 294 K in the presence of h tetrabutylammonium perchlorate (0.1 M) supporting electrolyte. Scan rate: 0.1 V s^{-1}. The ferrocene/ferrocenium couple (Fc^0/Fc^+) was used as a reference.

Both theoretical calculations and ^{1}H NMR helped to clarify the thermodynamic stability of **F-Sum**$_{endo}$ and **F-Sum**$_{exo}$. The DFT calculation was performed at B3LYP/6-311+g(d). The result displayed that the bowl inversion energy of **F-Sum**$_{endo}$ to **F-Sum**$_{exo}$ is 19.6 kcal/mol (**F-Sum**$_{exo}$ to **F-Sum**$_{endo}$ is 18.3 kcal/mol, Fig. 40). Which suggested that the stability of **F-Sum**$_{endo}$ is better than **F-Sum**$_{exo}$. The ^{1}H NMR measurements in a variety of solvents at varying temperatures were consistent with these calculation results (Table 13). The signal of the proton on the same benzyl carbon connecting the fluorine atom of **F-Sum**$_{endo}$ is dominant, this observation strongly suggested that the system's major component is **F-Sum**$_{endo}$ but not **F-Sum**$_{exo}$. And the equilibrium of **F-Sum**$_{endo}$ to **F-Sum**$_{exo}$ can be inverted, which was demonstrated by the Van't Hoff plot built by the ratio of *endo* to *exo* versus temperatures (Fig. 41).

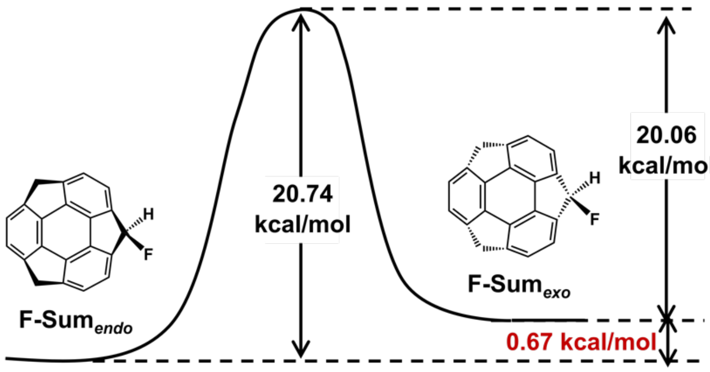

Fig. 40 DFT calculation result of the difference of structure and energy between **F-Sum**$_{endo}$ and **F-Sum**$_{exo}$ at B3LYP/6-311+G(d,p) level of theory.

Table 13 Proton NMR result of the *endo*:*exo* ratio of **1** in different solvents at various temperatures. The concentration of all the samples was 1.5 mg/mL. The figure below denotes the difference in molecular congestion based on the solvent size.

Entry	**Temperature(K)**	**Solvent (*endo*-F-Sum : *exo*-F-Sum)**			
		Acetone-d_6	$CDCl_3$	DMSO-d_6	Toluene-d_9
1	373	-	-	55:45	70:30
2	348	-	-	57:43	72:28
3	323	-	-	58:42	73:27
4	298	64:36	72:28	61:39	75:25
5	273	70:30	74:26	-	-
6	243	78:22	76:24	-	-
7	193	90:10	80:20	-	-

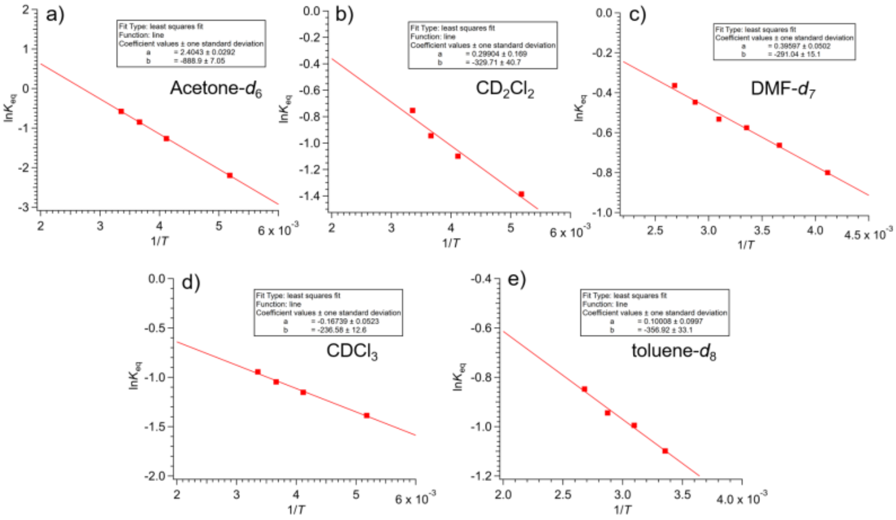

Fig. 41 van't Hoff plots of **F-Sum** in a) Deuterated acetone, b) Deuterated dichloromethane, c) Deuterated DMF, d) Deuterated chloroform, e) Deuterated toluene (400 MHz, 5 mM solution).

The enthalpy and entropy were proved to be related to compensatory correlation by the

$\Delta_r H$ and $\Delta_r S$[32,33] (Fig. 42), pointing to a common inversion mechanism in all four solvents. The bowl inversion process was hypothesized to be driven primarily by the positive entropy change brought about by switching from a congested surrounding of **F-Sum**$_{endo}$ to a relaxed environment of **F-Sum**$_{exo}$. The largest $\Delta_r S$ was gotten with acetone, demonstrating a substantial atomic blockage change engaged with the bowl reversal process around the fluorine molecule. Acetone's smaller molecular size relative to other solvents results in similar molecular congestions around **F-Sum**$_{endo}$ and **F-Sum**$_{exo}$, leading to lower $\Delta_r S$ values.

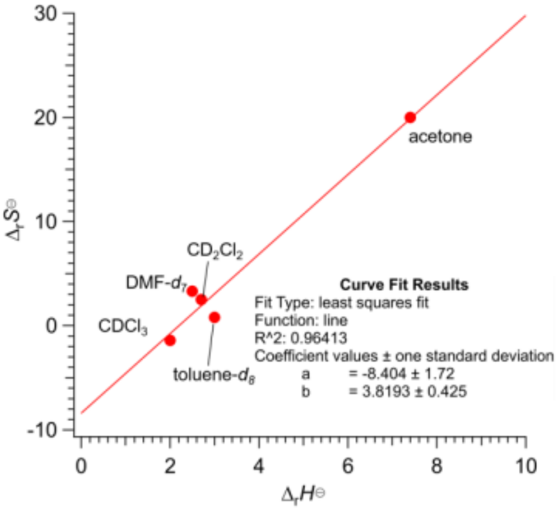

Fig. 42 Plot of the enthalpy vs entropy for bowl-to-bowl inversion of **F-Sum** in deuterated acetone, deuterated chloroform, deuterated dimethyl sulfoxide, and deuterated toluene.

Section 4. Crystallization and Single crystal x-ray crystallography

Previous investigations have revealed that **F-Sum**$_{endo}$ is the major conformer in the solutions. Despite this, **F-Sum**$_{endo}$ and **F-Sum**$_{exo}$ possess close energy levels (<1 kcal/mol). When it is disturbed by intramolecular interactions in the solid state, the *endo* is expected to be quickly converted into *exo*. Next, the crystallization parameters were explored, e.g. type of solvent and temperature, which influence the *endo* to *exo* proportion in solid form. An approach was used to create single crystals with three different solvents, which are DCM, acetone, and DMF. The crystallization proceeded at a temperature ranging from 193 K to 323 K. To make single crystals, a slow evaporation approach was adopted. All of the experiments yielded high-quality crystals. The single crystals possessing the iso-structure of Sumanene, and the reported fluorosumanenes,[27] all space group of them are R*3*c.

Table 14 Crystallization of **F-Sum**, the crystallization procedures are as follows: 0.2mg **F-Sum** in DCM(33 mg/mL), slow diffused with hexane(1 mL) or slow evaporated at specified temperature for 1 week in dark to give the crystals.[a] direct evaporation; [b] slow diffusion.

Solvent	Temp.(K)	F-Sum$_{endo}$: F-Sum$_{exo}$ (x-ray)	Bowl depth (Å)	Bowl to bowl Distance (Å)
DCM[a]	298	44:56	1.142	3.89
	243	60:40	1.143	3.90
	193	45:55	1.142	3.89
	323	31:69	1.140	3.90
Acetone[b]	298	20:80	1.138	3.89
	243	30:70	1.138	3.89
	193	36:64	1.141	3.89
DMF[a]	323	20:80	1.139	3.89
	298	17:83	1.136	3.89
	243	24:72	1.138	3.89

Characterization of the crystal structure revealed that in every single crystal generated from different solvents, the *endo*-to-*exo* ratio is different (Table 14). All entries produced the crystal composed of majorly **F-Sum**$_{exo}$, the percentage is larger than 60%, this result was entirely opposite from the case in the solution state, particularly when acetone was utilized as the solvent in the crystallization. Here is an example, the structure of **F-Sum** was analyzed by single crystal x-ray diffraction under the temperature of 100 K, while a single crystal of **F-Sum** was obtained by slow evaporation of the dichloromethane solvent at 25°C.

F-Sum and **Sum** have the same packing structure, while **F-Sum** possesses a lower molecular symmetry than C3-symmetric **Sum**, this result benefits from the smaller fluorine atom. Due to the presence of the triple axis at the center of the sumanene unit in the crystal structure, the occupancy factor of each of the two *endo* and *exo* fluorinated parts were 0.154(3) and 0.179(3), respectively (Fig. 43), namely, this is a co-crystal composed of 46mol% **F-Sum**$_{endo}$ and 54 mol% **F-Sum**$_{exo}$. Fig. 43 indicates that this cocrystal is the

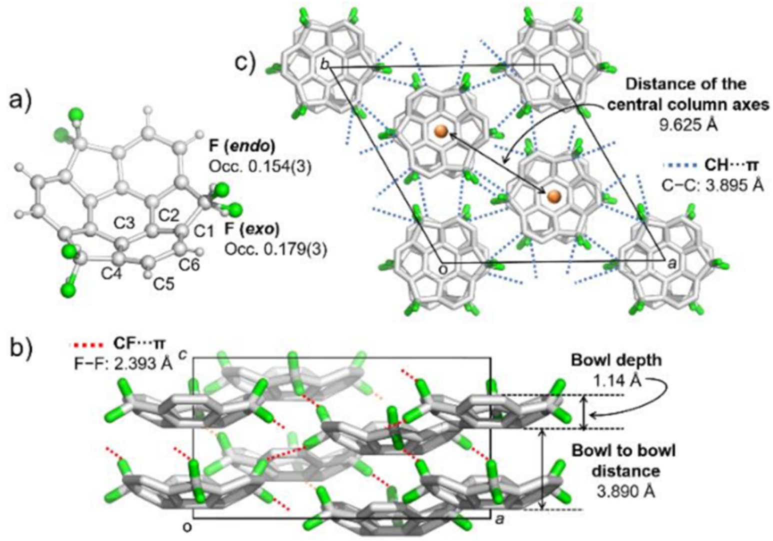

Fig. 43 X-ray single crystal result of **F-Sum**. This crystal was obtained by slow evaporation of **F-Sum** in DCM at 193 K.

iso-structure with suamanene. Meanwhile, this cocrystal possesses a bowl structure with an average bowl depth (from **F-Sum**$_{endo}$ and **F-Sum**$_{exo}$) of 1.14 Å(**Sum**: 1.11 Å) and a POAV angle of 8.9°. The bowl-to-bowl distance in **F-Sum** is 3.89 Å (Fig. 43b), this value is almost the same as the case of **Sum** (3.86 Å), probably due to the smaller fluorine atom. All the columns were linked by CH···π (3.895 Å) and F···F interactions (2.393 Å)(Fig. 43c). It is worth noting that the column-to-column distance was 9.623 Å (Fig. 43c), whereas the case of **Sum** is 9.570 Å. The structural characteristics were not significantly affected by the difference in the *exo*:*endo* ratio, showing that the structural difference between **F-Sum**$_{endo}$ and **F-Sum**$_{exo}$ decreases in the stacking column. However, it is plausible to surmise that in order to generate single crystals with a wide range of *exo*:*endo* ratios, small structural and electric properties of **F-Sum**$_{endo}$ and **F-Sum**$_{exo}$ were amplified during the crystallization process by intermolecular interactions and solvent, which confirmed that **F-Sum**$_{endo}$ possesses high similarity structure parameters including bowl depth with **F-Sum**$_{exo}$. Due to the interaction between the solvent and **F-Sum**$_{endo}$ being different from the interaction between the solvent and **F-Sum**$_{exo}$, the crystals in various *endo*-to-*exo* proportions can be generated by altering the type of solvent for crystallization.

Section 5. Dielectric experiments

Because of **F-Sum**'s changeable *exo*:*endo* ratio in the single crystal state and the stark contrast in dipole moments that exist between **F-Sum**$_{endo}$ and **F-Sum**$_{exo}$, **F-Sum** was attempted to prepare dielectric material that possesses tunable dielectricity. The crystalline sample was obtained by recrystallization from dimethylformamide ($\mathbf{S_{DMF}}$, **F-Sum**$_{endo}$: **F-Sum**$_{exo}$ = 27:73) or dichloromethane ($\mathbf{S_{CH2Cl2}}$, **F-Sum**$_{endo}$: **F-Sum**$_{exo}$=43:57). Under N_2 environment, the dielectric experiments proceeded on both samples at multiple frequencies, ranging in temperature from 300 K to 420 K (Fig. 41). The dielectric property varied significantly according to the *endo*-to-exo proportion. From the sample of S_{DMF}, at 1MHz, approximately 360 K, there was a Debye-type dielectric relaxation, and the real (ε_1) and imaginary (ε_2) parts of the dielectric constant were elevated. (Fig. 44a and 44b). This phenomenon was somewhat comparable to the previously described **F2-Sum**,[23] showing that the primary source of the dielectric response was the planar molecular motion of **F-Sum**$_{exo}$. The Arrhenius plot of it revealed a linear connection (Fig. 45), and the activation energy E_a = 70 kJ/mol to trigger the molecular motion of S_{DMF}. This value is found to be comparable to other known π-planar organic dielectric materials and the case of **F2-Sum**.[30, 31] As a simple organic molecule, on the other hand, S_{CH2Cl2} had noticeably high dielectric constants even after the potentially contained solvents were carefully dried up. The dielectric constant continued to drop sharply after the first heating (Fig. 44c-44f). It was anticipated thatthe structure was loose when the temperature was high and resulting in a structure with better stability, then the thermally induced mobility of **F-Sum**$_{exo}$ would be strictly forbidden.

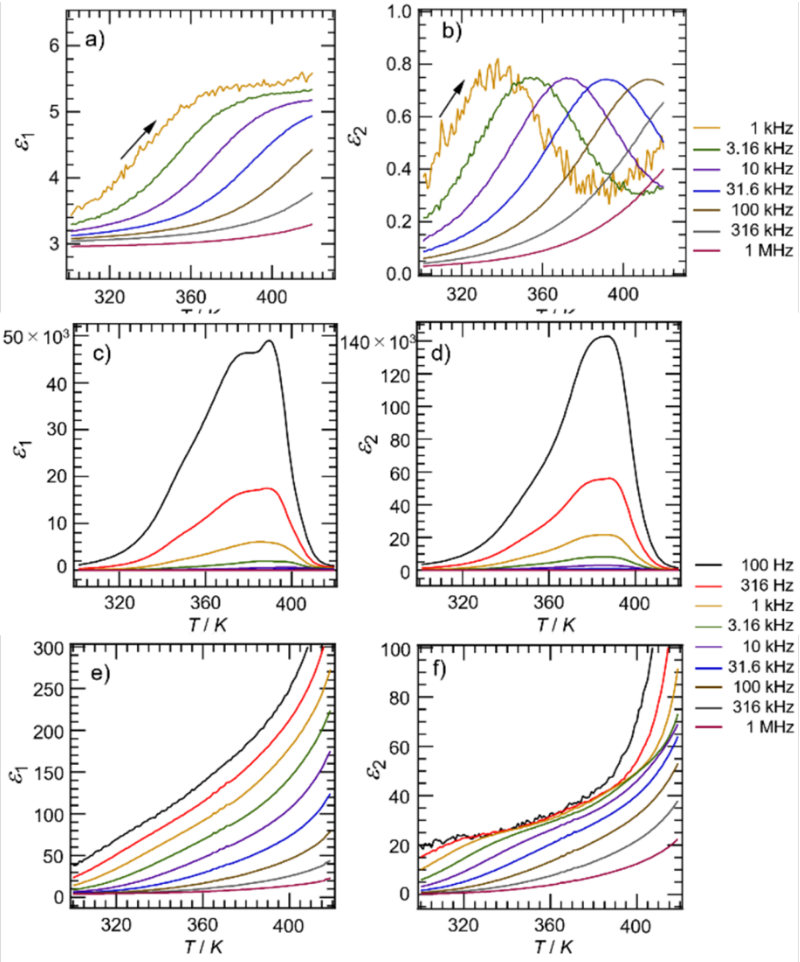

Fig. 44 a), b) the real part (ε_1) and the imaginary part (ε_2) of the dielectric constant of $\mathbf{S_{DMF}}$; c), d) the real part (ε_1) and the imaginary part (ε_2) of the dielectric constant of $\mathbf{S_{CH2Cl2}}$. e) and f) denotes the 2nd sweep.

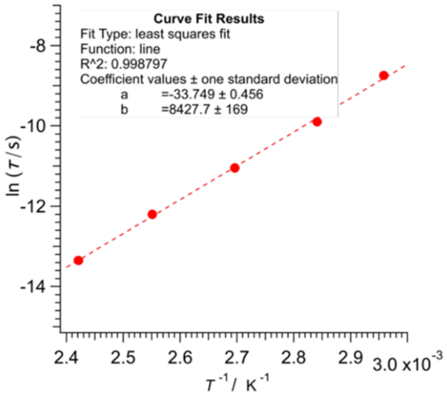

Fig. 45 Arrhenius plot of $\mathbf{S_{DMF}}$ in powder crystalline pellet.

Section 6. DFT calculation and MD simulation

Regarding using the functional molecules, the fact that a simple alteration in the crystallization solvent brings out a notable alteration of characters is a major advantage. To evaluate the interaction strength between the solvent and *endo* or *exo* form, and to get information on how the interaction strength determines the final result, DFT calculation was performed. To investigate the reason how the intermolecular interactions affect the ultimate **F-Sum**$_{exo}$: **F-Sum**$_{endo}$ ratio in the single crystal in the crystallization process of **F-Sum**, **F-Sum**$_{endo}$ and **F-Sum**$_{exo}$ were made up of a basic dimer model that can explore the stacking sequence and conformer that is most stable. The interaction energies of the dimer of **F-Sum** were calculated.

Due to the intra-columnar interaction being the major factor in maintaining the packing structure of sumanene rather than inter-columnar interaction,[24] the dimer model was constructed in a columnar model under ωb97XD/6-311+G(d,p) level of theory. The distance of every unit was fixed at 3.9Å and the rotation angle of the dimer was fixed at 60° or 180° (Fig. 46). Every potential stacking order of the dimer was considered. The calculated result indicated the dimer containing **F-Sum**$_{endo}$ at the bottom was less stable. These findings suggested that when the fluorine atom of **F-Sum**$_{endo}$ was connected to the bowl vertically, resulting in considerable steric hindrance. On the contrary, the C-F bond in **1**$_{exo}$ adopted a direction near the horizontal direction to avoid steric effects during the process that forming the packing structure. These findings clarified why, **F-Sum**$_{exo}$ is easier to extend the packing column by the convex side. In fact, the increase in the **F-Sum**$_{exo}$ percentage in every crystal when compared to the solvated case indicated that the explanation provided above can account for part of the phenomenon. However, the type of solvent in the crystallization ruled out the final *endo*-to-*exo* ratio in the resulting crystal, which either aided or hindered the introduction of **1**$_{exo}$ into the final crystal structure.

Using three different solvent systems: acetone, DCM, and DMF in the molecular dynamics (MD) simulation, the result showed how the solvent and the *endo-to-exo* proportion relate to one another throughout the crystallization process. GROMACS 2020.6 was used to conduct all of the MD simulations.[34] At first, the solvent effect on the aggregation of **F-Sum**$_{endo}$ or **F-Sum**$_{exo}$ was investigated. The following systems were built to simulate it, 100% **F-Sum**$_{endo}$, 100% **F-Sum**$_{exo}$, and a mixture of 50% percent of each. And defining that there is no bowl inversion during this process. At each run, the concentration of **F-Sum** was fixed, and the aggregate population was investigated. In addition, the aggregate was defined as follows: the distance of two molecules smaller than 8Å are counted as aggregate. For every conformer and for the 50:50 mixture, the monomer population is greater following this sequence: dimethylformamide > dichloromethane > acetone (Fig. 47). On the contrary, the aggregation propensity is decreased in DMF and it's stronger with acetone > DCM > DMF. Additionally, Fig. 47 also shows that there are fewer **F-Sum**$_{endo}$ to form aggregate, suggesting that **1**$_{exo}$ is easier to form aggregate. Table 15 lists the **F-Sum**$_{exo}$ and **F-Sum**$_{endo}$ isomers' respective preferences in the state of monomeric and

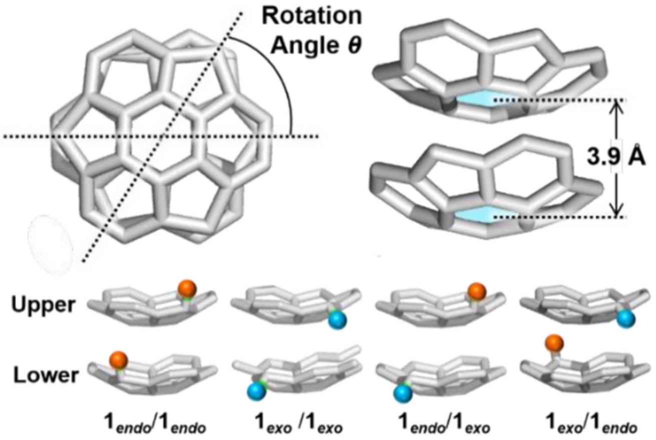

Upper/Lower	Interaction Energy(kcal/mol)[a]	
	60°	180°
1$_{endo}$ /**1**$_{endo}$	-18.81	-18.35
1$_{exo}$ /**1**$_{exo}$	-21.03	-21.34
1$_{endo}$ /**1**$_{exo}$	-21.05	-21.10
1$_{exo}$ /**1**$_{endo}$	-18.94	-18.92

[a](calculated under ωb97xd, 6-311+g(d, p) level of theory).

Fig. 46 The definition of the dimer model and the DFT calculation result of the intermolecular energies based on different dimer models.

aggregates. For instance, the population of **F-Sum**$_{endo}$ and **F-Sum**$_{exo}$ in monomeric state is 57:43 in acetone, suggesting that the *endo* is preferred when **1** is a monomeric form.

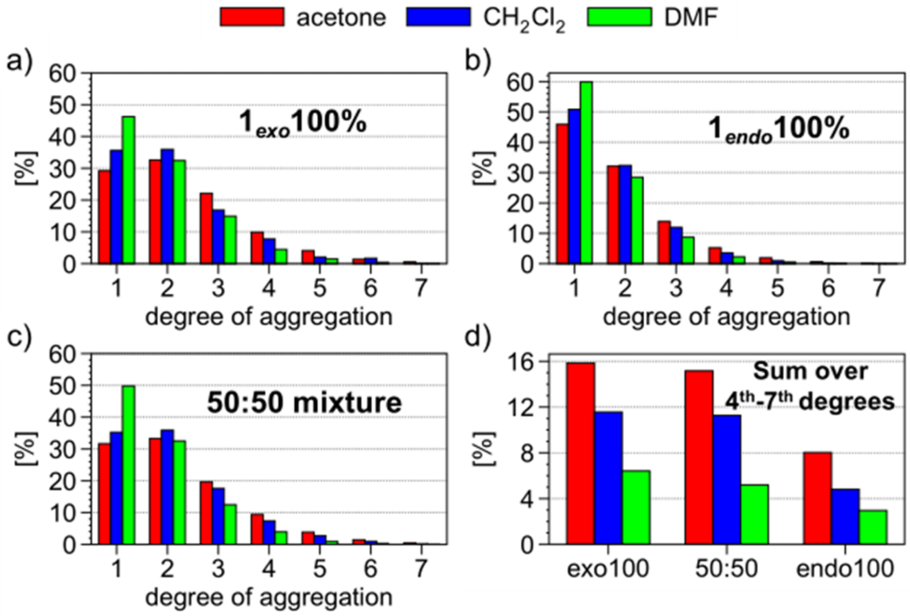

Fig. 47 Degree of the aggregation of a) 100% **F-Sum**$_{exo}$; b) **F-Sum**$_{endo}$, and c) 50:50 mixture of **F-Sum**$_{endo}$ to **F-Sum**$_{exo}$ in acetone, CH_2Cl_2, and DMF. d) The sum over the degrees of aggregation of 4 to 7 to explain the dependence on conformational states and solvents in more detail.

Table 15 The average number of **F-Sum**$_{exo}$ in every degree of aggregation in acetone, DCM and DMF. The concentration of **F-Sum** was 0.5 mol/L and *exo*:*endo* ratio was 50:50.

	Degree of aggregation						
Solvent	**1**	**2**	**3**	**4**	**5**	**6**	**7**
Acetone	0.43	1.0	1.6	2.2	2.8	3.4	3.8
DCM	0.44	1.0	1.7	2.3	3.0	3.5	3.9
DMF	0.48	1.0	1.6	2.2	2.6	2.9	3.3

This result is consistent with the experimental result in Table 10. Table 15 displays that over 50% of **F-Sum** are in the *exo* form at the moment the aggregation degree is over 2. Compared to the case of acetone, the tendency in DCM was similar, while **F-Sum**$_{exo}$ population growth was not as sharp in dimethylformamide as what was seen in acetone and CH_2Cl_2, and even at the 7th degree of aggregation, the average value was 3.3.

Next, the way that **F-Sum** stacking in every aggregate was examined, with an emphasis on the adjacent pairings which the distance of two adjacent molecules is smaller than 8 Å. The simulation result in acetone and DCM showed that the **F-Sum**$_{exo}$/**F-Sum**$_{exo}$ combination took center stage as the degree of aggregation rose, whilst those who had the *endo* conformer were on the reduce (Fig. 48). This outcome is consistent with the DFT calculation for **F-Sum**$_{exo}$, which benefits more in increasing the length of the packing column compare with **F-Sum**$_{endo}$. The same pattern was noted in the DMF case. According to the debate above, **F-Sum**$_{exo}$ was more straightforward incorporated thoroughly in the elongation of the aggregates than **F-Sum**$_{endo}$, and the aggregation is anyhow prohibited in dimethylformamide. However, to be noted, the *endo*-to-*exo* ratio is 50 to 50 in the simulation but not in the real experiment. As Table 10 illustrates, this has an impact on the degree of *exo* propensity at recrystallization process, more information was discussed later.

The energy difference in vacuum was calculated in Fig. 40, and the *endo*:*exo* ratio is altered as a result of the solvation effect, which is estimated by $\Delta\mu$ (solvation free energy) of **F-Sum** in monomeric state. It is displayed in Fig. 49. It is clear that the *exo* form partially cancels the preference of *endo* form in Fig. 40, and possesses higher interaction energy while contacting with every solvent than the *endo* form does. The degree of partial cancellation is stronger following this sequence: DMF > acetone > DCM, these results implied that the population of the *exo* is bigger following this sequence at the beginning of the recrystallization. As Fig. 45 illustrates, the propensity of the *exo* inclusion is more obvious in acetone and dichloromethane. Combining these two types of effects, the population of *exo* form is larger when DMF was used as the crystallization solvent (Table 10), for its stability is better at the start of the crystallization. In the case of acetone, it’s because of the better efficiency of the *exo* inclusion to results high *exo* population. Actually, Table 15 and Fig. 48 and 49 reveal that when the *exo* form is more highly solvated, it is less favorably integrated into aggregates. At the solvated state, the energy preference for *exo* pairs in aggregate competes with the energy preference of the *exo* monomer, and the energy preference of the *exo* monomer determines the propensity of *exo* during the process of crystallization. As a result, the ratio of *exo* gets higher in the crystal at the moment the interaction between *exo* and solvent is strengthened.

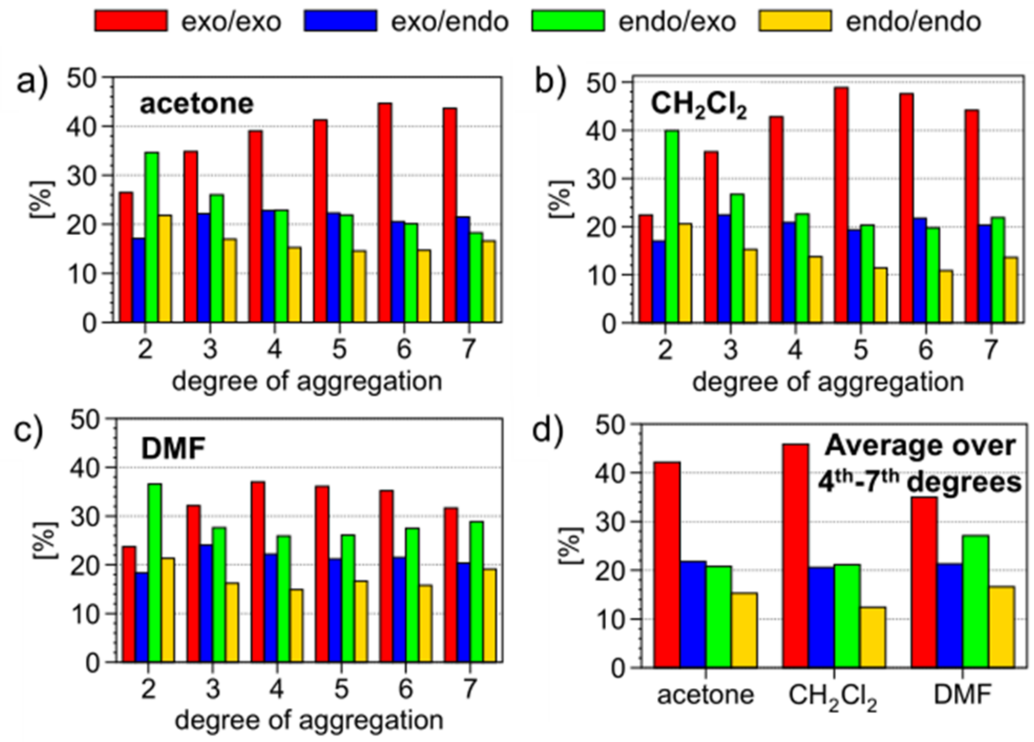

Fig. 48 The population analysis data of the dimers of *exo*/*exo*, *exo*/*endo*, *endo*/*exo*, and *endo*/*endo* of **F-Sum** in different aggregates in a) acetone, b) DCM and c) DMF. d)The averaged values over the degrees of aggregation of 4 to 7 to explain the dependence on the solvents clearerly. The definition of the dimers follows Fig. 46.

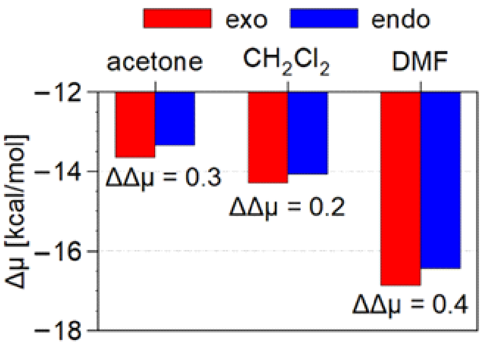

Fig. 49 Solvation free energy Δμ of *endo* and *exo* of **F-Sum** in acetone, DCM, and DMF. ΔΔμ = Δμ($\mathbf{1}_{endo}$)–Δμ($\mathbf{1}_{exo}$) is in units of kcal/mol for each solvent.

Section 7. Summary

Through bowl inversion, monofluorosumanene (**F-Sum**) occurs as diastereomers composed of **F-Sum**$_{exo}$ and **F-Sum**$_{endo}$, which was successfully synthesized. The theoretical and experimental findings revealed the energy link between **F-Sum**$_{endo}$, **F-Sum**$_{exo}$ and solvent, allowing the author to generate the single crystal of **F-Sum** with a specific *exo*-to-*endo* ratio by selecting the specified crystallization solvent. Throughout the course of this research, it was discovered that while the solvation effect benefits the stability of **F-Sum**$_{exo}$, and it was insufficient to overturn **F-Sum**$_{endo}$'s intrinsic stability, which led to a bigger amount of **F-Sum**$_{endo}$ under solvated conditions. Nonetheless, the inversion of the *exo*:*endo* proportion in solid form was made easier by the advantage of the less steric structure of **F-Sum**$_{exo}$ for aggregation. Understanding the underlying mechanisms was greatly aided by the DFT and MD simulations, which highlighted the crucial importance of two factors: the inclusion efficiency of **F-Sum**$_{exo}$ and the solvation stabilization effect. A regulated *exo*:*endo* ratio of **F-Sum** made it possible to create special materials with completely distinct dielectric responses. Using only a different crystallization solvent, **F-Sum** can generate two types of crystals that exhibit a tremendous varies in the dielectric response, one of them contains Debye-type relaxation and the rest one possesses a remarkably high dielectric constant. This noteworthy accomplishment brings the bowl reversing phenomenon in curved-π moieties closer to new applications and emphasizes the extraordinary underlying of fluorosumanenes as other energy materials.

Experimental section

1. Characterization

1-fluoro-4,7-dihydro-1H-tricyclopenta[def,jkl,pqr]triphenylene (F-Sum)

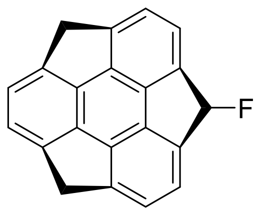

To a solution of hydroxylsumanene[1] (47 mg, 0.168 mmol, 100 mol%) in dry DCM (10 mL) in a plastic tube was added DAST (diethylaminosulfur trifluoride, 0.03 mL, 0.227 mmol, 135 mol %) under nitrogen gas at 0 °C. Then the reaction was stirred at 25°C for 20 min. Quenched by methanol (2 mL) at -40 °C and evaporated. The residue was purified by GPC (gel permeation chromatography) by chloroform as the eluent to give the target product **1** as a white solid (20.0 mg, 43%). mp: 230 ºC (dec.); ^{1}H NMR ($CDCl_3$, 400 MHz, 25 ºC): δ (ppm) 7.53 (d, 0.72H, J = 52 Hz, *endo*-F1-Sum), 7.11-7.20 (m, 6H), 5.71 (d, J = 52 Hz, *exo*-F1-Sum 0.28H), 4.72 (d, J = 16 Hz, *exo*-F1-Sum, 0.56H), 4.70 (d, J = 20 Hz, *endo*-F1-Sum, 1.44H), 3.45 (d, J = 20 Hz, 2H); ^{13}C NMR ($CDCl_3$, 100 MHz): δ (ppm) 153.02 (d, J = 3 Hz), 151.99, 150.33 (d, d, J = 18 Hz), 149.88 (d, J = 23 Hz), 149.22, 148.90, 148.59, 148.51, 148.25, 147.61 (d, J = 24 Hz), 143.12 (d, J = 19 Hz), 125.87 (d, J = 3 Hz), 124.05, 124.00, 123.70, 121.74 (d, J = 2 Hz), 100.69 (d, J = 203 Hz, *endo*-F1-Sum), 92.35(d, J = 183 Hz, *exo*-F1-Sum), 41.96 (*endo*-F1-Sum), 41.73 (*exo*-F1-Sum)); ^{19}F-NMR ($(CD_3)_2CO$, 376 MHz): δ (ppm) -165.71 (d, J = 60 Hz, *exo*-F1-Sum,), -196.10 (d, J = 60 Hz, *endo*-F1-Sum); IR (KBr): 3051.80, 2956.34, 2926.45, 2881.13, 2850.27, 2778.92, 2357.55, 2338.27, 1867.72, 1735.62, 1716.34, 1455.03, 1394.28, 1306.54, 1261.22, 1177.33, 1128.15, 1086.69, 1055.84, 1025.94, 984.48, 945.91, 923.74, 908.31, 809.96, 786.82, 745.35, 726.07, 684.61, 600.72, 566.97, 472.47, 419.44; HRMS (EI) *m/z*: Calcd. for $C_{21}H_{10}F_2$ $[M]^+$ 282.0845, found: 282.0844. Elemental Analysis: Calcd. for $C_{21}H_{11}F$: C, 89.34; H, 3.93; Found: C, 88.71; H, 4.21.

2. X-ray Crystal Structure Analysis

All the diffraction data for the crystals of **F-Sum** (**a-k**) except **l** were recorded on a XtaLAB Synergy with a Cu-target (λ = 1.54184 Å) equipped with a Rigaku HyPix-6000HE as the detector at 193 K or 173 K or 123 K in house. The diffraction data for the crystal **l** was recorded on a DICTRIS PILATUS3 X CdTM 1M Detector System (λ = 0.4132 Å) at 100 K at SPring-8 BL02B1 in SPring-8.

The diffraction images were processed by using CrysAlisPro for **a-k** and Bruker APEXIII for **l**. All the structures were solved by direct methods (SHELXT-2015, 2018/2) and refined by full-matrix least squares calculations on F^2 (SHELXL-2018/3) using the Olex2 program package. All the crystals had isostructural packing with $R3c$ space group, indicating 1/3 of the molecular skeleton is crystallographically independent. The independent unit included one benzylic carbon, to which total 0.33 F atom and 1.67 H were hanging. In order to assign the occupancy factors at the disordered moiety, we modeled two sets of free-variable pairs composed of F and H atoms and refined with SUMP command to make the total occupancy factors of F atoms to be 0.33 as well as PART command.

CCDC 2288999-2289010 contain the supplementary crystallographic data. These data can be obtained free of charge via The Cambridge Crystallographic Data Centre (http://www.ccdc.cam.ac.uk/data_request/cif).

Crystal	**a**	**b**	**c**	**d**	**e**	**f**
Solvent	CH_2Cl_2	CH_2Cl_2	CH_2Cl_2	acetone	acetone	acetone
Temperature	298 K (25 °C)	243 K (−30 °C)	193 K (−80 °C)	323 K (50 °C)	298 K (25 °C)	243 K (−30 °C)
Formula	$C_{21}H_{11}F_1$	$C_{21}H_{11}F_1$	$C_{21}H_{11}F_1$	$C_{21}H_{11}F_1$	$C_{21}H_{11}F_1$	$C_{21}H_{11}F_1$
Crystal Size (mm^3)	0.22×0.13×0.10	0.20×0.078×0.078	0.40×0.050×0.050	0.13×0.033×0.01	0.10×0.089×0.046	0.094×0.094×0.047
Crystal System	Trigonal	Trigonal	Trigonal	Trigonal	Trigonal	Trigonal
Space Group	$R3c$	$R3c$	$R3c$	$R3c$	$R3c$	$R3c$
a (Å)	16.6667(3)	16.6618(8)	16.6711(2)	16.6949(4)	16.6907(3)	16.6828(3)
b (Å)	16.6667(3)	16.6618(8)	16.6711(2)	16.6949(4)	16.6907(3)	16.6828(3)
c (Å)	7.7812(2)	7.7939(4)	7.7792(1)	7.7956(3)	7.7766(2)	7.7742(1)
α (°)	90	90	90	90	90	90
β (°)	90	90	90	90	90	90
γ (°)	120	120	120	120	120	120
V (Å^3)	1871.87(8)	1873.8(2)	1872.38(5)	1881.7(1)	1876.16(8)	1873.80(7)
Z	6	6	6	6	6	6
D_{calc} (g cm^{-3})	1.502	1.500	1.502	1.495	1.499	1.501
μ (mm^{-1})	0.765	0.765	0.767	0.763	0.765	0.766
Reflections collected/unique	692/684	757/753	833/827	853/841	844/840	846/846
R_1/wR_2 ($I > 2\sigma(I)$)	0.0294/0.0784	0.0381/0.1012	0.0278/0.0767	0.0308/0.0801	0.0303/0.0807	0.0284/0.0709
GOF on F^2	1.082	1.092	1.050	1.101	1.098	1.100
Occ. of $F_{\mathrm{endo}}/F_{\mathrm{exo}}$	0.150 (4)/0.183(4)	0.196(6)/0.137(6)	0.154(3)/0.179(3)	0.112(4)/0.221(4)	0.083(4)/0.250(4)	0.089(4)/0.244(4)
CCDC No.	2288999	2289001	2289007	2289002	2289000	2289009

Crystal	**g**	**h**	**i**	**j**	**k**	**l**
Solvent	acetone	DMF	DMF	DMF	CH_2Cl_2	DMF
Temperature	193 K (−80 °C)	323 K (50 °C)	298 K (25 °C)	243 K (−30 °C)	298 K (25 °C)	298 K (25 °C)
Formula	$C_{21}H_{11}F_1$	$C_{21}H_{11}F_1$	$C_{21}H_{11}F_1$	$C_{21}H_{11}F_1$	$C_{21}H_{11}F_1$	$C_{21}H_{11}F_1$
Crystal Size (mm^3)	0.20×0.033×0.016	0.36×0.056×0.056	0.36×0.033×0.033	0.24×0.060×0.060	0.12×0.067×0.044	0.12×0.040×0.030
Crystal System	Trigonal	Trigonal	Trigonal	Trigonal	Trigonal	Trigonal
Space Group	$R3c$	$R3c$	$R3c$	$R3c$	$R3c$	$R3c$
a (Å)	16.6808(2)	16.7060(3)	16.6999(3)	16.6786(2)	16.6845(3)	16.673(3)
b (Å)	16.6808(2)	16.7060(3)	16.6999(3)	16.6786(2)	16.6845(3)	16.673(3)
c (Å)	7.7808(1)	7.7806(2)	7.7889(2)	7.7710(1)	7.7481(1)	7.733(2)
α (°)	90	90	90	90	90	90
β (°)	90	90	90	90	90	90
γ (°)	120	120	120	120	120	120
V (Å^3)	1874.94(5)	1880.57(8)	1881.20(8)	1872.09(5)	1867.89(7)	1861.7(7)
Z	6	6	6	6	6	6
D_{calc} (g cm^{-3})	1.500	1.495	1.495	1.502	1.505	1.511
μ (mm^{-1})	0.766	0.763	0.763	0.767	0.768	0.041
Reflections collected/unique	851/851	849/847	849/839	848/845	866/850	948/899
R_1/wR_2 ($I > 2\sigma(I)$)	0.0313/0.0792	0.0329/0.0817	0.0331/0.0813	0.0279/0.0726	0.0305/0.0797	0.0556/0.1345
GOF on F^2	1.069	1.094	1.075	1.056	1.083	1.041
Occ. of $F_{\mathrm{endo}}/F_{\mathrm{exo}}$	0.121(4)/0.211(4)	0.074(4)/0.259(4)	0.058(5)/0.274(5)	0.096(4)/0.237(4)	0.176(3)/0.156(3)	0.090(6)/0.242(6)
CCDC No.	2289008	2289006	2289004	2289010	2289005	2289003

3. Molecular dynamics simulation detail

MD (molecular dynamics) simulations were performed at 300 K using GROMACS 2020-6.[34] The initial configuration for the simulation was constructed by using Packmol and filling the unit cell of MD randomly with solvent molecules and 300 molecules of **1**, where the numbers of acetone, CH_2Cl_2, and DMF molecules were 8170, 9400 and 7780, respectively.[35] The MD cell was then a cube of edge length 100 Å^3, and the periodic boundary condition was employed with minimum image convention. The force field was GAFF (general AMBER force field), and the atomic partial charges were determined with RESP (restrained electrostatic potential).[36,37] The RESP procedure was carried out after DFT calculations at the B3LYP/6-31G(d,p) level with Gaussian16.[38a] After the energy minimization with the steepest descent method for 50000 steps, MD was carried in the *NVT* ensemble over 0.5 ns for the initial equilibration and in *NPT* at 1 bar over 0.5 ns for the following equilibration and over 30 ns for production.

In MD, the electrostatic interaction was handled by the smooth particle-mesh Ewald (PME) method with a real-space cutoff of 12 Å, a spline order of 6, a relative tolerance 10^{-5}, and a reciprocal-space mesh size of 128 along each of the x, y, and z directions.[39] The Lennard-Jones (LJ) interaction was truncated at 12 Å with a switching range of 10-12 Å,[40] and the long-range correction was not incorporated. The Lorentz-Berthelot rule was employed to combine the LJ interaction between unlike pairs of atoms, and the truncation was applied on atom-atom basis both for the real-space part of PME and for LJ. The leap-frog method was adopted to integrate the equation of motion at a time step of 2 fs and an inverse friction time constant of 2 ps.[41,42] The pressure was regulated by the Berendsen and the Parrinello-Rahman barostats with a coupling time of 2 ps in the equilibration and in the production, respectively, where the isothermal compressibility was set to 4.5×10^{-6} bar^{-1} and the isotropic coupling was employed.[43,44] The LINCS algorithm was used to fix the lengths of the bonds with a hydrogen atom.[45]

Below figure illustrates the radial distribution function for the center-of-mass distance between a pair of 1-fluorosumanene molecules in solvent acetone at *endo*:*exo* = 50:50. For Figures 7 and 8 and the related discussion, 1-fluorosumanene molecules were treated as an aggregate when they are connected within distances corresponding to the first-peak region of the center-of-mass radial distribution function.

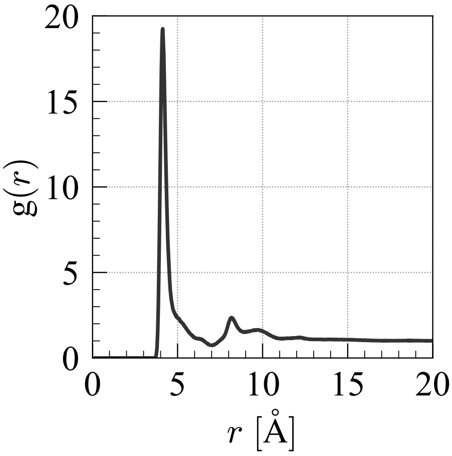

Figure S1. Radial distribution function g(*r*) in the 50:50 mixture system with solvent acetone, where *r* is the center-of-mass distance of **1**s.

In the present work, the solvation free energy of $\mathbf{1}_{endo}$ and $\mathbf{1}_{exo}$ in the bulk solvent was evaluated using the energy-representation method[46,47]. To obtain the solvation free energy with the method of energy representation, MD simulations were performed for three systems of the "solution", "reference solvent", and the isolated solute in vacuum. The unit cell of MD of each system was cubic. The solution system contained a single solute molecule and 1000 solvent molecules. For both systems, the production-run length was for 5 ns and the sampling interval was 0.2 ps. The MD setups for the solution and reference solvent were the same as those for the production runs in the above, except that the reciprocal-space mesh size in PME was 48 along each of the *x*, *y*, and *z* directions. The isolated solute was simulated in vacuum. MD of the single solute was performed for 10 ns at a sampling interval of 0.1 ps. The electrostatic potential was treated as its bare form of 1/*r* without cutoff, and the LJ interaction was handled with the same procedure as that for the solution and reference solvent. The solute molecule was then inserted into the reference-solvent system as a test particle at random position and orientation. The test-particle insertion was done without affecting the configuration of the reference solvent which had been simulated independently from the isolated solute. The number of insertions was 1000 for each reference-solvent configuration sampled, which leads to the generation of 2.5×10^7 solute-solvent configurations in total for the free-energy calculation with the energy-representation method.

4. Calculation details

For the bowl inversion analysis, the ground state structures were obtained by full optimization at the B3LYP/6-311+g(d,p) level of theory using Gaussian16 package.[S11a] The flat transition structure was also calculated at the same level and were confirmed by one imaginary frequency which corresponds to bowl inversion. The difference between the subtotal energies + ZPEs of bowl and flat structures of $\mathbf{1}_{\mathit{exo}}$ or $\mathbf{1}_{\mathit{endo}}$ are reported as bowl inversion energy of $\mathbf{1}_{\mathit{exo}}$ or $\mathbf{1}_{\mathit{endo}}$.

The interaction energy simulation of the stacking dimer of **1** were performed at ωb97xd/6-311+g(d,p) level of theory using Gaussian09 package.[S11b] Prior to the simulation, the suitable models were built by making the stacking dimers with each monomer unit optimised under vacuum at the B3LYP/6-31G(d,p) level of theory. Basis set superposition error (BSSE) was corrected by the counterpoise method.

Cartesian coordinates of the optimized structures and the dimer models

a) Optimized cartesian coordinates of $\mathbf{1}_{\mathit{endo}}$ (B3LYP/6-311+G(d,p)).

C	0.77173	0.250769	-1.4088
C	0.858517	-0.9442	-0.71767
C	0.303772	-2.12583	-1.21235
C	0.138605	-3.0796	0
C	0.303772	-2.12583	1.212345
C	-0.24592	-2.08233	2.491768
C	-0.33484	-0.84641	3.20636
H	-0.73839	-2.95082	2.914856
H	-0.88586	-0.84616	4.141231
C	0.68907	1.489785	0.69311
C	0.68907	1.489785	-0.69311
C	-0.0126	2.442865	-1.43644
C	-0.23632	1.843354	-2.84989
C	0.1183	0.347599	-2.64289
C	-0.33484	-0.84641	-3.20636
C	-0.24592	-2.08233	-2.49177
H	-1.26823	1.971217	-3.18527
H	0.408441	2.314314	-3.60132
H	-0.88586	-0.84616	-4.14123
H	-0.73839	-2.95082	-2.91486
C	0.858517	-0.9442	0.717672
C	0.77173	0.250769	1.408803
C	0.1183	0.347599	2.642886
C	-0.23632	1.843354	2.849889
C	-0.0126	2.442865	1.436441
C	-0.60674	3.480645	0.714384
C	-0.60674	3.480645	-0.71438
H	-1.26823	1.971217	3.18527
H	0.408441	2.314314	3.601319
H	-1.19651	4.241006	1.216364
H	-1.19651	4.241006	-1.21636
H	0.880114	-3.88561	0
F	-1.11227	-3.70787	0

Total energy: −906.876770 Hartree.

b) Optimized cartesian coordinates of $\mathbf{1}_{\mathit{exo}}$ (B3LYP/6-311+G(d,p)).

C	-0.6755	-0.20687	-1.40719
C	-0.64298	0.991538	-0.71841
C	0.026805	2.112087	-1.21284
C	0.328189	3.030307	0
C	0.026805	2.112087	1.212839
C	0.565781	2.008671	2.494886
C	0.524329	0.772558	3.213407
H	1.173241	-2.12531	-3.1933
H	-0.53179	-2.29676	-3.59935
H	1.062624	0.718755	-4.1541
H	1.132121	2.826504	-2.92845
C	-0.64298	0.991538	0.718414
C	-0.6755	-0.20687	1.407194
C	-0.04001	-0.37004	2.644294

H	1.362407	3.382263	0
H	1.132121	2.826504	2.928446
H	1.062624	0.718755	4.154102
C	-0.71555	-1.44849	0.692736
C	-0.71555	-1.44849	-0.69274
C	-0.11523	-2.46748	-1.43671
C	0.161597	-1.89391	-2.85164
C	-0.04001	-0.37004	-2.64429
C	0.524329	0.772558	-3.21341
C	0.565781	2.008671	-2.49489
C	0.161597	-1.89391	2.851636
C	-0.11523	-2.46748	1.436709
C	0.371299	-3.55993	0.714524
C	0.371299	-3.55993	-0.71452
H	1.173241	-2.12531	3.193297
H	-0.53179	-2.29676	3.599351
H	0.879177	-4.37734	1.216373
H	0.879177	-4.37734	-1.21637
F	-0.47653	4.187408	0

Total energy: −906.875696 Hartree.

c) Optimized cartesian coordinates of flat transition structure of **1** (B3LYP/6-311+G(d,p)).

C	-3.74438	-0.72639	0.107237
C	-2.55178	-1.48866	0.055356
C	-1.4411	-0.68205	0.007272
C	-1.4411	0.682051	0.007272
C	-2.55178	1.488662	0.055357
C	-3.74438	0.726391	0.107237
C	-0.23092	-1.38037	-0.04257
C	-0.23092	1.380371	-0.04257
C	0.949006	0.700403	-0.09013
C	0.949006	-0.7004	-0.09013
C	2.197722	1.264344	-0.14774
C	2.140814	2.677186	-0.15019
C	0.882979	3.402508	-0.09094
C	-0.37124	2.748027	-0.03664
C	-1.9513	2.968203	0.031431
H	-2.2363	3.530133	0.925075
H	-4.71993	-1.19994	0.1502
H	-4.71993	1.199935	0.1502
H	3.040459	3.282174	-0.18713
H	0.959677	4.484917	-0.09113
C	-1.9513	-2.9682	0.031432
C	-0.37124	-2.74803	-0.03664
H	-2.23631	-3.53013	0.925076
C	0.882979	-3.40251	-0.09094
C	2.140814	-2.67719	-0.15019
C	2.197722	-1.26434	-0.14774
H	0.959677	-4.48492	-0.09113
H	3.040459	-3.28217	-0.18713
C	3.17498	0	-0.23882
H	-2.31246	3.533281	-0.8322
H	-2.31246	-3.53328	-0.8322
H	3.723028	0	-1.18512
F	4.13407	0	0.774586

Total energy: −906.843724 Hartree.

d) Cartesian coordinates of $\mathbf{1}_{endo}/\mathbf{1}_{endo}$ dimer (60° rotation).

C	-0.76361	0.25085	1.41007
C	-0.85351	-0.94568	0.71829
C	-0.30036	-2.13033	1.21258
C	-0.14076	-3.08922	0
C	-0.30036	-2.13033	-1.21258
C	0.24814	-2.08555	-2.49442
C	0.33729	-0.84892	-3.21119
H	-0.90637	-3.87785	0
H	0.73864	-2.95671	-2.91941
H	0.88571	-0.85066	-4.14978
C	-0.68311	1.49066	-0.69405
C	-0.68311	1.49066	0.69405
C	0.01178	2.44931	1.43959
C	0.23737	1.84816	2.85454
C	-0.11268	0.34866	2.6473
C	0.33729	-0.84892	3.21119
C	0.24814	-2.08555	2.49442
H	1.27128	1.97945	3.18953
H	-0.40381	2.31944	3.61194
H	0.88571	-0.85066	4.14978
H	0.73864	-2.95671	2.91941
C	-0.85351	-0.94568	-0.71829
C	-0.76361	0.25085	-1.41007
C	-0.11268	0.34866	-2.6473
C	0.23737	1.84816	-2.85454
C	0.01178	2.44931	-1.43959
C	0.59397	3.49515	-0.71515
C	0.59397	3.49515	0.71515
H	1.27128	1.97945	-3.18953
H	-0.40381	2.31944	-3.61194
H	1.17473	4.26508	-1.21709
H	1.17473	4.26508	1.21709
F	1.09273	-3.72975	0

C	3.13132	0.05213	-1.4127
C	3.22122	1.24866	-0.72092
C	3.94518	2.33736	-1.21521
C	4.24627	3.26163	-0.00263
C	3.94518	2.33736	1.20995
C	4.48083	2.21112	2.49178
C	4.38419	0.97505	3.20855
H	3.60709	4.15581	-0.00263
H	5.09599	2.9992	2.91678
H	4.88508	-1.96113	-3.19216
H	3.17799	-2.047	-3.61457
H	4.92672	0.89483	-4.15242
H	5.09599	2.9992	-2.92205
C	3.22122	1.24866	0.71565
C	3.13132	0.05213	1.40744
C	3.76033	-0.14184	2.64466
C	3.88239	-1.67682	2.8519
C	3.56951	-2.23751	1.43696

H	4.92672	0.89483	4.14715	**C**	3.98888	-3.3586	0.71252
C	3.02566	-1.18579	0.69142	**C**	3.98888	-3.3586	-0.71778
C	3.02566	-1.18579	-0.69668	**H**	4.88508	-1.96113	3.18689
C	3.56951	-2.23751	-1.44223	**H**	3.17799	-2.047	3.60931
C	3.88239	-1.67682	-2.85717	**H**	4.44808	-4.20667	1.21446
C	3.76033	-0.14184	-2.64993	**H**	4.44808	-4.20667	-1.21972
C	4.38419	0.97505	-3.21382	**F**	5.56162	3.71066	-0.00263
C	4.48083	2.21112	-2.49705				

e) Cartesian coordinates of **1***endo***/1***endo* dimer (180° rotation).

C	-0.76361	0.25085	1.41007	**H**	1.27128	1.97945	3.18953
C	-0.85351	-0.94568	0.71829	**H**	-0.40381	2.31944	3.61194
C	-0.30036	-2.13033	1.21258	**H**	0.88571	-0.85066	4.14978
C	-0.14076	-3.08922	0	**H**	0.73864	-2.95671	2.91941
C	-0.30036	-2.13033	-1.21258	**C**	-0.85351	-0.94568	-0.71829
C	0.24814	-2.08555	-2.49442	**C**	-0.76361	0.25085	-1.41007
C	0.33729	-0.84892	-3.21119	**C**	-0.11268	0.34866	-2.6473
H	-0.90637	-3.87785	0	**C**	0.23737	1.84816	-2.85454
H	0.73864	-2.95671	-2.91941	**C**	0.01178	2.44931	-1.43959
H	0.88571	-0.85066	-4.14978	**C**	0.59397	3.49515	-0.71515
C	-0.68311	1.49066	-0.69405	**C**	0.59397	3.49515	0.71515
C	-0.68311	1.49066	0.69405	**H**	1.27128	1.97945	-3.18953
C	0.01178	2.44931	1.43959	**H**	-0.40381	2.31944	-3.61194
C	0.23737	1.84816	2.85454	**H**	1.17473	4.26508	-1.21709
C	-0.11268	0.34866	2.6473	**H**	1.17473	4.26508	1.21709
C	0.33729	-0.84892	3.21119	**F**	1.09273	-3.72975	0
C	0.24814	-2.08555	2.49442				
C	3.03983	-1.1656	0.7024	**H**	4.88898	-1.90919	3.21697
C	3.03977	-1.16645	-0.68263	**H**	3.17848	-2.04046	3.6131
C	3.60354	-2.20963	-1.42265	**H**	4.5479	-4.14706	1.22802
C	3.8772	-1.65055	-2.84667	**H**	4.55975	-4.13796	-1.21547
C	3.7609	-0.11529	-2.63523	**C**	3.13298	0.07416	-1.40092
C	4.38937	0.99372	-3.20189	**C**	3.22281	1.26985	-0.70766
C	4.47857	2.23118	-2.48654	**C**	3.94854	2.36316	-1.19958
H	3.14319	-2.01848	-3.57741	**C**	4.25504	3.28302	0.01447
H	4.9386	0.9044	-4.13488	**C**	3.91582	2.37178	1.22645
H	5.08642	3.02038	-2.92176	**C**	4.4103	2.25026	2.52962
C	3.21031	1.27188	0.72626	**C**	4.31749	1.01506	3.24477
C	3.12025	0.07312	1.42031	**H**	5.30288	3.5997	0.02744
C	3.729	-0.11466	2.66605	**H**	3.6472	4.19802	0.00116
C	3.88461	-1.64728	2.86901	**H**	4.99324	3.04916	2.98124
C	3.605	-2.2092	1.44772	**H**	4.8353	0.94702	4.19833
C	4.06185	-3.31513	0.72464	**F**	5.13115	-2.0187	-3.3198
C	4.06567	-3.31459	-0.70748				

f) Cartesian coordinates of **1***exo***/1***exo* dimer (60° rotation).

C	0.63368	1.01029	0.70425	**H**	-1.27169	1.57888	3.22181
C	0.63361	1.01313	-0.6805	**H**	0.4195	1.86503	3.61764
C	-0.02133	1.99921	-1.42276	**H**	-1.11689	3.85484	1.23569
C	-0.28435	1.40451	-2.83645	**H**	-1.12799	3.8483	-1.20329
C	0.0331	-0.10593	-2.63857	**C**	0.66578	-0.23109	-1.39909
C	-0.46255	-1.28227	-3.20737	**C**	0.69674	-1.42851	-0.70425
C	-0.42323	-2.52356	-2.49484	**C**	0.09809	-2.59466	-1.19923
H	-1.32731	1.55275	-3.13981	**C**	-0.11979	-3.53973	0.01501
H	-0.99587	-1.26153	-4.15443	**C**	0.11344	-2.59664	1.22827
H	-0.92992	-3.37587	-2.94036	**C**	-0.39277	-2.52451	2.53096
C	0.70183	-1.4302	0.72911	**C**	-0.42479	-1.28588	3.24632

C	0.67078	-0.22958	1.42252		**H**	-1.12833	-3.96562	0.01962
C	0.04895	-0.10248	2.66876		**H**	0.58112	-4.38555	0.00766
C	-0.24776	1.40944	2.87337		**H**	-0.89061	-3.37833	2.98388
C	-0.02065	1.99751	1.45294		**H**	-0.94509	-1.27123	4.20082
C	-0.56769	3.06348	0.73192		**F**	0.51359	1.993	-3.81968
C	-0.57482	3.05942	-0.69986					
C	4.5581	0.02634	1.40786		**H**	2.71706	-1.89333	3.20153
C	4.52706	1.22659	0.71794		**H**	4.42025	-2.07099	3.60933
C	3.86847	2.3541	1.21515		**H**	2.85676	0.96687	4.17539
C	3.5662	3.27703	-0.00065		**H**	2.79098	3.07496	2.95049
C	3.86847	2.3541	-1.21646		**C**	4.52706	1.22659	-0.71925
C	3.34505	2.25157	-2.50817		**C**	4.5581	0.02634	-1.40916
C	3.38427	1.01415	-3.22741		**C**	3.9335	-0.13634	-2.65283
H	2.51871	3.60036	-0.00065		**C**	3.73067	-1.66322	-2.85901
H	2.79098	3.07496	-2.9518		**C**	4.00316	-2.23871	-1.44114
H	2.85676	0.96687	-4.1767		**C**	3.52722	-3.33694	-0.71601
C	4.59525	-1.21536	-0.69406		**C**	3.52722	-3.33694	0.71471
C	4.59525	-1.21536	0.69276		**H**	2.71706	-1.89333	-3.20284
C	4.00316	-2.23871	1.43983		**H**	4.42025	-2.07099	-3.61064
C	3.73067	-1.66322	2.85771		**H**	3.02865	-4.16269	-1.2176
C	3.9335	-0.13634	2.65152		**H**	3.02865	-4.16269	1.21629
C	3.38427	1.01415	3.22611		**F**	4.34948	4.43301	-0.00065
C	3.34505	2.25157	2.50686					

g) Cartesian coordinates of $\mathbf{1}_{exo}/\mathbf{1}_{exo}$ dimer (180° rotation).

C	0.56539	-0.21515	-1.40849		**H**	-1.37239	1.60681	-3.20217
C	0.59643	-1.4154	-0.71858		**H**	0.31934	1.87226	-3.60997
C	-0.00302	-2.57544	-1.21579		**H**	-1.08506	-1.24234	-4.17603
C	-0.25718	-3.51276	0.00002		**H**	-1.04181	-3.35102	-2.95113
C	-0.00302	-2.57544	1.21583		**C**	0.59643	-1.4154	0.71861
C	-0.53104	-2.50009	2.50753		**C**	0.56539	-0.21515	1.40853
C	-0.55581	-1.2623	3.22678		**C**	-0.06678	-0.08496	2.65219
H	-1.28656	-3.88979	0.00002		**C**	-0.34825	1.42939	2.85838
H	-1.04181	-3.35102	2.95116		**C**	-0.10586	2.0182	1.44051
H	-1.08506	-1.24234	4.17606		**C**	-0.63792	3.09037	0.71538
C	0.53832	1.02681	0.69343		**C**	-0.63792	3.09037	-0.71534
C	0.53832	1.02681	-0.69339		**H**	-1.37239	1.60681	3.2022
C	-0.10586	2.0182	-1.44047		**H**	0.31934	1.87226	3.61
C	-0.34825	1.42939	-2.85834		**H**	-1.1785	3.88924	1.21696
C	-0.06678	-0.08496	-2.65216		**H**	-1.1785	3.88924	-1.21693
C	-0.55581	-1.2623	-3.22674		**F**	0.58479	-4.62671	0.00002
C	-0.53104	-2.50009	-2.5075					
C	4.45828	0.0203	1.40787		**H**	2.61725	-1.89937	3.20155
C	4.42724	1.22055	0.71795		**H**	4.32043	-2.07703	3.60934
C	3.76865	2.34806	1.21517		**H**	2.75694	0.96083	4.17541
C	3.46639	3.27099	-0.00064		**H**	2.69116	3.06892	2.95051
C	3.76865	2.34806	-1.21645		**C**	4.42724	1.22055	-0.71923
C	3.24523	2.24553	-2.50815		**C**	4.45828	0.0203	-1.40915
C	3.28446	1.00811	-3.2274		**C**	3.83368	-0.14238	-2.65281
H	2.4189	3.59432	-0.00064		**C**	3.63085	-1.66926	-2.859
H	2.69116	3.06892	-2.95179		**C**	3.90334	-2.24475	-1.44113
H	2.75694	0.96083	-4.17668		**C**	3.4274	-3.34298	-0.716
C	4.49543	-1.2214	-0.69405		**C**	3.4274	-3.34298	0.71472
C	4.49543	-1.2214	0.69277		**H**	2.61725	-1.89937	-3.20283
C	3.90334	-2.24475	1.43985		**H**	4.32043	-2.07703	-3.61062
C	3.63085	-1.66926	2.85772		**H**	2.92883	-4.16872	-1.21758
C	3.83368	-0.14238	2.65154		**H**	2.92883	-4.16872	1.2163
C	3.28446	1.00811	3.22612		**F**	4.24966	4.42697	-0.00064
C	3.24523	2.24553	2.50687					

h) Cartesian coordinates of $\mathbf{1}_{endo}/\mathbf{1}_{exo}$ dimer (60° rotation).

C	0.66521	-0.20911	1.40851	**H**	-1.17582	-2.12878	3.20219
C	0.63417	0.99114	0.71859	**H**	0.52736	-2.30644	3.60998
C	-0.02442	2.11865	1.21581	**H**	-1.03612	0.73142	4.17605
C	-0.32668	3.04158	0	**H**	-1.10191	2.83951	2.95115
C	-0.02442	2.11865	-1.21581	**C**	0.63417	0.99114	-0.71859
C	-0.54784	2.01612	-2.50751	**C**	0.66521	-0.20911	-1.40851
C	-0.50861	0.7787	-3.22676	**C**	0.04061	-0.37179	-2.65217
H	-1.37417	3.36491	0	**C**	-0.16222	-1.89867	-2.85836
H	-1.10191	2.83951	-2.95115	**C**	0.11027	-2.47416	-1.44049
H	-1.03612	0.73142	-4.17605	**C**	-0.36567	-3.57239	-0.71536
C	0.70236	-1.45081	-0.69341	**C**	-0.36567	-3.57239	0.71536
C	0.70236	-1.45081	0.69341	**H**	-1.17582	-2.12878	-3.20219
C	0.11027	-2.47416	1.44049	**H**	0.52736	-2.30644	-3.60998
C	-0.16222	-1.89867	2.85836	**H**	-0.86424	-4.39813	-1.21694
C	0.04061	-0.37179	2.65217	**H**	-0.86424	-4.39813	1.21694
C	-0.50861	0.7787	3.22676	**F**	0.45659	4.19756	0
C	-0.54784	2.01612	2.50751				
C	-3.23519	0.87049	0.68817	**H**	-5.14281	1.4714	3.1972
C	-3.23105	0.87169	-0.69686	**H**	-3.44834	1.7316	3.59847
C	-3.86992	1.86942	-1.43853	**H**	-4.96607	3.72917	1.20935
C	-4.09624	1.29161	-2.86338	**H**	-4.96989	3.71983	-1.23416
C	-3.86476	-0.23051	-2.65164	**C**	-3.22799	-0.37223	-1.41546
C	-4.40582	-1.38374	-3.22022	**C**	-3.22918	-1.57146	-0.72251
C	-4.40329	-2.62459	-2.50518	**C**	-3.86864	-2.71642	-1.21663
H	-3.38999	1.7142	-3.5919	**C**	-4.1083	-3.65714	-0.00353
H	-4.95745	-1.33599	-4.15485	**C**	-3.84262	-2.72316	1.20949
H	-4.94838	-3.4574	-2.94224	**C**	-4.34876	-2.63973	2.51117
C	-3.22085	-1.57291	0.71144	**C**	-4.35181	-1.40124	3.22664
C	-3.22381	-0.37096	1.4058	**H**	-5.12922	-4.0522	0.00629
C	-3.84875	-0.23008	2.64971	**H**	-3.43294	-4.52353	-0.01505
C	-4.12047	1.28632	2.85225	**H**	-4.87094	-3.48056	2.96102
C	-3.87993	1.86814	1.43182	**H**	-4.87613	-1.37282	4.17864
C	-4.41697	2.93653	0.70741	**F**	-5.37303	1.56395	-3.34026
C	-4.41645	2.93607	-0.72471				

i) Cartesian coordinates of $\mathbf{1}_{endo}/\mathbf{1}_{exo}$ dimer (180° rotation).

C	0.66521	-0.20911	1.40851	**H**	-1.17582	-2.12878	3.20219
C	0.63417	0.99114	0.71859	**H**	0.52736	-2.30644	3.60998
C	-0.02442	2.11865	1.21581	**H**	-1.03612	0.73142	4.17605
C	-0.32668	3.04158	0	**H**	-1.10191	2.83951	2.95115
C	-0.02442	2.11865	-1.21581	**C**	0.63417	0.99114	-0.71859
C	-0.54784	2.01612	-2.50751	**C**	0.66521	-0.20911	-1.40851
C	-0.50861	0.7787	-3.22676	**C**	0.04061	-0.37179	-2.65217
H	-1.37417	3.36491	0	**C**	-0.16222	-1.89867	-2.85836
H	-1.10191	2.83951	-2.95115	**C**	0.11027	-2.47416	-1.44049
H	-1.03612	0.73142	-4.17605	**C**	-0.36567	-3.57239	-0.71536
C	0.70236	-1.45081	-0.69341	**C**	-0.36567	-3.57239	0.71536
C	0.70236	-1.45081	0.69341	**H**	-1.17582	-2.12878	-3.20219
C	0.11027	-2.47416	1.44049	**H**	0.52736	-2.30644	-3.60998
C	-0.16222	-1.89867	2.85836	**H**	-0.86424	-4.39813	-1.21694
C	0.04061	-0.37179	2.65217	**H**	-0.86424	-4.39813	1.21694
C	-0.50861	0.7787	3.22676	**F**	0.45659	4.19756	0
C	-0.54784	2.01612	2.50751				
C	-3.22797	-0.35013	-1.42723	**H**	-5.12369	1.52513	-3.21188
C	-3.22916	-1.55021	-0.73576	**H**	-3.42673	1.74002	-3.62917
C	-3.86719	-2.69043	-1.23225	**H**	-4.94627	-1.32554	-4.17235
C	-4.10112	-3.63514	-0.02061	**H**	-4.95953	-3.43701	-2.94255

C	-3.87444	-2.69106	1.19289	**C**	-3.23346	-1.55058	0.70081
C	-4.42195	-2.60603	2.47312	**C**	-3.23641	-0.35085	1.39289
C	-4.42124	-1.36638	3.19022	**C**	-3.88198	-0.20534	2.62823
H	-3.39613	-4.47841	-0.01872	**C**	-4.12044	1.31595	2.83515
H	-4.97699	-3.43851	2.89625	**C**	-3.84664	1.89907	1.42117
H	-4.97108	-1.32767	4.12718	**C**	-4.34746	2.9854	0.69551
C	-3.22256	0.8917	0.67723	**C**	-4.34319	2.98577	-0.73479
C	-3.21841	0.89205	-0.71086	**H**	-5.14276	1.5235	3.16714
C	-3.83803	1.89981	-1.458	**H**	-3.44833	1.73816	3.59467
C	-4.10337	1.31741	-2.87389	**H**	-4.87101	3.79616	1.19609
C	-3.86615	-0.20398	-2.66633	**H**	-4.86373	3.79679	-1.23808
C	-4.40204	-1.36473	-3.23213	**F**	-5.37873	-4.1824	-0.02457
C	-4.40703	-2.60475	-2.51569				

j) Cartesian coordinates of $\mathbf{1}_{exo}$/$\mathbf{1}_{endo}$ dimer (60° rotation).

C	-0.76361	0.25085	1.41007	**H**	1.27128	1.97945	3.18953
C	-0.85351	-0.94568	0.71829	**H**	-0.40381	2.31944	3.61194
C	-0.30036	-2.13033	1.21258	**H**	0.88571	-0.85066	4.14978
C	-0.14076	-3.08922	0	**H**	0.73864	-2.95671	2.91941
C	-0.30036	-2.13033	-1.21258	**C**	-0.85351	-0.94568	-0.71829
C	0.24814	-2.08555	-2.49442	**C**	-0.76361	0.25085	-1.41007
C	0.33729	-0.84892	-3.21119	**C**	-0.11268	0.34866	-2.6473
H	-0.90637	-3.87785	0	**C**	0.23737	1.84816	-2.85454
H	0.73864	-2.95671	-2.91941	**C**	0.01178	2.44931	-1.43959
H	0.88571	-0.85066	-4.14978	**C**	0.59397	3.49515	-0.71515
C	-0.68311	1.49066	-0.69405	**C**	0.59397	3.49515	0.71515
C	-0.68311	1.49066	0.69405	**H**	1.27128	1.97945	-3.18953
C	0.01178	2.44931	1.43959	**H**	-0.40381	2.31944	-3.61194
C	0.23737	1.84816	2.85454	**H**	1.17473	4.26508	-1.21709
C	-0.11268	0.34866	2.6473	**H**	1.17473	4.26508	1.21709
C	0.33729	-0.84892	3.21119	**F**	1.09273	-3.72975	0
C	0.24814	-2.08555	2.49442				
C	3.03576	-1.0746	0.69917	**H**	4.86031	-1.83879	3.22481
C	3.04159	-1.0776	-0.68557	**H**	3.14676	-1.94668	3.61318
C	3.59318	-2.12679	-1.4253	**H**	4.4773	-4.08638	1.23728
C	3.92305	-1.56299	-2.83763	**H**	4.49968	-4.08133	-1.20162
C	3.76424	-0.02763	-2.64063	**C**	3.14269	0.16309	-1.40388
C	4.38253	1.09043	-3.20687	**C**	3.23393	1.35727	-0.70878
C	4.46996	2.32913	-2.4941	**C**	3.95327	2.45445	-1.20076
H	4.94614	-1.81939	-3.13649	**C**	4.26336	3.37174	0.01474
H	4.9149	1.01398	-4.15161	**C**	3.92761	2.45833	1.22666
H	5.06485	3.1238	-2.93712	**C**	4.41782	2.33387	2.53151
C	3.22279	1.35966	0.72455	**C**	4.31717	1.09876	3.24659
C	3.12523	0.16245	1.41768	**H**	5.31084	3.68996	0.02389
C	3.72494	-0.02875	2.66658	**H**	3.65467	4.28615	0.00462
C	3.8612	-1.56337	2.87197	**H**	5.00013	3.13108	2.98689
C	3.58012	-2.12467	1.45038	**H**	4.82891	1.02996	4.20335
C	4.01597	-3.24204	0.73139	**F**	3.07231	-2.06504	-3.82453
C	4.02974	-3.23892	-0.70035				

k) Cartesian coordinates of $\mathbf{1}_{exo}$/$\mathbf{1}_{endo}$ dimer (180° rotation).

C	-0.76361	0.25085	1.41007	**H**	1.27128	1.97945	3.18953
C	-0.85351	-0.94568	0.71829	**H**	-0.40381	2.31944	3.61194
C	-0.30036	-2.13033	1.21258	**H**	0.88571	-0.85066	4.14978
C	-0.14076	-3.08922	0	**H**	0.73864	-2.95671	2.91941
C	-0.30036	-2.13033	-1.21258	**C**	-0.85351	-0.94568	-0.71829
C	0.24814	-2.08555	-2.49442	**C**	-0.76361	0.25085	-1.41007

C	0.33729	-0.84892	-3.21119	**C**	-0.11268	0.34866	-2.6473
H	-0.90637	-3.87785	0	**C**	0.23737	1.84816	-2.85454
H	0.73864	-2.95671	-2.91941	**C**	0.01178	2.44931	-1.43959
H	0.88571	-0.85066	-4.14978	**C**	0.59397	3.49515	-0.71515
C	-0.68311	1.49066	-0.69405	**C**	0.59397	3.49515	0.71515
C	-0.68311	1.49066	0.69405	**H**	1.27128	1.97945	-3.18953
C	0.01178	2.44931	1.43959	**H**	-0.40381	2.31944	-3.61194
C	0.23737	1.84816	2.85454	**H**	1.17473	4.26508	-1.21709
C	-0.11268	0.34866	2.6473	**H**	1.17473	4.26508	1.21709
C	0.33729	-0.84892	3.21119	**F**	1.09273	-3.72975	0
C	0.24814	-2.08555	2.49442				

C	3.141	0.14116	-1.4133	**H**	4.88569	-1.87345	-3.19913
C	3.23249	1.33818	-0.72313	**H**	3.17729	-1.9608	-3.61438
C	3.95199	2.4292	-1.21734	**H**	4.90179	0.99001	-4.17328
C	4.29735	3.33499	-0.00012	**H**	5.07368	3.09182	-2.94787
C	3.94137	2.42949	1.21426	**C**	3.22621	1.33835	0.71405
C	4.45298	2.29957	2.50823	**C**	3.1287	0.14151	1.40369
C	4.34519	1.06604	3.22716	**C**	3.73837	-0.05384	2.65005
H	5.36047	3.60244	0.00449	**C**	3.85922	-1.58929	2.85696
H	5.0479	3.09254	2.95437	**C**	3.56286	-2.14973	1.43785
H	4.86531	0.99103	4.17874	**C**	3.98318	-3.2717	0.71469
C	3.02902	-1.09657	0.6883	**C**	3.98943	-3.27187	-0.71602
C	3.03508	-1.09674	-0.69851	**H**	4.85772	-1.87267	3.20519
C	3.57544	-2.15008	-1.4431	**H**	3.14575	-1.95991	3.60552
C	3.88419	-1.58999	-2.85971	**H**	4.43516	-4.1226	1.21835
C	3.76154	-0.05449	-2.65424	**H**	4.44579	-4.1229	-1.21551
C	4.37338	1.06525	-3.2263	**F**	3.57635	4.53079	-0.00341
C	4.47489	2.29895	-2.50675				

References

1. R. J. Davey, S. L. M. Schroeder, J. H. ter Horst, *Angew. Chem., Int. Ed.* **2013**, *52*, 2166–2179.
2. A. Gavezzotti, G. Filippini, J. Kroon, B. P. van Eijck, P. Klewinghaus, *Chem. Eur. J.* **1997**, *3*, 893–899.
3. R. J. Davey, N. Blagden, S. Righini, H. Alison, M. J. Quayle, S. Fuller, *Cryst. Growth Des.* **2001**, *1*, 59–65.
4. A. Spitaleri, C. A. Hunter, J. F. McCabe, M. J. Packer, S. L. A Cockroft, *CrystEngComm* **2004**, *6*, 489–493.
5. S. Parveen, R. J. Davey, G. Dent, R. G. Pritchard, *Chem. Commun.* **2005**, 1531–1533.
6. R. J. Davey, G. Dent, R. K. Mughal, S. Parveen, *Cryst. Growth Des.* **2006**, *8*, 1788–1796.
7. J. Chen, B. L. Trout, *J. Phys. Chem. B.* **2008**, *112*, 7794–7802.
8. M. Habgood, *Phys. Chem. Chem. Phys.* **2012**, *14*, 9195–9203.
9. R. A. Sullivan, R. J. Davey, G. Sadiq, G. Dent, K. R. Back, J. H. ter Horst, D. Toroz, R. B. Hammond, *Cryst. Growth Des.* **2014**, *14*, 2689–2696.
10. E. Gaines, K. Maisuria, D. D. Tommaso, *CrystEngComm* **2016**, *18*, 2937–2948.
11. C. A. Hunter, J. F. McCabe, A. Spitaleri,*CrystEngComm* **2012**, *14*, 7115–7117.
12. J. Zeglinski, M. Kuhs, D. Khamar, A. C. Hegarty, R. K. Devi, Å. C. Rasmuson, *Chem. Eur. J.* **2018**, *24*, 4916–4926.
13. Y. Chai, L. Wang, Y. Bao, R. Teng, Y. Liu, C. Xie, *Cryst. Growth Des.* **2019**, *19*, 1660–1667.
14. R. G. Simões, P. L. T. Melo, C. E. Bernardes, M.T. Heilmann, F. Emmerling, M. E. Minas de Piedade, *Cryst. Growth Des.* **2021**, *21*, 544–551.
15. R. C. Burton, E. S. Ferrari, R. J. Davey, J. L. Finney, T. *J.* Bowron, *Phys. Chem. B* **2020**, *114*, 8807–8816.
16. A. Joseph, J. S. Rodrigues Alves, C. E. S. Bernardes, M. F. M. Piedade, M. E. Minas de Piedade, *CrystEngComm* **2019**, *21*, 2220–2233.

17. T. Nakamoto, M. Sakakibara, H. Nada, K. Harano, E. Nakamura, *J. Am. Chem. Soc.* **2021**, *143*, 1763–1767.

18. S. Fujii, M. Ziatdinov, S. Higashibayashi, H. Sakurai, M. Kiguchi, *J. Am. Chem. Soc.* **2016**, *138*, 12142–12149.

19. H. Sakurai, T. Daiko, T. Hirao, *Science* **2003**, *301*, 1878.

20. T. Amaya, H. Sakane, T. Muneishi, T. Hirao, *Chem. Commun.* **2008**, 765–767.

21. S. Higashibayashi, S. Onogi, H. K. Srivastava, G. N. Sastry, Y. Wu, H. Sakurai, *Angew. Chem., Int. Ed.* **2013**, *52*, 7314–7316.

22. B. M. Schmidt, B. Topolinski, S. Higashibayashi, T. Kojima, M. Kawano, D. Lentz, H. Sakurai, *Chem. Eur. J.*, **2013**, *9*, 3282–3286.

22. M. Li, J. Wu, K. Sambe, Y. Yakiyama, T. Akutagawa, T. Kajitani, T. Fukushima, K. Matsuda, H. Sakurai, *Mater. Chem. Front.* **2022**, *6*, 1752–1758.

23. M. Li, X. Chen, Y. Yakiyama, J. Wu, T. Akutagawa, H. Sakurai, *Chem. Commun.* **2022**, *58*, 8950–8953.

24. Y. Yakiyama, M. Li, H. Sakurai, *Pure Appl. Chem.* **2023**, *95*, 421–430.

25. H. Sakurai, T. Daiko, H. Sakane, T. Amaya, T. Hirao, *J. Am. Chem. Soc.* **2005**, *127*, 11580–11581.

26. S. Mebs, M. Weber, P. A. Luger, B. M. Schmidt, H. Sakurai, S. Higashibayashi, S. Onogi, D. Lentz, *Org. Biomol. Chem.* **2012**, *10*, 2218–2222.

27. P. Zanello, S. Fedi, F F. de Biani, G. Giorgi, T. Amaya, H. Sakane, T. Hirao, *Dalton Trans.* **2009**, 9192–9197.

28. L. Liu, Q. Guo, *Chem. Rev.* **2001**, *101*, 673-696.

29. A. Pan, T. Biswas, A. K. Rakshit, S. P. Moulik, *J. Phys. Chem. B* **2015**, *119*, 15876-15884.

30. J. Harada, N. Yoneyama, S. Sato, Y. Takahashi, T. Inabe, *Cryst. Growth Des.* **2019**, *19*, 291–299.

31. J. Harada, M. Ohtani, Y. Takahashi, T. Inabe, *J. Am. Chem. Soc.* **2015**, *137*, 4477–4486.

32. J. Wang, R. M. Wolf, J. W. Caldwell, P. A. Kollman, D. A. Case, *J. Comput. Chem.* **2004**, *25*, 1157–1174.

33. C. I. Bayly, P. Cieplak, W. D. Cornell, P. A. Kollman, *J. Phys. Chem.* **1993**, *97*, 10269–10280.

34. M. J. Abraham, T. Murtola, R. Schulz, S. P´all, J. C. Smith, B. Hess, E. Lindahl, *SoftwareX* **2015**, *1-2*, 19–25.

35. L. Martínez, R. Andrade, E. G. Birgin, J. M. Martínez, *J. Comput. Chem.* **2009**, 30, 2157−2164.

36. J. Wang, R. M. Wolf, J. W. Caldwell, P. A. Kollman, D. A. Case, *J. Comput. Chem.* **2004**, *25*, 1157–1174.

37. C. I. Bayly, P. Cieplak, W. D. Cornell, P. A. Kollman, *J. Phys. Chem*. **1993**, *97*, 10269–10280.

38. a)Gaussian 16, Revision C.01, M. J. Frisch, G. W. Trucks, H. B. Schlegel, G. E. Scuseria, M. A. Robb, J. R. Cheeseman, G. Scalmani, V. Barone, G. A. Petersson, H. Nakatsuji, X. Li, M. Caricato, A. V. Marenich, J. Bloino, B. G. Janesko, R. Gomperts, B. Mennucci, H. P. Hratchian, J. V. Ortiz, A. F. Izmaylov, J. L. Sonnenberg, D. Williams-Young, F. Ding, F. Lipparini, F. Egidi, J. Goings, B. Peng, A. Petrone, T. Henderson, D. Ranasinghe, V. G. Zakrzewski, J. Gao, N. Rega, G. Zheng, W. Liang, M. Hada, M. Ehara, K. Toyota, R. Fukuda, J. Hasegawa, M. Ishida, T. Nakajima, Y. Honda, O. Kitao, H. Nakai, T. Vreven, K. Throssell, J. A. Montgomery, Jr., J. E. Peralta, F. Ogliaro, M. J. Bearpark, J. J. Heyd, E. N. Brothers, K. N. Kudin, V. N. Staroverov, T. A. Keith, R. Kobayashi, J. Normand, K. Raghavachari, A. P. Rendell, J. C. Burant, S. S. Iyengar, J. Tomasi, M. Cossi, J. M. Millam, M. Klene, C. Adamo, R. Cammi, J. W. Ochterski, R. L. Martin, K. Morokuma, O. Farkas, J. B. Foresman, and D. J. Fox, Gaussian, Inc., Wallingford CT, 2016. b)Gaussian 09, Revision E.01, M. J. Frisch, G. W. Trucks, H. B. Schlegel, G. E. Scuseria, M. A. Robb, J. R. Cheeseman, G. Scalmani, V. Barone, B. Mennucci, G. A. Petersson, H. Nakatsuji, M. Caricato, X. Li, H. P.

Hratchian, A. F. Izmaylov, J. Bloino, G. Zheng, J. L. Sonnenberg, M. Hada, M. Ehara, K. Toyota, R. Fukuda, J. Hasegawa, M. Ishida, T. Nakajima, Y. Honda, O. Kitao, H. Nakai, T. Vreven, J. A. Montgomery, Jr., J. E. Peralta, F. Ogliaro, M. Bearpark, J. J. Heyd, E. Brothers, K. N. Kudin, V. N. Staroverov, R. Kobayashi, J. Normand, K. Raghavachari, A. Rendell, J. C. Burant, S. S. Iyengar, J. Tomasi, M. Cossi, N. Rega, J. M. Millam, M. Klene, J. E. Knox, J. B. Cross, V. Bakken, C. Adamo, J. Jaramillo, R. Gomperts, R. E. Stratmann, O. Yazyev, A. J. Austin, R. Cammi, C. Pomelli, J. W. Ochterski, R. L. Martin, K. Morokuma, V. G. Zakrzewski, G. A. Voth, P. Salvador, J. J. Dannenberg, S. Dapprich, A. D. Daniels, Ö. Farkas, J. B. Foresman, J. V. Ortiz, J. Cioslowski, and D. J. Fox, Gaussian, Inc., Wallingford CT, 2009.

39. U. Essmann, L. Perera, M. L. Berkowitz, T. Darden, H. Lee, L. G. Pedersen, *J. Chem. Phys.* **1995**, *103*, 8577–8593.
40. D. van der Spoel, P. J. van Maaren, *J. Chem. Theory Comput.* **2006**, *2*, 1–11.
41. W. F. van Gunsteren, H. J. C. Berendsen, *Mol. Simul.* **1988**, 1, 173−185.
42. N. Goga, A. J. Rzepiela, A. H. de Vries, S. J. Marrink, H. J. C. Berendsen, *J. Chem. Theory Comput.* **2012**, 8, 3637−3649.
43. H. J. C. Berendsen, J. P. M. Postma, W. F. van Gunsteren, A. DiNola, J. R. Haak, *J. Chem. Phys.* **1984**, *81*, 3684–3690.
44. M. Parrinello, A. Rahman, *J. Appl. Phys.* **1981**, *52*, 7182–7190.
45. B. Hess, H. Bekker, H. J. C. Berendsen, J. G. E. M. Fraaije, *J. Comput. Chem.* **1997**, *18*, 1463–1472.
46. N. Matubayasi, M. Nakahara, *J. Chem. Phys.* **2002**, 117, 3605−3616.
47. S. Sakuraba, N. Matubayasi, *J. Comput. Chem.* **2014**, 35, 1592−1608. Footnote 1 on page 1598 of this paper is incorrectly stated. The TIP3P model used for the calculations was the CHARMM-modified one with a Lennard-Jones term on the hydrogen atom.

Summary

In this doctoral dissertation, two fluorinated sumanene derivatives were synthesized successfully- **F2-Sum** and **F-Sum**, and the physical properties of them were characterized by NMR, UV, CV, single crystal x-ray crystallography. They can be used to produce the dielectric materials that the dielectric response can be tuned.

In Chapter 2, the author designed and synthesized 1,1-difluorosumanene, a curved π-conjugated molecule with two fluorines on one benzyl position on pristine sumanene. This results in a high dipole potential in the planar direction. Thermal experiments at varying temperatures, X-ray single crystal diffraction analysis, and infrared studies revealed a planar motion in the packing columns of 1,1-difluorosumanene, without any phase transition. Dielectric experiments on powder pellet and single-crystal of 1,1-difluorosumanene revealed that the real (ε_1) and imaginary (ε_2) parts of the dielectric constant increased above 360 K at 1 MHz due to Debye-type dielectric relaxation, indicating an in-plane motion caused by the applied electric field.

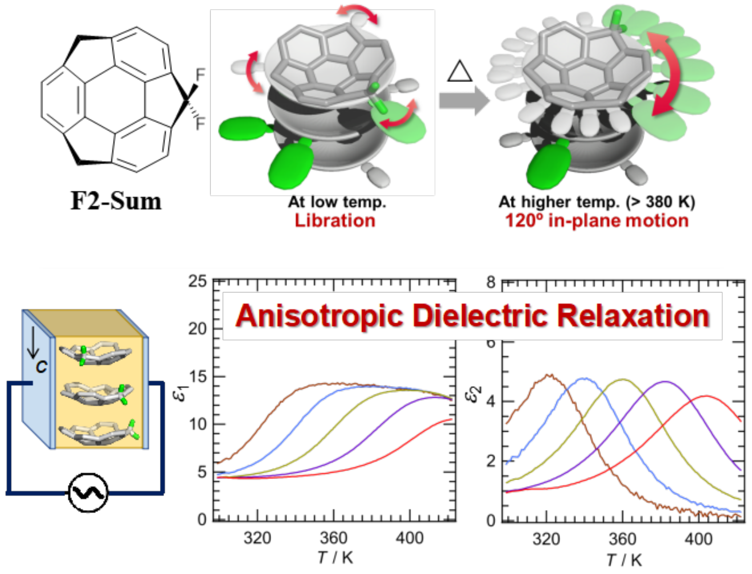

In Chapter 3, the author produced lots of co-crystals composed of 1,1-difluorosumanene and sumanene. Co-crystallization was succeeded in adjusting the structural and physical parameters, particularly the dielectric response, without requiring chemical alterations. X-ray analysis and theoretical studies show that 1,1-difluorosumanene reduces intermolecular interaction energy.

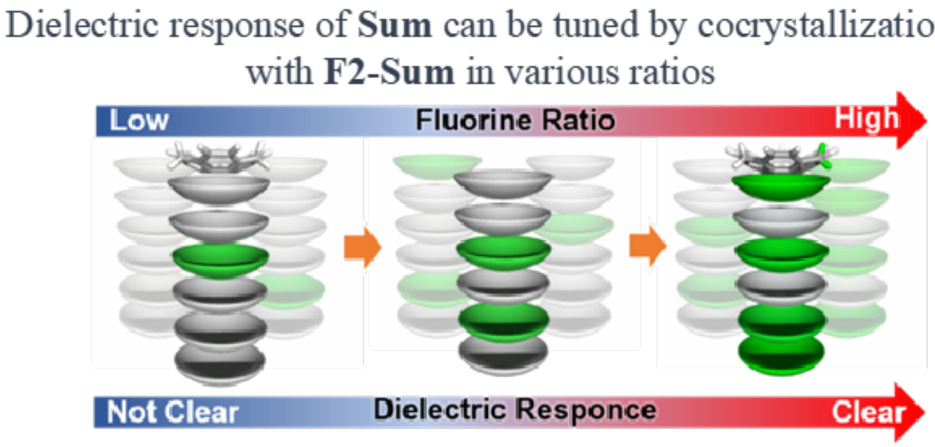

In Chapter 4, 1-fluorosumanene(**1**) was developed which has one fluorine atom on the benzyl position of sumanene. Interestingly, 1-fluorosumanene exhibits bowl inversion in a solvated state, resulting in the creation of two diastereomeric isomers: $\mathbf{1}_{endo}$ and $\mathbf{1}_{exo}$, each with a distinct dipole moment. The study found an energy link between $\mathbf{1}_{exo}$, $\mathbf{1}_{endo}$, and the solvent, allowing for manipulation of the *exo*:*endo* ratio in single crystals by selecting the specified solvent for crystallization. The molecular dynamics (MD) simulations show that $\mathbf{1}_{exo}$ promotes packing structure elongation. The ultimate *exo* to *endo* proportion is influenced by the stability varies between $\mathbf{1}_{endo}$ and $\mathbf{1}_{exo}$ due to solvation. The tunable *exo* to *endo* proportion of **1** allows for the creation of new materials with distinct dielectric responses.

These works pave the way for future research into sumanene in-plane motion, including the presentation of design strategies and synthesis of benzyl fluorinated sumanenes, as well as fully characterization methodologies for molecular movements using specific-heat measurements, variable temperature PXRD, variable temperature x-ray, and variable temperature IR. Because the orientations of the fluorosumanenes in the packing structures can be changed in single crystal state under the external electric field, the author believe that these works will benefit the development of molecular machines, molecular devices, and molecular switches and the related physical properties of them that depend on the packing structure can be altered by external electric field.

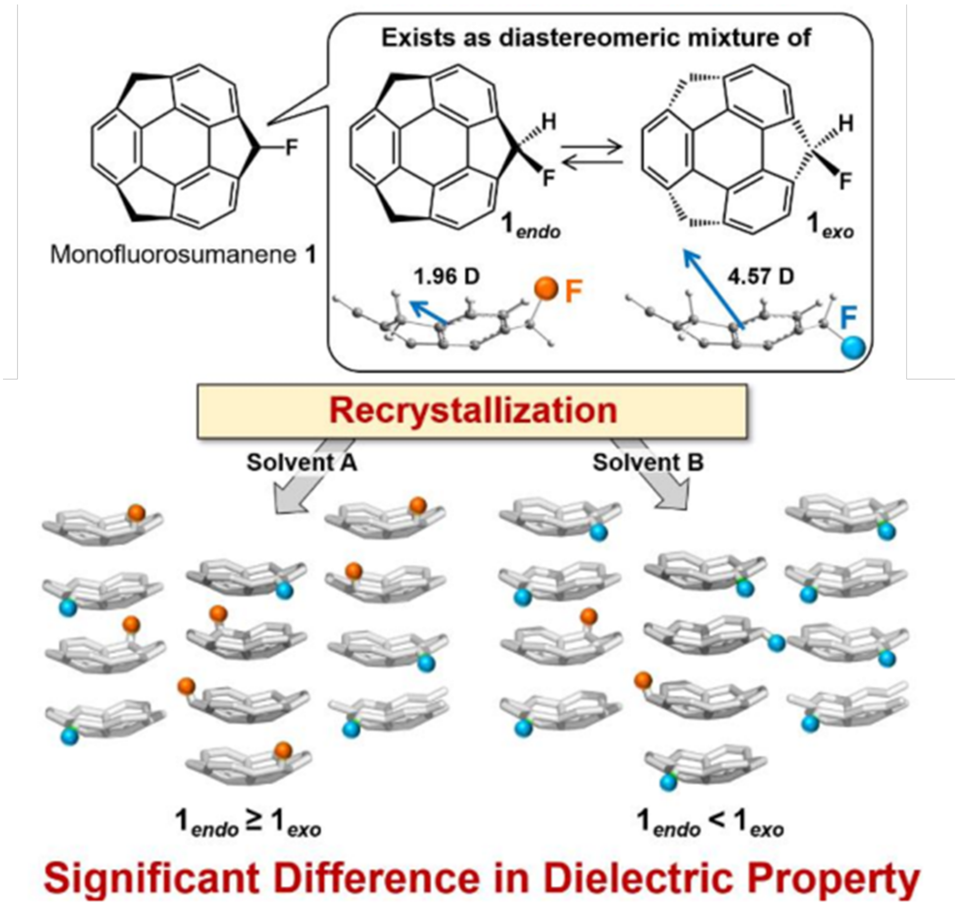

List of Publications

The content of this thesis has been published in the following papers.

1. Dielectric Response of 1,1-Difluorosumanene Caused by An In-plane Motion
Minghong Li, JianYun Wu, Kohei Sambe, Yumi Yakiyama, Tomoyuki Akutagawa, Takashi Kajitani, Takanori Fukushima, Kazunari Matsudah and Hidehiro Sakurai
Mater. Chem. Front., **2022**, *6*, 1752.

2. Tuning Dielectric Response by Co-crystallizing Sumanene and Its Fluorinated Derivative
Minghong Li, Xi Chen, JianYun Wu, Tomoyuki Akutagawa, Yumi Yakiyama and Hidehiro Sakurai, *Chem. Commun.*, **2022**, *58*, 8950.

3. Bowl-Direction Control of Monofluorosumanene in the Solid State
Yumi Yakiyama, **Minghong Li**, Dongyi Zhou, Tsuyoshi Abe, Chisato Sato, Kohei Sambe, Tomoyuki Akutagawa, Teppei Matsumura, Nobuyuki Matubayashi, Hidehiro Sakurai, *J. Am. Chem. Soc.*, **2024**, *146*, 5224.

Copyright

The author has obtained the permissions to reuse contents. The author wishes to express his thanks to Copyright Clearance Center, Creative Commons, The Royal Society of Chemistry and American Chemical Society

Credits

Reprinted with permission from **Minghong Li**, JianYun Wu, Kohei Sambe, Yumi Yakiyama, Tomoyuki Akutagawa, Takashi Kajitani, Takanori Fukushima, Kazunari Matsudah and Hidehiro Sakurai, *Mater. Chem. Front.*, **2022**, *6*, 1752. Copyright 2024 The Royal Society of Chemistry.

Reprinted with permission from **Minghong Li**, Xi Chen, JianYun Wu, Tomoyuki Akutagawa, Yumi Yakiyama and Hidehiro Sakurai, *Chem. Commun.*, **2022**, *58*, 8950. Copyright 2024 The Royal Society of Chemistry.

Reprinted with permission from Yumi Yakiyama, **Minghong Li**, Dongyi Zhou, Tsuyoshi Abe, Chisato Sato, Kohei Sambe, Tomoyuki Akutagawa, Teppei Matsumura, Nobuyuki Matubayashi, Hidehiro Sakurai, *J. Am. Chem. Soc.* **2024**, *146*, 5224. Copyright 2024 American Chemical Society.

Acknowledgement

First and foremost, I would like to thank Dr. Yumi Yakiyama for guiding me in all of the projects during my Ph.D. course. She is really nice and patient in teaching me scientific skills such as analysis and writing academic papers. Meanwhile, I would like to thank Prof. Hidehiro Sakurai for teaching me how to be receptive to science and how to connect all the knowledge in different fields in a unified way. I also want to thank Dr. Yuta Uetake, from whom I've learned a lot in the journal reports. With the skills I learned from them, I am convinced that I will be a qualified chemical researcher in the future.

In addition, I want to thank Prof. Tomoyuki Akutagawa (Tohoku University) and the students - and Mis. JianYun Wu, and Mr. Kohei Sambe in his lab who helped me to measure the dielectricity; I thank Prof. Takanori Fukushima and Dr. Takashi Kajitani (Tokyo Institute of Technology) for heat capacity measurement; I am also grateful to Prof. Kazunari Matsuda (Kyoto University) for the help in VT-IR measurement. I'd like to thank Dr. Xi Chen (Northeast Petroleum University) in particular for her assistance with DFT calculations.

Finally, I'd like to thank everyone at Sakurai Lab for their wonderful support and assistance, especially Mr. Junyi Han, Mr. Mikey Nishimoto, and Mr. Hironobu Nakazawa for their assistance with DFT calculations.

May 2024

Minghong Li